2018

Micro-nano biosystems: silicon nanowire sensor and micromechanical wireless power receiver

BOSTON UNIVERSITY

COLLEGE OF ENGINEERING

Dissertation

MICRO-NANO BIOSYSTEMS: SILICON NANOWIRE SENSOR AND MICROMECHANICAL WIRELESS POWER RECEIVER

by

FARRUKH MATEEN

B.S., National University of Sciences and Technology, 2004
M.S., Purdue University, 2008

Submitted in partial fulfillment of the

requirements for the degree of

Doctor of Philosophy

2018

Approved by

First Reader

Pritiraj Mohanty, PhD
Professor of Physics
Professor of Materials Science and Engineering

Second Reader

Thomas G. Bifano, PhD
Professor of Mechanical Engineering
Professor of Materials Science and Engineering
Professor of Biomedical Engineering

Third Reader

Shyamsunder Erramilli, PhD
Professor of Physics
Professor of Materials Science and Engineering
Professor of Biomedical Engineering

Fourth Reader

Alice White, PhD
Professor and Chair of Mechanical Engineering
Professor of Materials Science and Engineering
Professor of Biomedical Engineering

Faiz thi raah sarbasar manzil
Hum jahaan pahunche kaamyaab aaye

- Faiz Ahmed Faiz (1911 - 1984)

Acknowledgments

This thesis has certainly been a journey for me - both intellectually and personally. It would not have been complete without the guidance and support of my advisor Dr. Raj Mohanty. He welcomed me into his group and has over the years equipped me with the tools to help me through. But most of all what he has given me is confidence - for which I will forever be indebted to him. It is incredible how despite having a busy schedule he has always and still continues to be available with helpful guidance and advice. I still remember one evening from back in early 2014 when I trying to figure out how a Network Analyzer worked, he explained it to me in about ten minutes. I would also like to extend my gratitude and thanks to Prof. Shyamsunder Erramilli for his support and encouragement through out the course of my work here at Boston University. The ease, patience and graciousness with which he has answered all of my queries ranging from the truly perplexing to the most trivial, through all these years has helped me along immensely. Even when I sent him a question at 2 am in the morning he would answer it right away. I feel truly blessed to have him on my committee and to have known him.

I would also like to extend my heartfelt thanks to Dr. Alice White, who has always taken an interest in my work both as part of my thesis committee and in general. She has helped me, in times when I have needed it the most when I needed it the most. I cannot thanks her enough for her advise, comments and patience. I would also like to thank Dr. Thomas Bifano for having been my advisor in Mechanical Engineering and a committee member. Thank you sir, for keeping me focused and guiding me along this journey. Your questions and comments have helped me hone the rough edges of my work and given me inspiration to improve myself.

No Ph.D. student can do it alone, and so I would like to thank Mirtha Cabello, who quiet literally takes the well being of her grad students very personally. She

is the one stop shop for all graduate student related woes - and she always has a solution and a kind word (or two). I would also like to thank Anita Gupta for all her support in ordering things and helping me navigate the so many form. I would also like to thank Despina Bokios for helping me with so many administrative matters and for being so kind. Working in the MEMS area one cannot achieve anything without the OPF facility and even more importantly Paul Mak. His importance to my work can be gauged by the fact that in my long and involved fabrication process I would worry less about whether layers of patterned materials would come off at the next lift off and more about the ever looming question, "how will I manage when Paul goes on holiday." Without his continuous and express support with materials and keeping the clean room up and running - this work would never have been done. I cannot thank him enough. I have learned so much from him. Similarly I would like to thank Anlee Krupp for all her help and support in the use of the SEMs and with ebeam-lithography.

My journey would have been pretty monochromatic if it was not for my friends at BU: Mustafa Ordu, Joe Boales, Shawn Medford, Carsten Madler, Leanord Kogos, Buraq, Justin Mann, GD, Dr. Carl Boone and Yu Jin.

While I still talk to you, Mustafa nearly every day, as i'll probably continue to do so for a long time - I wish for more of all the times your company made the rather bland-food of the student dining halls taste better, the hard times a little easier, and made my life so much brighter. Joe, thanks for making me realize every day not to make definitive statements - their is always room for error. Your penchant for knowing everything from the tax-code to the penal-code to laws of physics and math has always challenged me to be better informed. Thanks for sharing your nearly twenty solutions to every single problem.

I would also like to thank my Boston Cares friends and fellow volunteers Alle-

gra, Emily, Simon, Patrice, Debra, Dan, Sarah, Nancy, Parsuna, Vanessa, Jo-Ellen, Phyllis, Emera and so many more - thank you for showing me the most noble side of humanity. I have never known such remarkable group of people. May you all grow in your volunteering spirit and continue to spread joy through your efforts.

I would also like to thank my life long best friends: Faisal, Fahd, Yasir, Abu Bakr, Haroon and Nabeel - you guys know me more than I know myself. Thank you for being the support structure that you have always been for me.

Most of all I would like to thank God for always having an eye out for me, and to all the many people and events that have helped me realize his existence. I would like to thank Mama and Baba who have loved me more than this son ever deserved or imagined or even has yet to realize. You truly gave me hope and love when it seemed that there was none for me and prayed for me every step of the way. I am sorry I don't call you up as often as I should. But I want you to know that I stand here bolstered up by your hopes and prayers.

This journey has truly been unique for me. Intellectually it has challenged me to learn and grapple with so many diverging facts and figures and streams of learning and to realize and be confident in the knowledge that I too can achieve. Personally it has shown me so many of those strong and promising and burgeoning supports that seemingly were joined at my hip, and who trumpeted there support for ever and ever; and who all withered away under the weight of one moment. All crumpled away and gone. All that remained - that has always remained has been my wife - *Mariah* - I owe so much to you. You make my life easier and richer and have held on when all else fell away. Your support has allowed me to reach this place. I try everyday to become the husband you truly deserve.

MICRO-NANO BIOSYSTEMS: SILICON NANOWIRE SENSOR AND MICROMECHANICAL WIRELESS POWER RECEIVER

FARRUKH MATEEN

Boston University, College of Engineering, 2018

Major Professors: Pritiraj Mohanty, PhD
Professor of Physics
Professor of Materials Science and Engineering

Thomas Bifano, PhD
Professor of Mechanical Engineering
Professor of Materials Science and Engineering
Professor of Biomedical Engineering

ABSTRACT

Silicon Nanowire based biosensors owe their sensitivity to the large surface area to volume ratio of the nano-wires. However, presently they have only been shown to detect specific bio-markers in low-salt buffer environments. The first part of this thesis presents a pertinent next step in the evolution of these sensors by presenting the specific detection of a target analyte (NT-ProBNP) in a physiologically relevant solution such as serum. By fabrication of the nanowires down to widths of 60 nm, choosing appropriate design parameters, optimization of the silicon surface functionalization recipe and using a reduced gate oxide thickness of 5 nm; these sensors are shown to detect the NT-ProBNP bio-marker down to 2 ng/ml in serum. The observed high background noise in the measured response of the sensor is discussed and removed experimentally by the addition of an extra microfabrication step to employ

a differential measurement scheme. It is also shown how the modulation of the local charge density via external static electric fields (applied by on chip patterned electrodes) pushes the sensitivity threshold by more than an order of magnitude. These demonstrations bring the silicon nanowire-based biosensor platform one step closer to being realized for point-of-care (POC) applications. In the second half of the thesis it is demonstrated how silicon micromechanical piezoelectric resonators could be tasked to provide wireless powering to such POC bio-systems. At present most sensing and actuation platforms, especially in the implantable format, are powered either via on-board battery packs which are large and need periodic replacement or are powered wirelessly through magnetic induction, which requires a proximately located external charging coil. Using energy harnessed from electric fields at distances over a meter; comprehensive distance, orientation and power dependence for these first-generation devices is presented. The distance response is non-monotonic and anomalous due to multi-path interferences, reflections and low directivity of the power receiver. This issue is studied and evaluated using COMSOL Multiphysics simulations. It is shown that the efficiency of these devices initially evaluated at 3% may be enhanced up to 15% by accessing higher frequency modes.

Contents

List of Figures

List of Abbreviations

AC	.....	Alternating Current
AlN	.....	Aluminum Nitride
ALD	.....	Atomic Layer Deposition
BAW	.....	Bulk Acoustic Wave
B-fields	.....	Magnetic Fields
BU	.....	Boston University
DC	.....	Direct Current
E-fields	.....	Electric Fields
FWHM	.....	Full-Width at Half Maximum
IDT	.....	Inter digitated electrodes
LAW	.....	Lamb Acoustic Wave
LIA	.....	Lock in Amplifier
POC	.....	Point of Care
Q	.....	Quality Factor
SAW	.....	Surface Acoustic Wave
VNA	.....	Vector Network Analyzer

Chapter 1

Introduction

1.1 Motivation

Health is a valued asset in modern society. This is reflected in the annual health expenditure, which is projected to be 5.7 trillion USD by the year 2026, about 19.7% of the US GDP then. The world biosensor market according to multiple sources is expected to be valued at above 25 Billion USD in the next five years. This includes point-of-care devices, home diagnostics, biodefense, environmental monitory, food and beverage industry etc. Especially in the medical sciences, such sensors could provide early detection of health threatening factors, which could then be treated and managed, at a significantly lower expense than if the disease was allowed to progress and eventually required invasive intervention. Early detection of health-threatening factors is both a financially and practically viable tool for the medical field in its entirety, especially given present financial pressures. Hence a substantial research effort is been directed towards the development of not only wireless, hand-held, point-of-care devices but those that could be wearable and eventually implantable. Implantable bio-sensors of the near future could possibly monitor and report on multiple health-threatening factors and could be customizable to the needs of individual patients.

Two important aspects of realizing such sensors (whether handheld, wearable or implantable) are for them to remain sensitive and selective in physiologically relevant environments and to also be wirelessly powered to aid in their monitoring function and placement. Development of novel micro and nano-devices for biomedical applications

can not only deliver detection tools for an arbitrary disease but in the near future administer treatments as well.

Take for instance the dilemma faced by a dermatologist having received a patient presenting with severe skin lesions. His practice is far from the nearest lab and the test to confirm his suspicions would take about two days to return. Wouldn't it be helpful if he had a hand-held device that could scoop up a few cells, from the patient's skin, make an analysis and provide an early indication either confirming or denying some of his fears. Such Point-of-Care (POC) devices could have also come in handy in making an in-field early diagnosis, during the deadly outbreak of the Ebola virus in western Africa in 2013-16 during which, according to the World Health Organization (WHO) more than 11,000 people lost their lives. The lab test for Ebola takes about 5 days to turn around and requires a lab having bio-safety level 4 and highly trained technicians. Hence there is significant room for the growth and a pressing need for specific and sensitive biosensors.

Similarly a wearable skin-patch type of a biosensor could constantly monitor specific physiological parameters for a patient and remotely convey them to a doctor or nurse. Many such systems often referred to as telemedicine sensors [Ajami and Teimouri, 2015, Roda et al., 2014, Cha et al., 2014] already exist and have been reported extensively in recent years. One interesting and rather unique work was reported by Mannor et. al [Mannoor et al., 2012] who developed a graphene-based sensor for peptide based biosensing. The slim form sensor can be placed on the front tooth as a tattoo and can monitor bacteria in saliva. It links with a base station for communication and powering purposes. Another example is the recently unveiled tele-sensor by Philips Healthcare which is a 36 x 8 mm, battery powered skin patch for remote surveillance of a patient's heart rate, motion, ECG and body temperature. Similar efforts from private enterprises and startups such as Vital-Connect (Campbell,

CA, USA), Eccrine Systems (OH, USA), Nix. Inc (MA, USA), ContinUse Biometrics (Israel) have resulted in multiplexed wearable biosensors able to monitor as many as thirty body parameters. In addition technology giants such as Google have developed the Lens technology which can detect the glucose levels from tear fluids in the eye and is reportedly working on patches that could record ECG from behind the ear. Even Apple has reportedly been developing a skin sensor for glucose monitoring which could possibly (although not confirmed) be integrated in their Apple watch platform.

Research has suggested that in the elderly population acceptance of wearable patches has been low hence researchers have developed smart-shirts and belts with electrodes in contact with the skin to increase patient compliance [Steele et al., 2009, Sardini and Serpelloni, 2010]. Pandian et. al in there article [Pandian et al., 2008] pointed to further applications for such smart shirts in the realms of manned space missions, fire-fighting, military - where they could monitor and report on critical body parameters. Similar clothing and patches could also alert first aid services should a person living alone suffer a cardiac arrest thus decreasing critical response time [Gyselinckx et al., 2007]. And while research continues to make such systems smarter, slimmer and in the case of skin patches - able to cling on to the skin via the use of micro-fabricated elastomeric substrates [Xu et al., 2014] the limiting factor is still the powering of such systems which is mostly done via battery packs. Such battery packs either require periodic replacement, and the scant few applications that employ wireless powering do so with specifically designed systems only able to cater to the specific sensor. It would be extremely beneficial if a single robust platform could be used to power multiple sensing platforms, wirelessly.

Implantable biosensor have been developed for monitoring critical parameters, such as body temperature, pH, blood glucose, cholesterol, lactate and drug levels [Bolomey et al., 2009, Nawito et al., 2015]. Most of these sensors employ magnetic

induction as the wireless powering mechanism, which requires an external charging coil to be worn, usually in the form of a band. Since the intensity of magnetic induction reduces with increasing distance between the primary and secondary coils, such sensors can only be implanted a few millimeters under the skin. Implantable deep brain biosensors have also been developed to predict and mitigate the onset of epileptic seizures [Da Cunha et al., 2015, Blaha et al., 2015, Lewitus et al., 2014, Tan et al., 2015]. Figure 1·1 shows in schematic form how one such deep brain stimulation device developed by Medtronics (MN, USA) is implanted in the brain. Notice, the electrodes are controlled and powered by battery packs placed higher inside the torso. In a similar stream other stimulators have been developed for treatment of Alzhimers, PTSD and even depression. However all of them need powering via battery packs which need frequent replacement. Thus implantable biosensors could benefit from a type of wireless actuation that would aid in there placement deep inside the body, thus realizing their peak functional potential.

With the above discussion it is not hard to see that sensors often serve critical life saving functions and while they have experienced a significant reduction in form factor, powering devices to run such implants haven't shrunk down by at the same rate. Where wireless powering has been employed it has largely been with magnetic induction, which confines the placement of the biosensor to only a couple of millimeters deep within the body. Despite extensive research efforts the development of wirelessly actuated point of care (POC) device platforms remains a grand challenge from both a technological and medical point of view [Ghafar-Zadeh, 2015].

This thesis attempts to introduce two robust platforms: one a silicon nanowire based biosensor and the second a piezoelectric micro-mechanical resonator as two possible solutions for sensitive bio-molecule recognition and wireless actuation at a distance. While the integration of these two platforms is not in the scope of this

Figure 1·1: Schematic showing the placement of deep brain electrodes with the controller and battery pack placed in the upper torso. Picture credit https://www.epilepsysociety.org.uk

thesis, however it does imply that both can be developed further and possibly be used in unison for the next generation of wirelessly powered highly sensitive bio-sensors capable of being adapted to handheld, wearable and implantable formats.

1.2 Thesis Organization

This thesis consists of five chapters and two appendicies.

Chapter 2, introduces wireless actuation and piezoelectric micro-mechanical resonators. In recent years these resonators have found uses mostly in timing applications in electronic circuits. This thesis explores their use for wireless actuation applications. The interdigitated transducer (IDT) electrodes overlaid above the resonator element simultaneously function as patch antennas capable of receiving external Electric Fields (E-fields) and actuating the element below. It is by the use of these E-Fields that we can actuate these devices at a distance of about a meter.

However E-fields unlike magnetic fields (which do not interact with objects in there paths) reflect off of surfaces and interfere resulting in non-intuitive responses of the device. COMSOL multiphysics simulations are used to investigate this non-intuitive behavior. The complete distance and polarization dependance of the piezoelectric device is also presented and discussed. It is pertinent to note that all measurements of this device are carried out at -10 dBm (0.1 mW) which compared to nearly a Watt of power that a personal cellphone uses in talk mode, is significantly less.

Chapter 3, carries on the discussion of Chapter 2 by expanding on methods of increasing efficiency of the device by means of accessing higher frequency modes. It starts with a brief discussion of the modes of the resonator and then diverges into how accessing certain higher frequency modes can increase the efficiency by nearly five times.

Chapter 4, introduces Silicon Nanowire based biosensors. It discusses the significance of this robust platform and then describes how we have used these sensors to measure the presence of the cardiac bio-marker NT-ProBNP in Serum using nanowires fabricated down to 60 nm in thickness. Complete description of dilution series runs is presented and a lowest detectable limit is established for these devices.

Chapter 5, discusses how enhancement of sensitivity is important for Nanowire biosensors. It details how other groups have endeavored to increase the same via different methods and there present short comings. Finally the sensitivity enhancement via application of static E-fields is discussed and presented as a viable means of increasing sensitivity of these devices.

Lastly, Chapter 6, concludes the thesis work and presents future directions for both of the piezoelectric micro-mechanical resonator and silicon nanowire based biosensor - platforms. It discusses the shortcomings and suggests methods of improvement.

Chapter 2

Wireless Actuation of Micro-mechanical Piezoelectric Resonators

2.1 Introduction

Wireless energy transfer was first introduced to the world in 1890's when the great inventor Nikola Tesla demonstrated it at the Chicago's World Fair. His genius demonstration at the time must not have been short of pure magic to the many in attendance. He had his audience hold large bulbs in there hands not connected to any wires. Then with the flick of a switch he turned them all on. It is described that the audience was in awe, some were running around like mad men, some frozen in place, dumbfounded, in all of their hands were light bulbs connected to nothing and yet were incandescent [Tesla, 1914]. The principle however is well understood for over a hundred years now and present in most high school textbooks. He used magnetic induction where by a large magnetic coil energized the secondary coils attached to the light bulbs.

Wireless energy transfer consists of energy transfer from an appropriate source to an energy-consuming device [Kurs et al., 2007] - such as implanted biomedical devices and sensors [Ho et al., 2014, Mei and Irazoqui, 2014, Chow et al., 2011, Zimmerman et al., 2006,Kim et al., 2013] without the use of physical conductors or solid connecting wires. Predominantly, wireless energy transfer can be realized via either magnetic (B-field) or electric field (E-field) coupling between the source and receiver. Mechanisms

involving the inductive coupling of magnetic fields require the short-range placement of an external (source) and an internal (receiver) coil. While, on the other hand wireless actuation mechanisms involving E-field coupling allow the source and receiver antennas to be proximately located. At present, however E-field coupling for wireless energy transfer is mostly carried out through micro-fabricated LC circuits and the incorporation of highly efficient radio frequency rectifying circuits at the receiver end.

Wireless energy transfer is however of both fundamental and technical interest, since it opens up a wide range of possibilities of remotely powered consumer electronics and bio-implants to sensors and actuation devices for which hard-wired connections are not possible or feasible. Wireless powering can also aid in fundamental experiments, where heat carried by the electrical wires in standard actuation techniques is detrimental to maintaining the resonator in a quantum state.

Biomedical devices that are implanted in the body (to measure various physiological parameters) or in the brain (for deep brain stimulation) have, in recent years, seen a considerable decrease in form factor. However in all cases these implants need to either be placed directly under the skin to be powered via magnetic induction or have to be hard-wired to battery packs placed elsewhere inside or outside the body.

In this chapter micro-mechanical piezoelectric resonators are introduced as possible devices for possible wireless powering applications. The resonators are modeled in COMSOL Multiphysics to demonstrate the wireless actuation mechanism. Then the successful actuation of these micron-sized silicon-based piezoelectric resonators with resonance frequencies ranging from 36 to 120 MHz at power levels of nano-watts and at a distances of about 3 feet, including comprehensive polarization, distance and power dependence measurements is presented.

2.2 Mechanical Resonators

The micro-mechanical piezoelectric resonators being used in this thesis are acoustic devices, which rely on the propagation of an acoustic wave through the device material for realization of their purpose. Acoustic resonators have been used since the pioneering work of Gunter Sauerbrey in 1959 [Sauerbrey, 1959] who demonstrated both through experimentation and theory the frequency shift in resonant frequency of a resonant quarts crystal oscillator. Previously, quartz crystal oscillators had been developed as radio frequency references for the National Bureau of Standards by the Naval Research Laboratory and Bell Labs, with temperature controlled, 100 kHz references in use by 1929 [Brown and Gallagher, 2011]. Since then acoustic resonators have been used for various functions.

Chapter 3 will elaborate on the types of acoustic waves that propagate within the thin-film resonators used in this thesis. For the current discussion it may be noted that the resonators used are rectangular beams of primarily silicon overlaid with piezoelectric material, sandwiched between two electrodes and connected to the bulk via thin-connects. The piezoelectric material is used to actuate and detect a response from the resonator. More on piezoelectric materials in Section 2.3

The two most common structures in mechanical resonators are the double-clamped beam (anchored at two points) and the cantilever (anchored at one point). Both are studied and based on the Euler-Bernoulli theory of beam approximation. Since the beams for both structure are extended non-rigid objects, continuous mechanics has to be applied in order to calculate stress and strain distributions. The Euler-Bernoulli equation describes the deflection of a solid due to an applied load. Using this as well as Hooke's Law one can determine the spring constant for a given geometry. The boundary conditions for such a problem (clamped-beam or cantilevers for example) are set during fabrication, and the load distribution which results during actuation

and sensing determine the exact response. The frequency for each of the resonant acoustic modes can be derived from the Euler-Bernoulli equation. Most common modes for micro-mechanical resonators include flexural, longitudinal, torsional and thickness. For a more in depth discussion the reader should also consider the work of Cleland [Cleland, 2013].

The resonators used in this work have been pre-fabricated off-site and were not designed or fabricated at BU hence an exhaustive study of the theory is not included. What needs consideration however is that the resonator response can be considered to be (and for simplicity of discussion) similar to that of a damped harmonic oscillator, which for a one dimensional forced-damped harmonic oscillator can be described as,

$$\ddot{x} + \gamma\dot{x} + \omega_0^2 x = \frac{f_0}{m} e^{i\omega t} \tag{2.1}$$

where x is the displacement of the beam, γ is the damping coefficient, ω_0 is the natural frequency of the system in (rad/s), ω is the drive frequency, f_0 is the driving amplitude and m is the mass of the beam being considered. The forcing function is on the right-hand-side of the equation. The stationary solution for Equation 2.1 can then be written as,

$$x(\omega) = \frac{1}{\omega_0^2 - \omega^2 + \frac{\imath\omega_0\omega}{Q}} \frac{f_0}{m} \tag{2.2}$$

where Q is known as the quality factor and is given as:

$$Q = \frac{\omega_0}{\gamma} \tag{2.3}$$

The quality factor (Q) is a characteristic of a resonator and qualifies its resonance frequency (ω_0) with respect to the full-width half-maximum (FWHM) ($\triangle\omega$) of its Lorentzian response (discussed shortly). The inverse of Equation 2.3 (inverse of the

quality factor) qualifies the dissipation in the system. For resonator systems higher quality factors are preferred which dissipate lower energy. Higher quality factors also reduce the mechanical and electrical noise that can couple into the devices. A higher Q also allows for more accurate frequency measurements. Since many sensors rely on frequency shifts as the method of sensing, this being one of the most precise measurements possible. It is common for a frequency to be measured with eight-digit accuracy, a feat not possible for amplitude or dissipation. Lower dissipation also means lower energy consumption and impoved signal to noise ratio which is important for signal processing and in communication applications. Dissipation sources and mechanisms can be categorized depending on their nature [Imboden and Mohanty, 2014]. They may be bulk defect effects, surface effects or external sources. Some are temperature sensitive, while others are geometry dependent.

The response for the driven harmonic oscillator of Equation 2.1 can be written as the amplitude and phase,

$$x(t) = x(\omega)cos(\omega t + \phi) \tag{2.4}$$

with,

$$x(\omega) = \frac{f_0/m}{\sqrt{\left(\omega_0^2 - \omega^2\right)^2 + \omega_0^2\omega^2/Q^2}} \tag{2.5}$$

and,

$$\phi = arctan\left[\frac{\omega_0\omega/Q}{\omega^2 - \omega_0^2}\right] \tag{2.6}$$

It may be noted that the resonance response of the resonator from Equation 2.5 would increase unbounded if it were not for the f_0/m term in the numerator which binds it to a finite value. This as we shall see later in this chapter is the equivalent

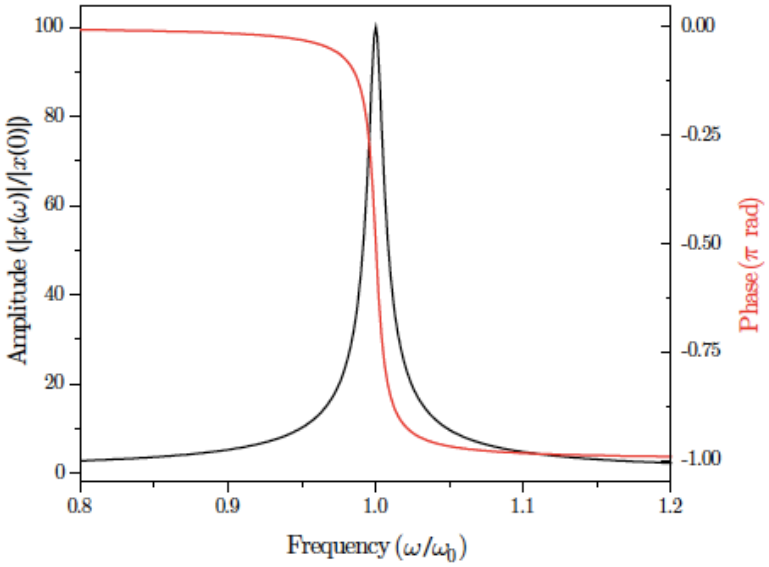

Figure 2·1: (black) Normalized amplitude $x(\omega)/x(0)$ response as a function of drive frequency. (red) Phase response as a function of drive frequency. Q for this system is about a 100

resistance that the resonator feels to its motion. In the meanwhile Figure 2·1 shows a typical resonance response for a resonator. The curve in "black" shows the Lorentzian amplitude response while the curve in "red" represents the phase of the response as it lags behind the forcing function. The phase goes through a 90-degree transition at resonance.

2.3 Piezoelectric materials

The piezoelectric effect is manifested as two accompanying inverse and direct effects. The former effect results in a mechanical strain upon the application of an electric field across the material i.e. the material flexes, whereas the latter results in an electric charge polarization in the material upon the application of a strain. The inverse and direct effects are, in turn, used to excite and measure the response of a piezoelectric resonator, respectively.

The piezoelectric effect was first observed in 1880 by the brothers Pierre and

Jacques Curie. Since then piezoelectric materials have found application in power sources and generators where reciprocal motion like walking or pumping of the heart etc. could be used to harness energy for powering small devices [Dagdeviren et al., 2014, Ferrari et al., 2015, Caliò et al., 2014, Jung et al., 2015, Platt et al., 2005]; in sensors with a wide variety of applications such as microphones which detect pressure variations in the form of sound, force sensors, pressure sensors, acuosto-optic modulators, valves and in ultrasonic transducers for medical imaging and industrial non-destructive testing (strain guages), [Gautschi, 2002, Zhang and Yu, 2011, Zhang, 2006]. These materials are also used in piezoelectric motors where the less-than-micron-deformation of the crystal (due to the inverse effect) is used for the precision/nano positioning in Atomic Force Microscopy (AFM) [Hemsel and Wallaschek, 2000, Dong et al., 1995, Morita, 2003]. More recently piezoelectric resonators have been fabricated [Chen et al., 2015] for timing applications in electronic components which have seen a great reduction in form factor. These resonators usually have a high Quality factor (Q) which is a measure of the energy stored in the system to that which is dissipated within it during each cycle. A high Q ensures that the resonance peak will be sharp and the Full-width at half maximum (FWHM) will be low.

There are many naturally occurring and man-made piezoelectric materials. Some natural piezoelectric materials include Berlinite (structurally identical to quartz), cane sugra, quartz, collagen, DNA, Rochelle salt, topaz, tourmaline and bone (dry bone exhibits some piezoelectric properties due to the apatite crystals, and the piezoelectric effect is generally thought to act as a biological force sensor). Some examples of man-made ceramic piezoelectric materials includes Lithium Niobate ($LiNbO_3$), Barium Titanate ($BaTiO_3$), Aluminum Nitride (AlN) and Lead Zirconate Titanate (PZT). In recent years, growing concerns due to toxicity of lead-containing devices there has been a push to develop Lead-free devices. While PZT is still used Aluminum

Nitride (AlN) is preferred by foundries and researchers due to its reasonable piezoelectric coefficient d_{33} of 5.15 pm/V, low permittivity (ϵ_r) of about 9 and high acoustic velocity which is advantageous because, in general, materials with high acoustic velocity tend to have high Quality factors (Q) and thus low dissipation. In addition AlN also has excellent thermal and chemical stability and can be sputtered in controlled layers on top of a MEMS device with the c-axis (axis of maximum deformation) pointing perpendicular to the plane of deposition. Since piezoelectric materials are anisotropic (direction dependent properties), this allows for maximum displacement in the direction perpendicular to the device surface which is what is needed in most devices especially micro-mechanical resonators.

2.4 Piezoelectric Resonators and Patch Antennas: A symbiosis

The optical micrograph (re-colored) in Figure 2·2 shows the top view of Device A, while Figure 2·3 shows a similar view of Device-B, both of which are the two devices we will be discussing in the demonstration of wireless actuation. However it may be pertinent to add here that similar actuation has been carried out and recorded on multiple other similar resonator devices.

The resonator shown is a rectangular plate type resonator - so called due to the shape of the suspended central structure. The rectangular resonator stack is realized by suspending a bottom base layer of structural silicon with subsequent layers of Silicon Oxide followed by a gold-ground layer, a layer of piezoelectric material (aluminum nitride AlN) and top gold electrodes. The top gold electrodes are patterned as, finger-like, interdigitated transducers (IDT's). Four of these IDTs are connected to the tab marked as "RF-1" through thin connects on one side, while the remaining four (IDT's) are connected similarly to the tab marked "RF-2" on the opposite side.

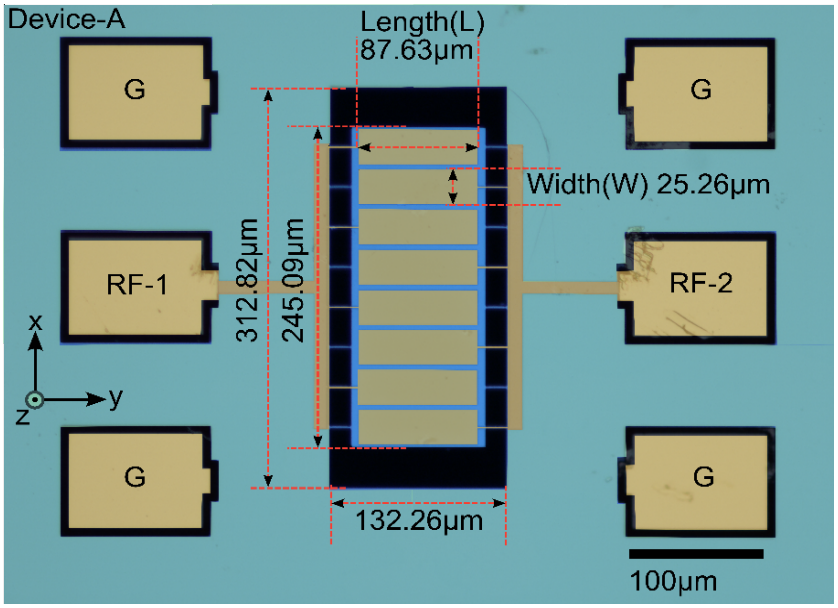

Figure 2·2: Re-colored micrograph showing top view of Device A, also used for the wireless actuation experiments. The central rectangular resonator element is about 88 by 245 μm $\pm$ 1μm

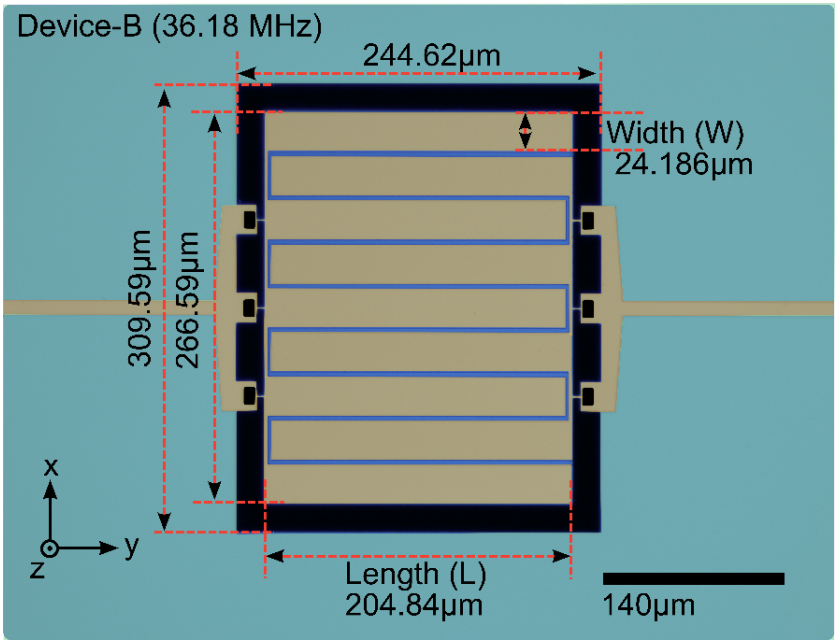

Figure 2·3: Re-colored micrograph showing top view of Device B used for the wireless actuation experiments. The central rectangular resonator element is about 204 by 266 μm $\pm$ 1μm

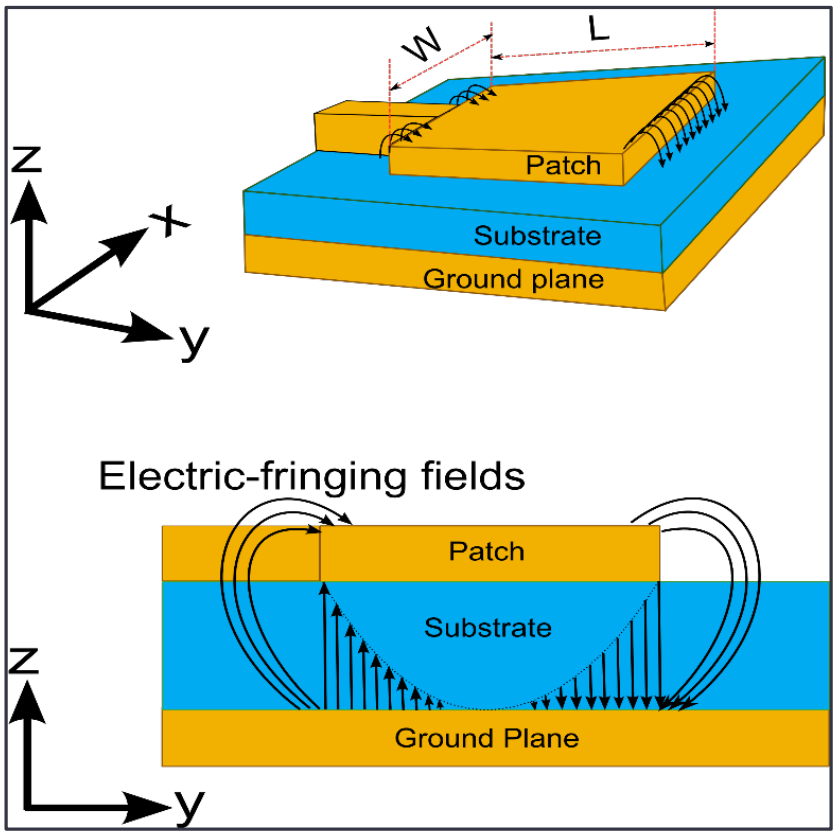

Figure 2·4: Two schematic views of the working of a typical patch antenna and fringing E-fields due to excess charge accumalation in the top and bottom electrodes.

The four gold tabs marked "G" are connected to the common ground layer of the device.

Typically, in hard-wired measurement scheme, an input alternating signal is applied across these top (IDT) and bottom (ground) electrodes to piezoelectrically actuate the resonator, while an output signal is measured across the corresponding set of IDT-electrodes and the ground plane. It may be noted that the devices are symmetric with respect to input and outputs so an input signal can be applied between the "RF-1" and "G" tabs on one side while an output can be measured across the "RF-2" and "G" tabs on the other side. The hard-wired connections can be provided through wire-bonding.

A typical patch antenna, as shown in the schematic in Figure 2·4, consists of two parallel conducting plates separated by a dielectric material. The patch antenna works when the horizontal component of the fringing electric fields line up due to opposing current directions in the top and bottom planes. Maximum radiation (and reception) happen in the direction perpendicular to the plane of the patch antenna (z-axis in Figure 2·4). The thickness of the dielectric is chosen to the smaller than the wavelength of the radiation to the transmitted or received while its permittivity (ϵ_r) is also chosen to be as low as possible for increasing fringing fields. In addition the length of the patch (L) (along the y-axis in Figure 2·4) is also chosen to be lesser than the wavelength, thus assuming that the dielectric extends infinitely beyond the patch. The length of the patch antenna and the relative permittivity of the dielectric characterize its resonance frequency (f) approximately as given as,

$$f \approx \frac{c}{2L\sqrt{\epsilon_r}} \tag{2.7}$$

For Device-A which has a patch antenna (top-electrode) length L of 87.6 μm and ϵ_r of the substrate (AlN) taken as 9.0, has a resonant frequency given by Equation 2.7 of 603.33 GHz (for detailed information refer Appendix B).

In the case of the resonator shown in Figure 2·2, each of the top IDT and bottom electrodes, along with the piezoelectric material (dielectric in our case) sandwiched between them, simultaneously functions as an inherent patch antenna, able to capture energy from an incident electromagnetic (EM) wave, and act as actuation (or detection) electrodes for the piezoelectric layer below. Patch antennas can couple to linearly polarized EM waves due to the fringing fields caused by excess charge accumulation (due to opposing current flows) at the edges of the top (IDT electrodes in our case) with respect to the bottom ground electrode. Hence for a resonator lying flat in the x-y plane as shown in Figure 2·5, with the IDT electrode length (L), par-

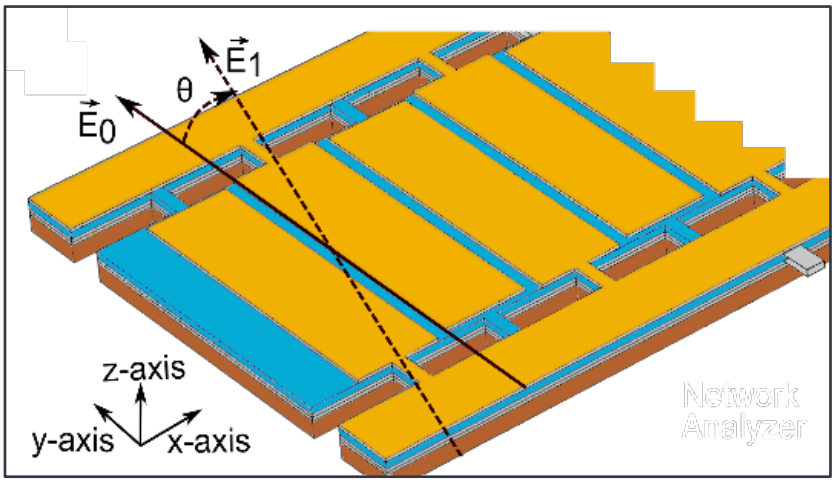

Figure 2·5: The patch antenna is linearly polarized and will receive maximum radiation from a similarly polarized E-field.

allel to the y axis, the top patch electrodes receive a maximum electric field from a normally incident electromagnetic wave polarized along the y axis. This time-varying electric field can produce a similarly varying electric potential between the top IDT's (patch antennas) electrodes and the ground plane below, resulting in a strain on the piezoelectric element (inverse piezoelectric effect) that may cause the resonator to actuate wirelessly.

2.5 Simulation Results

A typical patch antenna about 50 mm square (0.5 mm thick) was first simulated using COMSOL Multiphysics package. The patch is lying flat in the x-y plane while an E-field polarized in the y-axis is linearly incident on the patch. The resonance frequency of the simulation as depicted in the inset plot of Figure 2·6 is about 1.63 GHz while that given analytically by Equation 2.7 is about 1.632 GHz which are in good agreement. Appendix B details the exact calculations for the patch antenna.

Figure 2·7 shows the radiation pattern of the simulated patch antenna. As expected the main-lobe of the radiation pattern is in the direction of the positive z-axis,

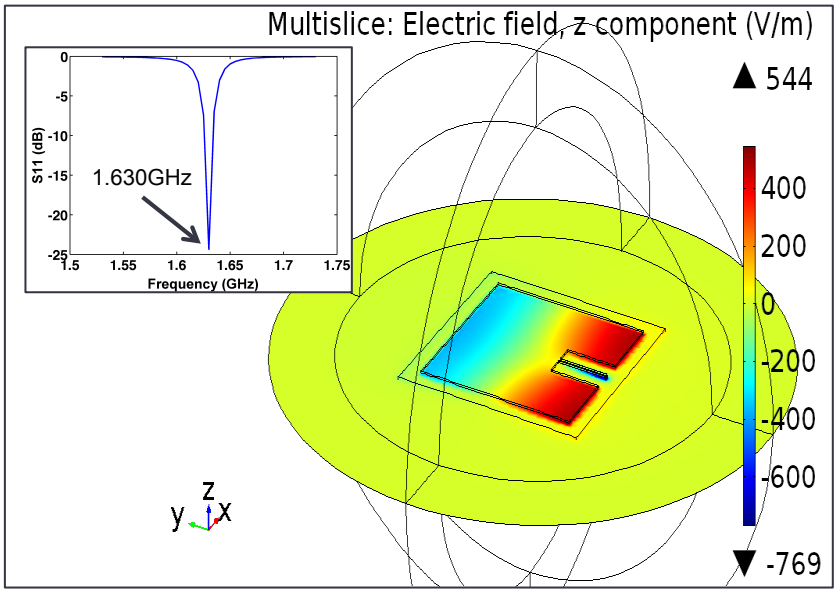

Figure 2·6: COMSOL simulation of a typical patch antenna (lying flat in the x-y axis) under normal incidence of linearly polarized E-field polarized along the y-axis as shown. Inset: S_11 plot depicts the reflection coefficient versus frequency. At resonance very little of the incident field is reflected.

perpendicular to the x-y plane containing the patch. This is as mentioned before, and expected. It may also be noted that a back lobe (diametrically opposite to the main-lobe) also exists in the negative z-axis. Minor-lobes and side-lobes are inadvertent artifacts of the antenna design and need to be minimized. In the present simulation however they are of no interest and can be ignored.

To confirm our hypothesis of wireless actuation of micro-mechanical piezoelectric resonators another model conforming to the dimensions of Device-A depicted in Figure 2·2 was developed in COMSOL. The piezoelectric-MEMS and EM-waves physics modules were used for this simulation. The simulation domain was chosen to be a rectangular box of 200 by 150 by 300 μm as shown in Figure 2·8 Port boundary condition was used to excite the E-field from the top-surface of the simulation box. The E-field was polarized in the y-axis and travelled in the negative z-axis direction (per the coordinate axis given in the figure). Scattering boundary conditions were chosen

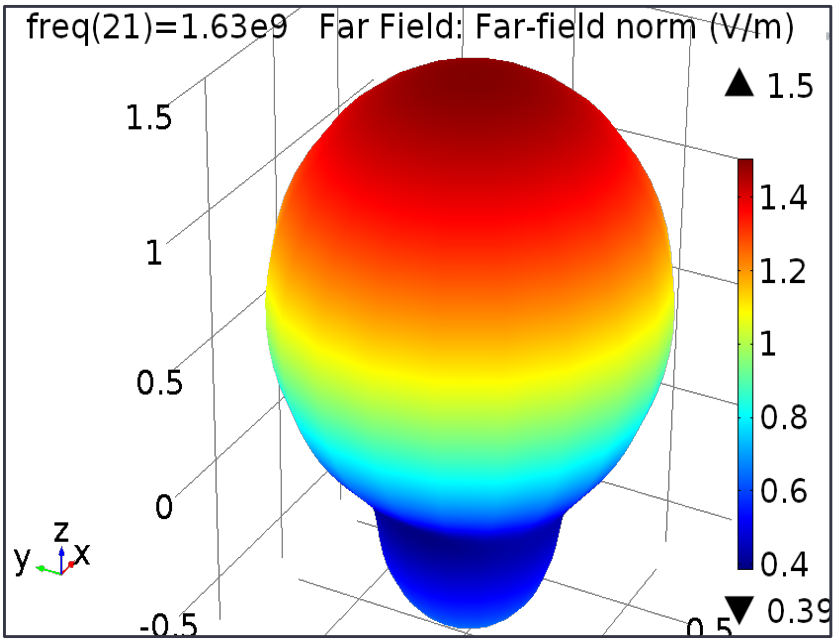

Figure 2·7: Radiation pattern of the patch antenna simulated using COMSOL Multiphysics package. The main-lobe extends in the positive z-axis which is perpendicular to the x-y plane of the patch antenna.

for all other sides of the cuboid to depict infinite domain.

The simulation uses the EM-wave module physics first to calculate electric field (E-field) components (E_x, E_y, E_z) in the computational domain comprising of approximately 84,000 mesh elements, from the inhomogeneous wave equation with sources (charges and currents) of the forms given below,

$$\bigtriangledown \times \left(\bigtriangledown \times \vec{E} \right) - \omega \epsilon_0 \mu_0 \mu_r \left(\epsilon_r - \frac{\iota \sigma}{\omega \epsilon_0} \right) \vec{E} = 0 \tag{2.8}$$

In the above $\vec{E}$ is the unknown electric field (V/m) to be solved in 3D, as mentioned before, ω is the angular frequency (rad/s), and μ_r, ϵ_r and σ are the relative permeability, relative permittivity and electrical conductivity respectively, specified by the properties of the material. In addition μ_0 and ϵ_0 are the permeability (H/m) and permittivity (F/m) of the free space, respectively. The above frequency domain form of the equation assumes that the resultant electric fields will be wave-like and

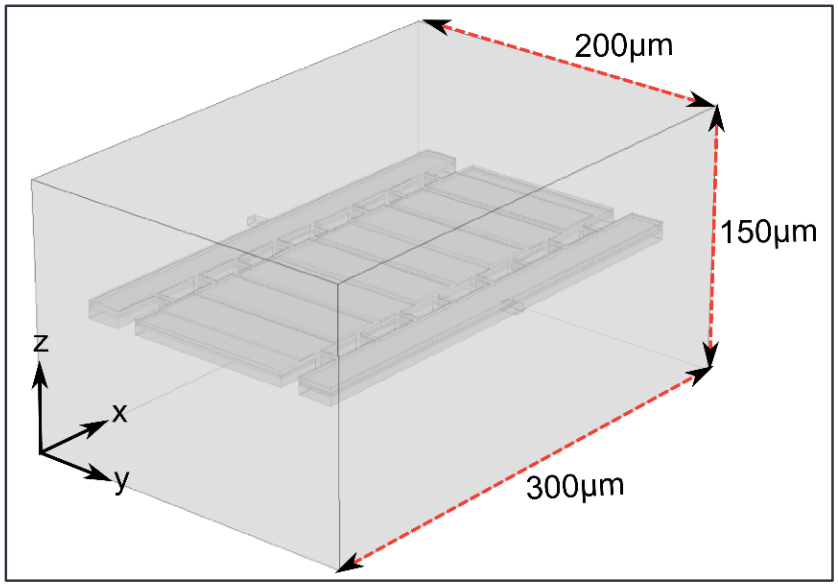

Figure 2·8: A model of Device-A was simulated inside a cuboid simulation domain in COMSOL to confirm the wireless actuation mechanism.

that the power transfer will occur primarily through radiation.

The piezoelectric physics module uses the E-field calculated throughout the finite simulation domain by the EM-wave module and sweeps the same frequency range (121.4 MHz to 122 MHz, step size of 0.05 MHz) to calculate the displacement of the resonator. The study at each frequency step utilizes the respective E-field solution from the EM-wave physics module to calculate the electric potential at the top patch electrodes, which is then provided as an input to compute the displacement of the resonator. It solves the following stress-charge form of the coupled piezoelectric equations, which are linear in the low E-field and mechanical stress regime,

$$\vec{T} = c_E \vec{S} + e^T \vec{E} \tag{2.9}$$

$$\vec{D} = e\vec{S} + \epsilon_0 \epsilon_{rS} \vec{E} \tag{2.10}$$

where S is the strain tensor of rank 2, T is the stress ($\mathrm{N/m^2}$) tensor of rank 2, E is the electric field (V/M) tensor of rank 1, and D is the electric charge density ($\mathrm{C/m^2}$)

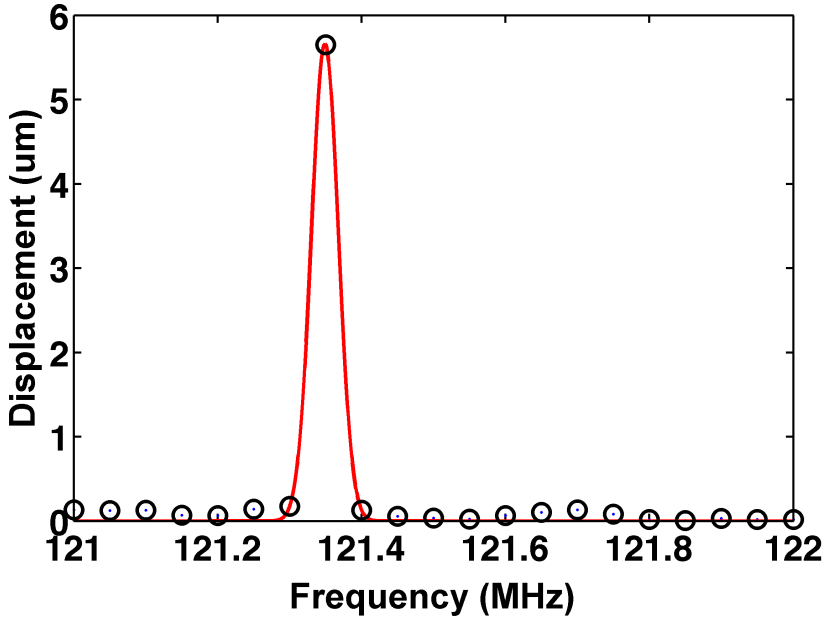

Figure 2·9: A resonance peak for the model of Device-A is observed around 121.3 MHz which is close the resonance of device A at 121.7 MHz.

tensor of rank 1. The material parameters c_E (tensor of rank 4), e (tensor of rank 3) and ϵ_{rS} (tensor of rank 2) correspond to the material stiffness (N/m^2), coupling properties (C/m^2) and relative permittivity at constant strain, respectively. In addition, ϵ_0 is the permittivity of free space (F/m) and e^T represents the transpose of the tensor e. Equation (2.9) describes the indirect piezoelectric effect, while equation 2.10 describes the accompanied direct effect piezoelectric effect.

The resonance peak shown at 121.3 MHz in the displacement vs. frequency plot of Figure 2·9 is slightly shifted from the actual resonance for Device-A which is about 121.7 MHz. While this may be due to approximations in the COMSOL model however it is close enough to demonstrate the wireless actuation principal.

2.6 Measurement Setup

In the lab the resonator device was setup as shown in the schematic of Figure 2·10 while Figure 2·11 shows the actual experimental setup. It may be noted that the resonance frequencies for Device-A and B are 121.7 MHz and 36.18 MHz, respectively. The micro-mechanical resonators (both Device-A and B) were wire-bonded to a printed circuit board (PCB) and tested successively to gather extensive distance and angular dependence data to verify wireless actuation. The PCB (containing the resonator) was mounted on a rotary stage and fixed vertically with its z-axis (as shown in Figure 2·10 and 2·11) pointing directly towards a transmitting biconical antenna. This transmission antenna produces planar EM-waves with a horizontally polarized E-field, parallel to the y-axis of the resonator. The rotary stage served to controllably sweep the resonator's in-plane (azimuth) angle-θ (Figure 2·10) from 0 to 330-degrees in 12-steps of 30-degrees each. Once complete set of such angular measurements was carried out at each of the ten distances between 6 and 36 inches from the fixed transmitting antenna, i.e, at 6, 8, 10, 12, 16, 20, 24, 28, 32 and 36 inches. These distances each fall within 1-wavelength (calculated at the resonance frequency) for both devices, which is about 2.5 m for Device-A and 8.3 m for Device-B.

Together, the data sets provided the angular and distance dependence of the wireless actuation of each resonator. We used a vector network analyzer (VNA, Agilent N3383) to record the S21 parameter magnitude and phase at each distance and angle data point. For all data points, the bi-conical antenna connected at port-1 of the VNA was excited at a fixed output power of -10 dBm (0.1 mW) and swept between 121.3 MHz and 122.4 MHz (201 points sweep) for Device A and between 32.5 MHz and 42.5 MHz (201 points sweep) for Device B respectively. The resonator output was recorded at port 2 of the VNA.

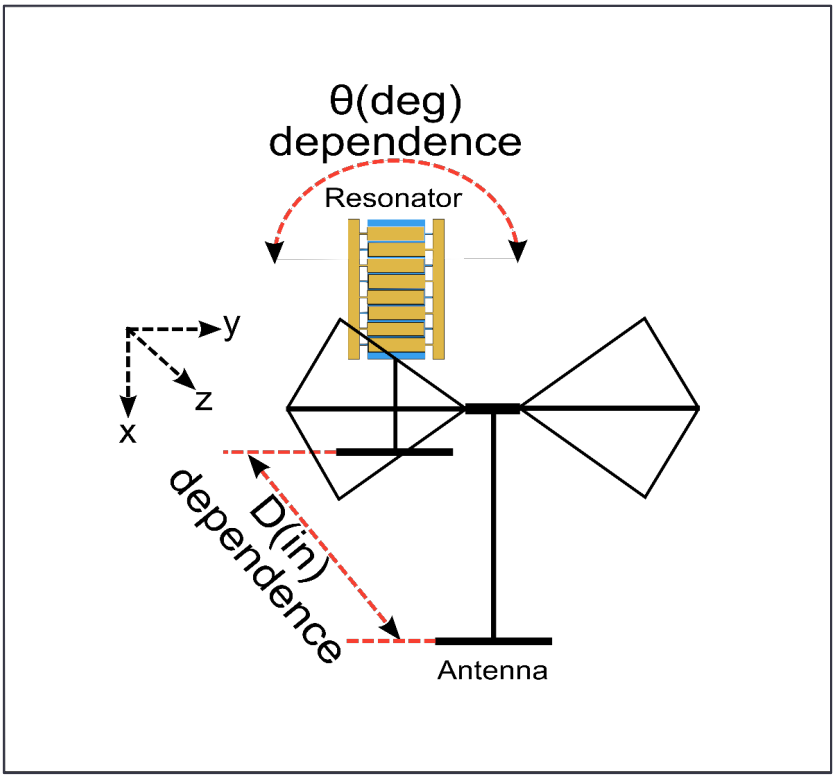

Figure 2·10: Schematic of the experimental setup for wireless actuation of Micromechancal Piezoelectric Resonators.

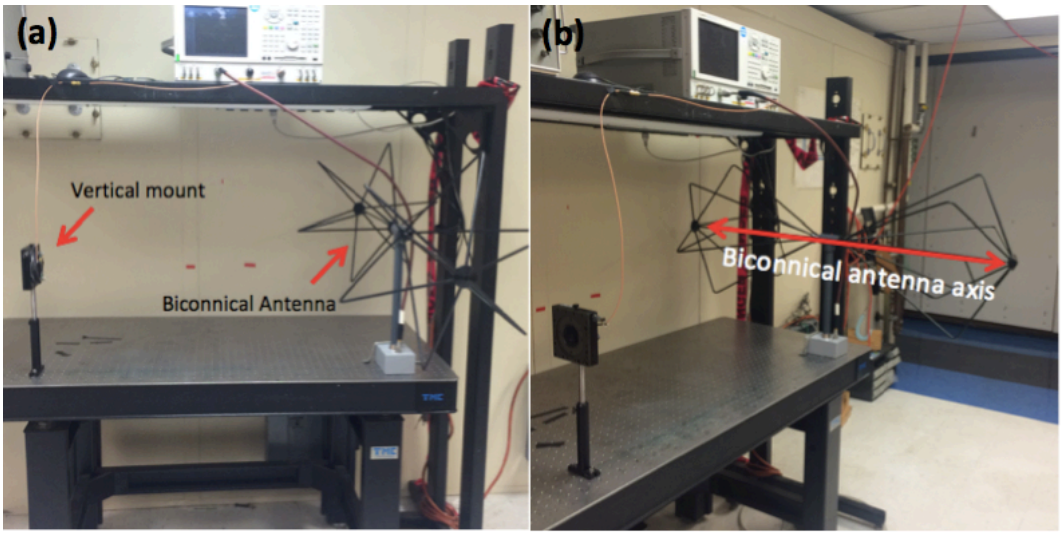

Figure 2·11: Two views of the experimental setup in the lab. The vertical mount contains the PCB (with the wire-bonded resonator) which is excited under wireless actuation via the biconical antenna. The VNA sits on the rack above.

2.7 Experimental Results

2.7.1 Wireless actuation - Simulation

Figure 2·12 provides a proof of principle whereby both devices depict wireless resonance responses at exactly the same resonance frequency as when tested under direct excitation. Figure 2·12 (a) and (b), provide the respective responses of both Device-A and B, when they are excited and their respective responses are measured via a VNA under what we call Direct-actuation. This direct-actuation is depicted in each of the inset schematic in both figures. Figure 2·12 (c) and (d), show the responses of both Device-A and B under wireless-actuation (setup as shown in Figure 2·11) at a fixed distance of 8-inches and angle-θ of 330-degrees for Device-A and at a distance of 20-inches and angle-θ of 300-degrees for Device-B. As the inset in each of these plots shows the VNA is now used to excite the transmission (biconical) antenna to sweep between the frequency ranges as mentioned afore, while the response of the resonator is noted by the VNA. It may be noted that while the resonator response under the wireless actuation for both devices is diminished in magnitude however the resonance frequency is exactly similar, in both cases to that of the direct-actuation scheme. This result is the basis of the wireless actuation mechanism and stands to experimentally demonstrate the same.

It is pertinent to add that similar results were obtained when the transmission (biconical) antenna was excited by VNA and the response of the resonator was recorded on a separate Spectrum Analyzer. However, this arrangement would not have conveniently yielded the required S21 parameter, which is customary for wireless systems and central to our own data analysis, hence the same VNA was used to both excite the source bi-conical antenna and measure the resonator response. The S21 parameter in high-frequency multi-port systems characterizes the forward transmission parameter and quantifies the power transmitted through to Port-2 with respect to the power

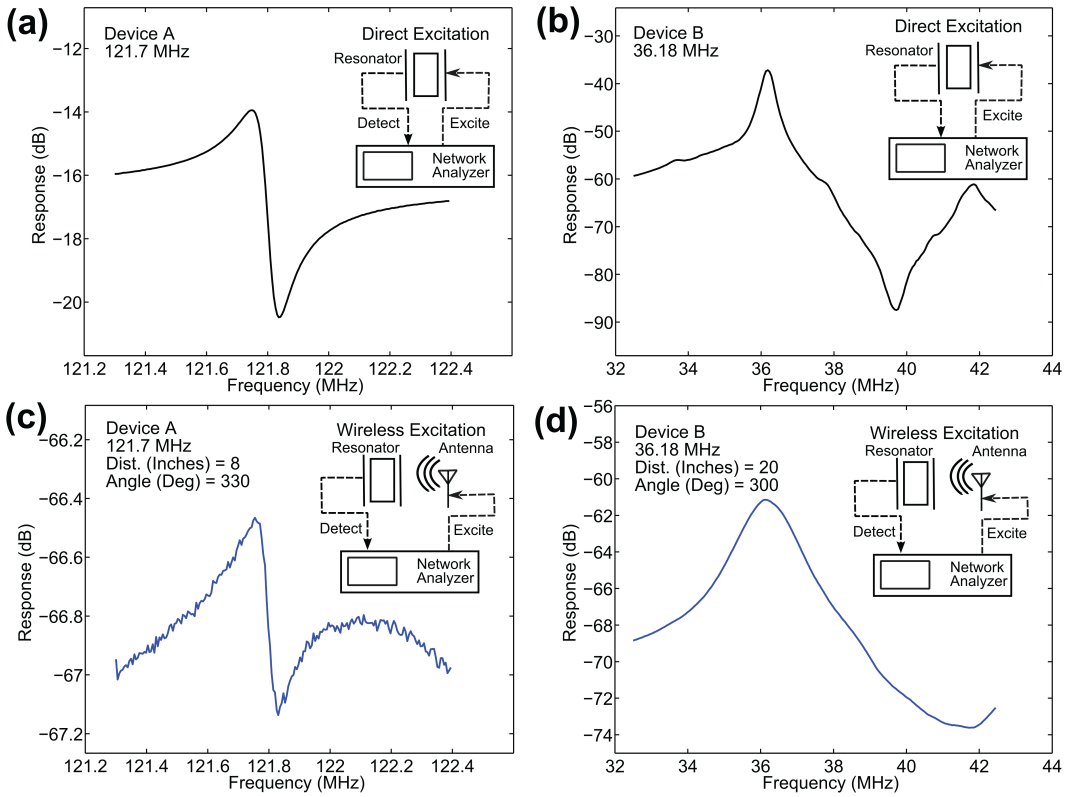

Figure 2·12: Direct and wireless actuation of both Devices A and B at fixed angles and distances is compared to demonstrate wireless energy transfer (actuation) of two separate piezoelectric devices. (a). Direct excitation response of Device-A (121.7 MHz). (b). Direct excitation response of Device-B (36.18 MHz). (c). Wireless excitation response of Device-A. (d). Wireless excitation response of Device-B.

supplied by the VNA at Port 1. The S21 parameter is recorded by the VNA for each distance and polarization angle-θ and for each frequency point swept.

While results of two devices (Device-A and B) are discussed here it may be noted that experiments were carried out on a number of different resonator devices and found to be in conformance.

2.7.2 Distance dependence

Micromechanical resonators are typically modeled as equivalent Butterworth Van Dyke [Enz and Kaiser, 2012] circuits consisting of resistive, inductive and capacitive

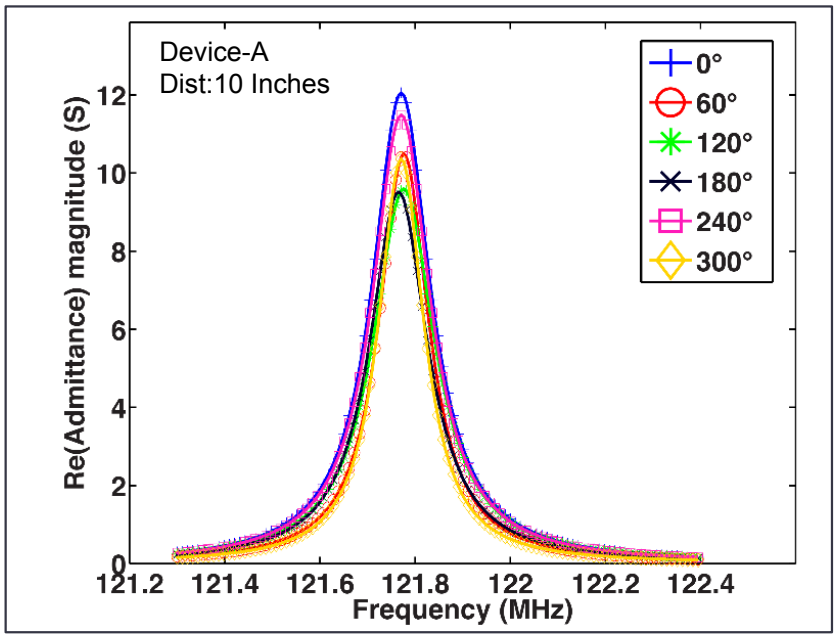

Figure 2·13: Distance dependence plot for Device-A is shown for six polarization angles (θ), for easier viewing.

elements (refer Appendix A for a complete derivation and analysis). Using this model the real part of the admittance (G_{BVD}) is extracted from the measured S21 parameter raw data. G_{BVD} (Siemens, S) is given as per the following equation,

$$G_{BVD} = \frac{R_m}{R_m^2 + \left(\omega L_m - \frac{1}{\omega C_m}\right)^2} \tag{2.11}$$

where R_m, L_m and C_m are the equivalent BVD circuit Resistance (ohms), Inductance (H) and Capacitance (F), parameters representing the mechanical motion of the piezoelectric resonator, while ω is the angular frequency (rad/s). The real part of the admittance (G_{BVD}) is the lorentzian response of the resonator and is plotted for each angle at every measured distance. One such plot of G_{BVD} is given in 2·13 for Device-A at a distance of 10-inches. The legend only shows six of the measured twelve polarization (θ) for clearer presentation. A clear polarization dependence can be seen from the resonance peaks.

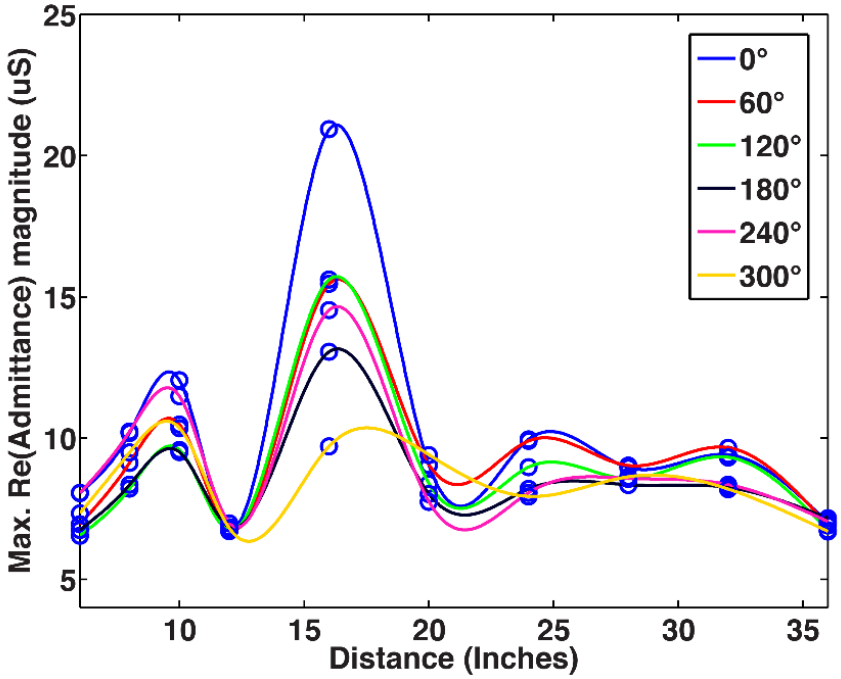

Figure 2·14: Plot of Real part of G_{BVD} vs. distance shown for six polarization angles (θ).

Using similar plots for all polarizations and distances measured we extract and plot the complete distance dependence for Device-A for all polarization angles (θ) in one plot shown in Figure 2·14. Theoretically we expect that such a plot should depict a monotonic decline as the distance of the resonator is increased from the fixed biconical antenna. The distance dependence of G_{BVD} for Device A however reveals a non-intuitive response. An anomalous maximum is observed for this device at 16-inches. A similar anomalous increase for Device-B is observed at 36 inches. While both devices do actuate wirelessly, an intuitive understanding of the distance dependence is difficult to form due to the near-field regime effects, reflections and multi-path interference of the linearly polarized systems.

The near field and far field are regions of the electromagnetic field (EM) around a transmitting antenna. The near-field is roughly the area within one wavelength of the frequency being transmitted, while the far field is everything beyond one-

wavelength. Far-field effects are well understood and the field strength in this region decreases inversely with distance from the source, resulting in an inverse-square law for the radiated power intensity of electromagnetic radiation. By contrast, near-field effects may cause rapid power declines which may vary with the inverse fourth and sixth-power of the distance. This however ensures that the near field effects essentially vanish within a wavelength approximately. However reflections and multi-path interferences may be enhanced in this region. As mentioned before the distances (6-36-inches) within which both Device-A and B were tested for wireless actuation, fall within one wavelength hence such effects are expected. In addition patch antennas (top-electrodes of the resonators) are linearly-polarized and hence are most receptive to electric-fields polarized along the length L (Figure 2·5). This would mean that we should only have a signal at 0 or 180-degree polarizations (Figure 2·14) however since there are signals at other polarizations it is easy to see that the linearly polarized patch antennas receive radiation at cross and other polarizations. This is actually expected since most linearly polarized systems are susceptible to cross polarization and multi-path reflections. In systems where such linearly polarized antennas are employed, cross-polarization and interferences are controlled by improving the directivity of the antenna. The directivity of an antenna is the ratio of the radiation intensity in a given direction from the antenna to the radiation intensity averaged over all directions. And one way of improving directivity is to operate the antenna at or in the vicinity of its resonance frequency. Taking Device-A as an example, and as mentioned before, the resonance frequency of the top-electrode patch-antenna are found to be about 603.33 GHz while the resonance of the resonator is about 120.7 MHz. Operating in the vicinity of the resonator's resonance, in the wireless actuation experiments, we are at least three-orders of magnitude below the resonance of the top-electrode patch-antennas, hence the low directivity of the patch antenna is expected.

However to explore the near-field regime effects we devised a COMSOL simulation of the physical lab experiment setup to observe a similar non-intuitive response like that observed in Figure 2·14. We assert that the non-intuitive response observed in our data is due to interference and reflections caused by the presence of reflective surfaces such as optical table, walls, reflective surfaces, data measurement equipment etc.

The COMSOL simulations, simulates the electromagnetic environment by measuring the power density at specified intervals (6 - 28 inches) for both an ideal and non-ideal situation. Two views of the lab setup are already presented in Figure 2·11 before. While all un-necessary equipments were removed from the vicinity of the experimental setup, nearby walls and racks however are fixed and cannot be removed.

The simulation calculates the power density (W/m^2) at each of the 6, 8, 10, 12, 16, 20, 24 and 28 inch distances from a fixed antenna source for both an ideal scenario (without the presence of any lab equipments, walls, optical tables etc.) and a non-ideal scenario which takes into account the presence of the immovable and essential lab data equipment. For simplicity a dipole, which is operationally similar to the biconical antenna - used in our experiments - is employed for the simulation. In addition the spherical domain for the simulation around the dipole antenna is halved via a symmetric plane, which serves to reduce computational memory requirements and time, while not effecting the results of the simulation.

Figure 2·15(a) and (b), shows the hemispherical computational domain where the power density measurements reveal a doughnut shaped (Figure 2·15(c)) far field radiation pattern of the typical dipole antenna, revolved about the axis of the antenna (z-axis of the simulation). Panel (d) of the same Figure shows the plot of the power density vs. distance (inches) and depicts an intuitive gradual decline response as the receiver (resonator) is moved away from the source.

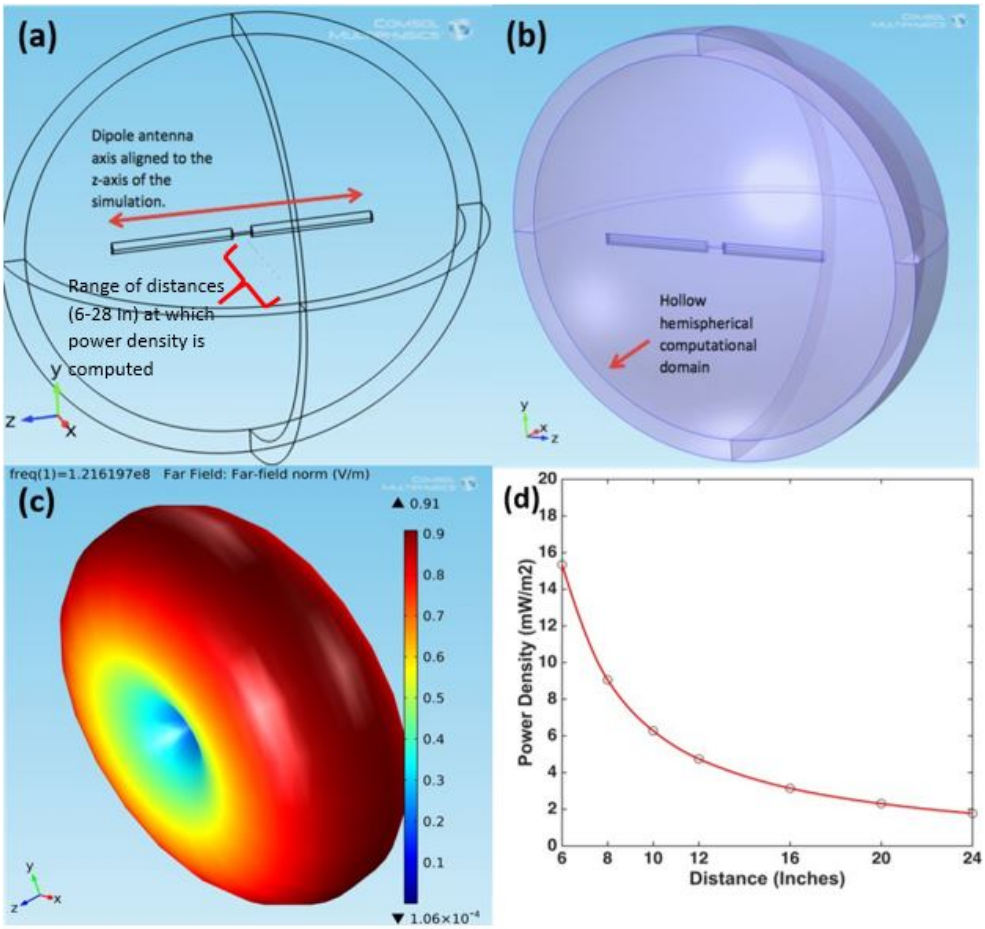

Figure 2·15: (a). The hemispherical computational domain and the model dipole antenna. (b). Another view of the hemispherical domain. (c). The resultant doughnut shaped radiation pattern of the dipole antenna (legend: Electric field (V/m)) (d). The power density vs. distance plot shows an expected and gradual decline.

Figure 2·16(a) and (b) show the simulation and results related to the non-ideal simulation which while calculating the power density (as before) also takes into account the presence of the optical table and rack, as seen in Figure 2·11 above. The lab equipment are modeled as reflective surfaces. Due to the presence of the reflecting surfaces the ideal doughnut shaped radiation pattern of Figure 2·15(c) above is distorted as seen in Figure 2·16(c) below. This causes a non-intuitive response in the Power density vs. distance plot shown in panel (d) of the Figure.

While the simulations performed are not to validate the results of the experiments but they do stand to provide an understanding that the presence of reflecting surfaces in close proximity of the wireless actuation experiments can cause non-intuitive responses observed in our data.

To further ensure that the non-intuitive response observed was due to the physical setup of the lab, the experiment (using Device-A) was conducted outside the lab in the open-air where the nearest reflecting surface was at least 15-20 wavelengths away from the resonator and source antenna setup with the exception of only the measurements equipments (VNA, stands etc) which had to be placed nearby. The results of G_{BVD} vs. distance for 0 and 180-degree polarizations in Figure 2·17 depict an approximate monotonic and intuitive decline. Thus providing credence to the assertion that the non-intuitive data observed is due to the presence of the reflecting surfaces near our experimental setup.

2.7.3 Angular dependence

The angular dependence for both Devices A and B also reveal interesting results. Since the transmission (bi-conical) and receiver (patch) antenna are both linearly polarized, the patch receives maximum of the incident E-field when its in-plane rotation angle θ coincides with the polarization of the incident field. As the in-plane angle θ of each device is varied between from 0 to 330 degrees, G_{BVD} is observed to vary

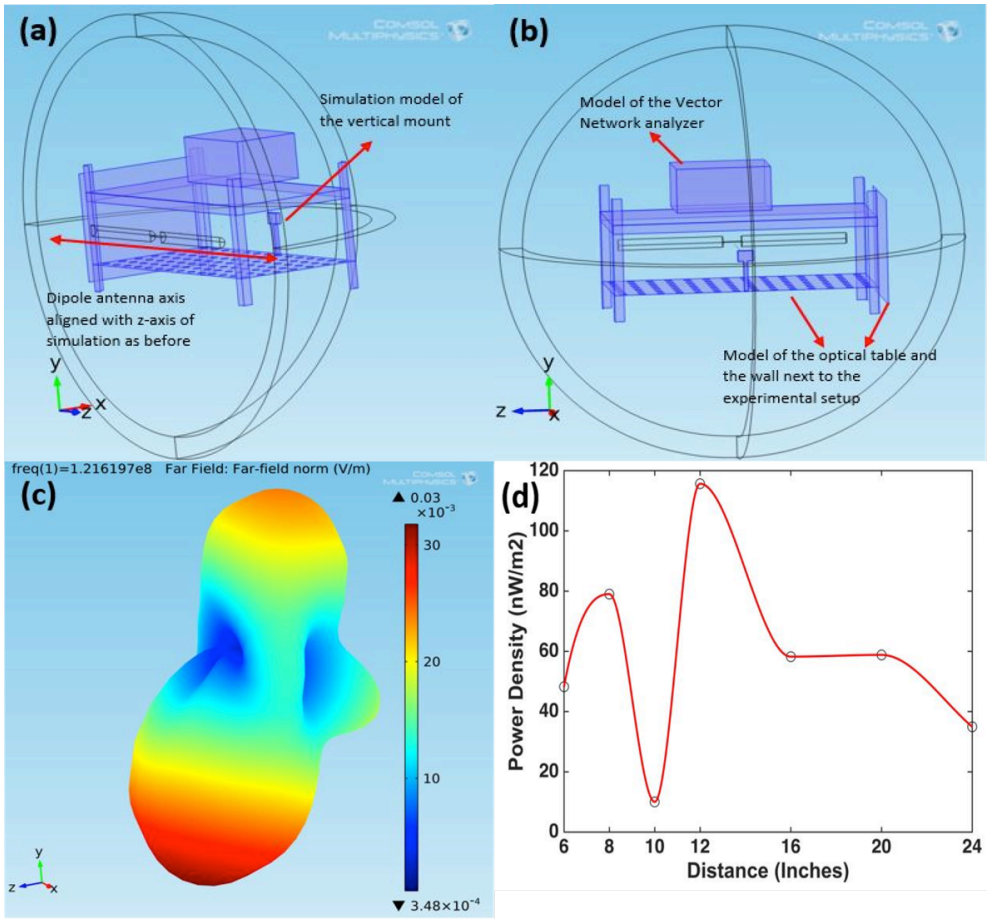

Figure 2·16: (a). and (b). Show the hemispherical computational domain containing the dipole antenna and models of the optical table, adjacent wall, top rack and VNA. Power density measurements are made at each of the distances between 6 - 28 inches. (c). The resultant distorted radiation pattern of the dipole antenna due to reflections and multi-path interference (legend: Electric field (V/m)). (d). The power density vs. distance plot showing un-intuitive response.

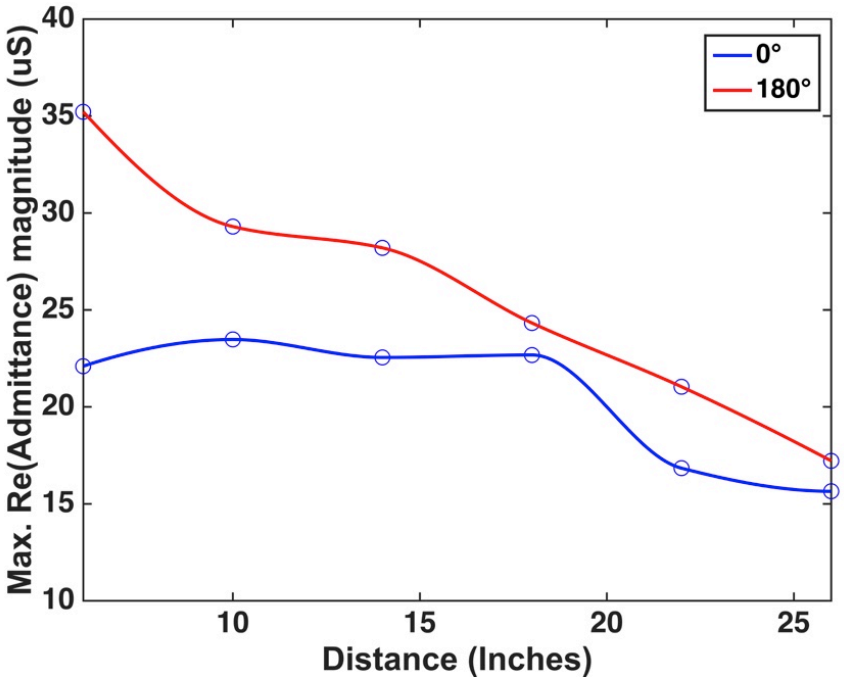

Figure 2·17: The G_{BVD} vs. Distance response (Device-A) for wireless actuation open-air experiments results for 0 and 180 degree orientation.

non-monotonically. This type of angular dependence is observed for both Devices A (as shown in Figure 2·18). As expected, an amplitude increase is observed at 0 degrees for Device A along with another at 270-degrees due to the susceptibility of linearly polarized systems to cross-polarization (as discussed before).

A similar non-monotonic result is seen for Device B. Furthermore, this behavior is found to be more pronounced for both devices at distances nearer (6, 8, 10, 12 inches) to the transmission bi-conical antenna. As the devices are moved farther away from the transmission antenna, beyond 12-inches amplitude peaks are observed at multiple angles which is due to the device response being overcome by the more predominant near-field and wave reflection effects, as shown in Figure 2·19. While it may seem contrary that the near field effects become dominant as the distance between the transmission antenna and the device is increased it may be recalled that all distances at which measurements were carried out fall well within 1-wavelength distance of the

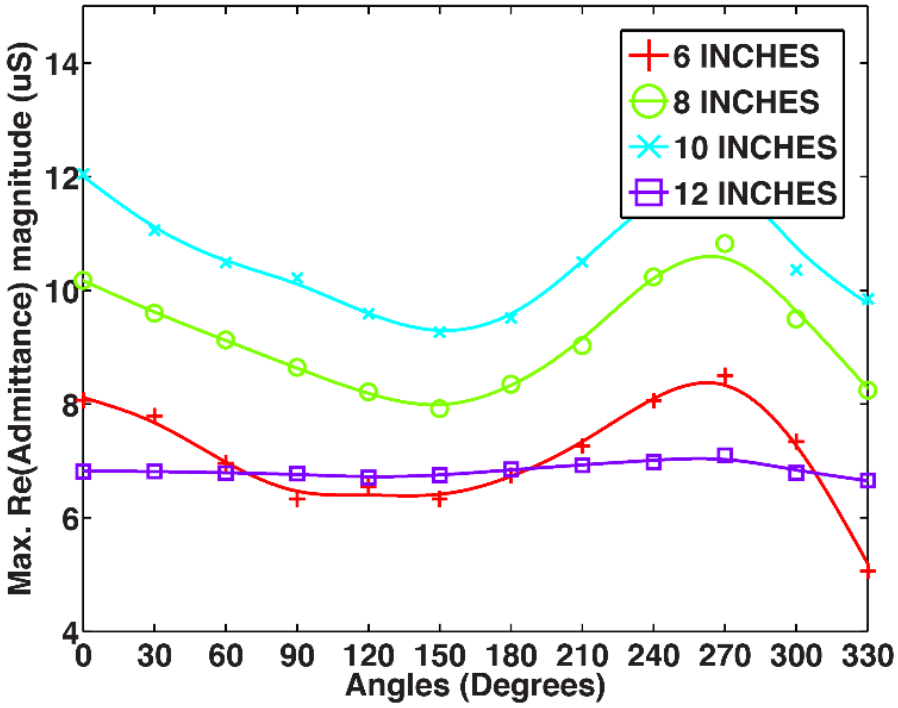

Figure 2·18: Angular dependence plot for Device-A is shown for first four distances, for easier viewing.

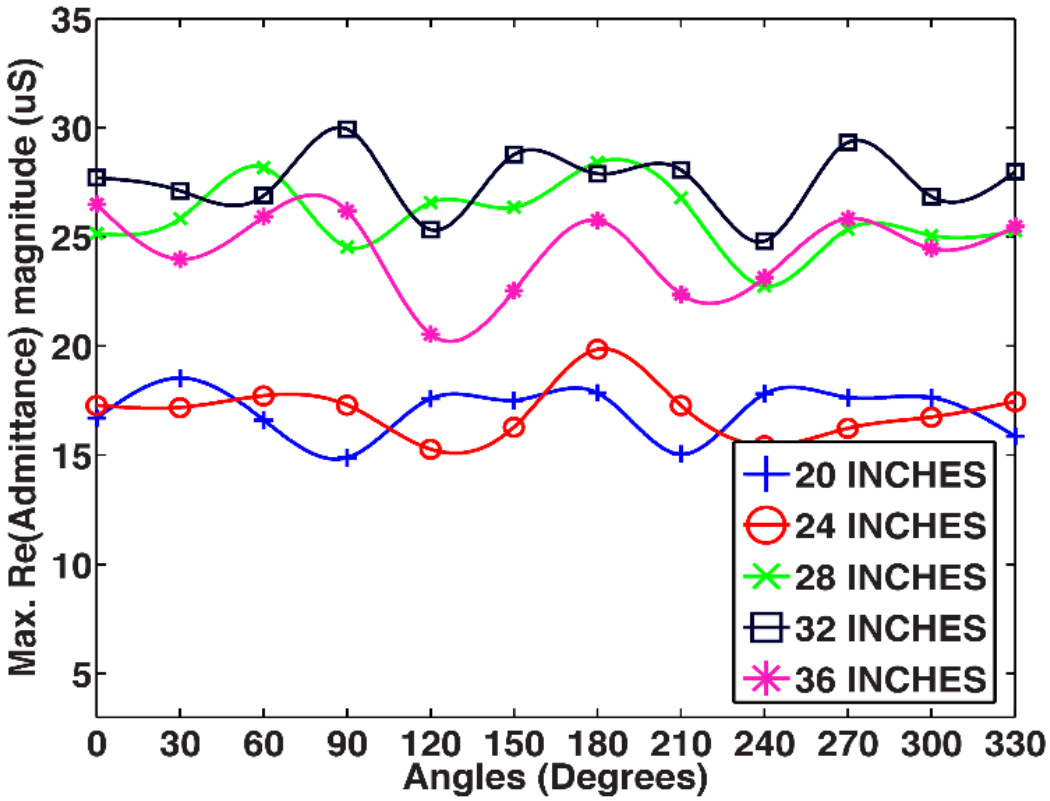

Figure 2·19: Angular dependence plot for Device-A is shown for four distances, further away from the transmission antenna.

devices hence near field effects remain dominant.

2.7.4 Power dependence

The studies and plots described up to this point, for both Devices A and B, were measured at a fixed EM-wave source (bi-conical) antenna output power of -10 dBm (0.1 mW). By fixing the distance and angle of both devices, in turn, we now investigate the lowest source antenna power, still able to generate a discernible resonance response. For this Device-A was fixed at 8 inches and 330 degree, while Device-B was fixed at 8 inches and 180 degrees, chosen at random. The source antenna power was swept, at the fixed resonance frequency for both devices respectively, between 15 and -75 dBm (31.6 mW to 31.6 pW). The resonance response was observed and recorded.

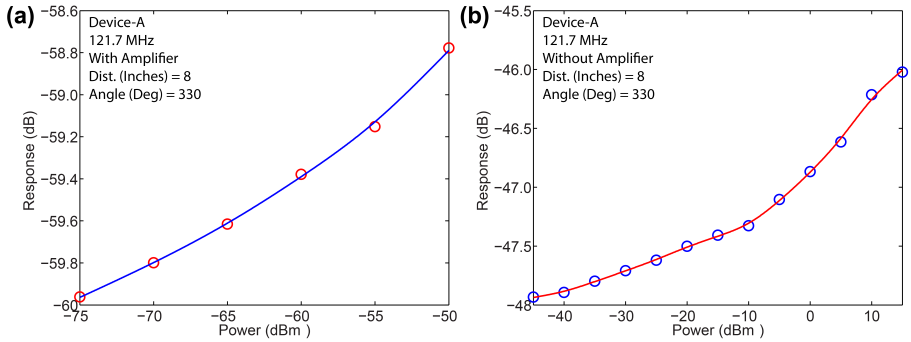

Figure 2·20: Power dependence plot for Device-A fixed at an angle of 330-degree and 8-inches from the transmission antenna.

A 35 dB-gain, low noise (MITEQ AU-1466) preamplifier was used to amplify the resonator response signals as the power was reduced below -50 dBm for Device-A and -45 dBm for Device-B. The guide-to-eye plots for Device-A shown in Figure 2·20 demonstrate that the resonance response amplitude decreases as the source output power is decreased. Similar results are obtained for Device B (not shown). Furthermore a separate similar power sweep experiment (results no shown) for Device A was carried out by fixing it at a distance of 10 inches and at an angle of 330 degrees, from the transmission antenna which resulted in a minimum power of actuation of -70 dBm (100 pW).

2.7.5 Efficiency

Efficiencies of both Devices A and B were calculated via the method detailed in Appendix B. Figure 2·21 shows the distance dependence of efficiency for Device A at a constant in-plane angle θ of 0- degrees. The incident input power to the device is calculated as the product of the measured power density at each distance by a portable handheld power meter (RF-Explorer 3G) and the effective area of the top patch antenna array. The output power is calculated from the S21-raw data response of the device measured by the VNA. The ratio of the output to input power reveals the maximum percentage efficiency which for Device A is nearly 3% at 16 inches, and

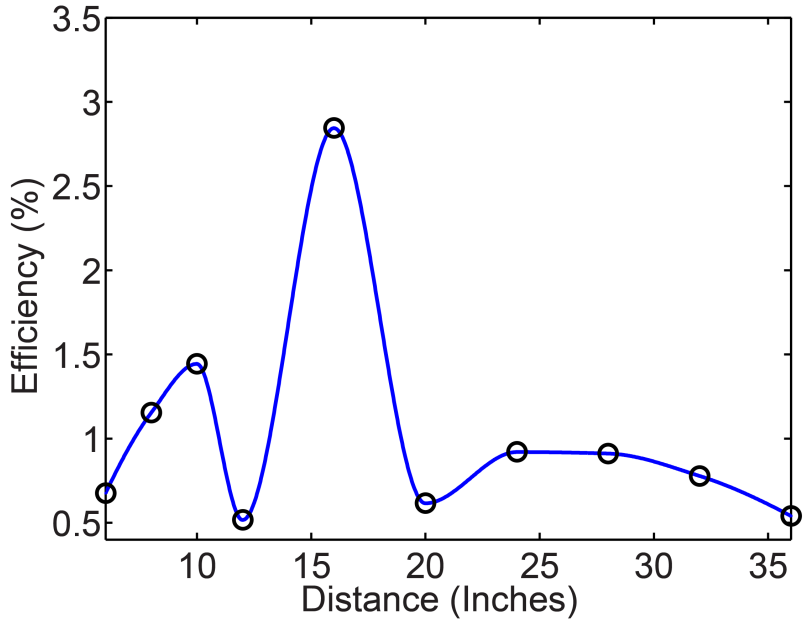

Figure 2·21: Efficiency plot for Device-A vs. distance.

for Device B it is 1% at 32 inches. The distance dependence of efficiency shows that near-field and wave reflection effects do play a role in enhancing or depreciating the received power by the resonator.

While it can be observed that Device-A (and similarly Device-B) has an output signal for nearly all distances and in-plane angle orientations, the efficiency, however, in these first measurements is low but it can be enhanced by at least an order of magnitude by appropriate design adjustments, which for instance, could result in bridging the gap between the resonant frequency of the patch antenna and the mechanical resonant frequency of the resonator thus resulting in a higher transfer of power and coupling between the incident electromagnetic wave and receiver device.

2.8 Conclusion

To summarize, we demonstrate wireless actuation of micro-mechanical resonators down to the level of 100 picowatt of excitation power at a distance of over 10 inches

and with 0.1 mW of excitation power up to a distance of 1 m. We observe that while the response may be non-intuitive it can be explained. What is more revealing is the fact that the device has a signal at all orientations and distances.

Such a low-power wireless excitation technique can pave the way for a host of fundamental experiments that require minimal heating and coupling, as in a quantum system, by the measurement setup. More importantly, these small footprint low-power devices, with appropriate design modifications, can be used as wireless power receiving element in biomedical micro-implants in the brain and the body, enabling a new generation of neuroscience studies that require local targeting with high spatial resolution.

Chapter 3

Wireless actuation: High Frequency Modes

3.1 Introduction

The previous chapter presented micro-mechanical piezoelectric resonators for possible wireless actuation of biomedical devices. One pertinent insight that was presented in it was the possibility of increasing the efficiency of the wireless actuation mechanism by bridging the frequency gap between the resonance frequency of the micro-mechanical resonator and the top patch antennas. This chapter presents how in fact this can be achieved and a maximum increase of nearly five-times may be achieved, without incurring any design modifications to the resonator or top patch antennas.

Also and as mentioned previously micro-mechanical piezoelectric resonators [Imboden and Mohanty, 2014, Gaidarzhy et al., 2007, Mateen et al., 2016, Imboden et al., 2013, Dorignac et al., 2009] employ inverse piezoelectric effect for actuation. An alternating (AC) electric field causes a mechanical strain in the material which excites an acoustic wave. Conversely, direct piezoelectric effect converts mechanical vibrations resulting from an acoustic wave into a proportional electric charge polarization, which can be used to sense said acoustic wave. As mentioned in Section 2.2 the Euler-Bernoulli equation can be solved for the different frequency modes of acoustic propagation in clamped beams, similar to the resonant structure of our micro-mechanical

resonators. By accessing a higher frequency mode of the micro-mechanical resonator the gap between the resonance of the top patch antennas and the resonator may be reduced as desired.

Conventionally, acoustic wave resonators have been confined to the realms of either Bulk Acoustic Waves (BAW) or Surface Acoustic Waves (SAW) resonators depending on whether the wave travels through the bulk (Figure 3·1) or on the surface of the resonator (Figure 3·2), respectively.

Bulk acoustic waves propagate through the bulk of a material including longitudinal wave, shear horizontal (SH) wave, and shear verticle (SV) wave. The longitudinal acoustic wave is also called P-wave (primary wave) and has the highest phase velocity. A thin-film BAW resonator is a device composed mainly from a piezoelectric thin film surrounded by two metal electrodes that generate the longitudinal wave propagating according to a thickness extension mode (TE).

BAW resonators fabricated out of piezoelectric materials in the sixties [Hickernell, 2003] have experienced skyrocketing development since the past two decades [Tsubouchi and Mikoshiba, 1985, Matsumoto et al., 2004, Lakin and Wang, 1980] due to their high quality factors (Q) which has enabled their use as electronic filter components in mobile communications [Grudkowski et al., 1980, Lakin et al., 1995]. Due to their high Q and resulting high sensitivity, BAW resonators are widely used as gravimetric sensors for measuring of various physical properties such as: temperature [He et al., 2012], pressure [Chiu et al., 2007], humidity [Qiu et al., 2010], and UV light [Qiu et al., 2011]. BAW resonators have also been used for chemical [Johnston et al., 2012, Pang et al., 2012, Lin et al., 2008] and biological sensing [Zhao et al., 2014, García-Gancedo et al., 2011, Zhao et al., 2012].

SAW resonators are also formed from piezoelectric layer but the acoustic waves travel along the surface of the material. Typically, these waves propagate as Rayleigh

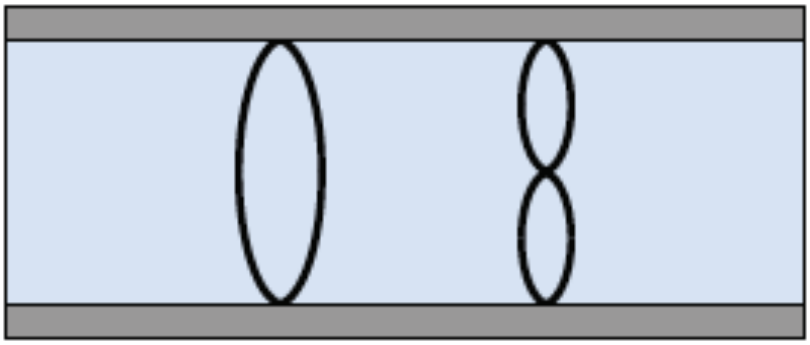

Figure 3·1: Schematic depicting propagation of BAW acoustic waves in the bulk of the material. First two modes are shown.

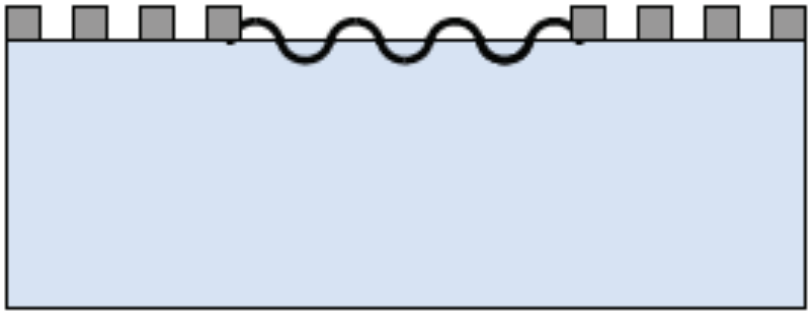

Figure 3·2: Schematic depicting propagation of SAW acoustic waves on the surface of the material.

waves, which comprise of particle displacement normal to the piezoelectric surface and have finite penetration depth. The SAW device was first reported by White and Voltmer in 1965 for a quartz plate [White and Voltmer, 1965], and both quartz and thin-film variants have since been employed commercially for use in electronic filters, delay lines, and pressure sensing applications [Fanget et al., 2011, De Klerk, 1975, Bao et al., 1987].

Since SAW resonators employ acoustic waves that travel on the surface and BAW resonators employ those that travel into the thickness of the material recently, thin plate modes called Lamb waves resonators (LWRs) have been developed. These waves are launched by interdigitated transducers like surface acoustic waves while the wave travels through the bulk of the material like bulk acoustic waves - in this manner Lamb Acoustic wave (LAW) resonators enjoy the benefits of both the earlier mature technologies. LAW resonators are easy to fabricate and foundry compatible. Lamb waves can travel over a long distance, confined by two parallel boundaries, and have found primary use in non-destructive testing applications. Thus for piezoelectric devices these acoustic waves are preferred for actuation and detection.

Pioneering work on Lamb waves was first explained in 1889, by Lord Rayleigh for wave propagation along a guided surface and the waves were known as Rayleigh waves [Rayleigh, 1885]. Following this work, Horace Lamb, a British applied mathematician, reported the waves discovered in plates in his historic publication, *On Waves in an Elastic Plate*, in 1917 [Lamb, 1917]. These waves since then have been called Lamb Waves.

Lamb waves are further classified into symmetric $(S_0, S_1, S_2...)$ or anti-symmetric $(A_0, A_1, A_2...)$, indicating the symmetry of a particles displacement relative to an imaginary median plane drawn through the thickness of the plate, as shown in Figure 3·3 and Figure 3·4 respectively. The symmetric modes are also called longitudinal or

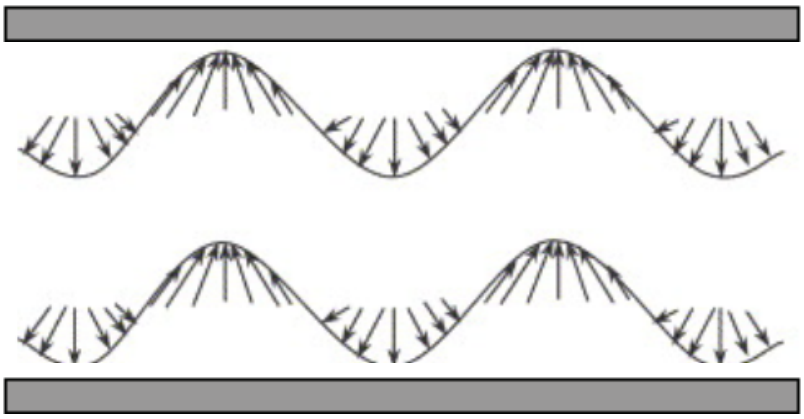

Figure 3·3: Schematic depicting propagation of Lamb symmetric mode waves.

contour modes because the average displacement over the thickness of the plate or layer is in the longitudinal direction. While the anti-symmetric modes are observed to exhibit average displacements in the transverse direction, these are called flexural modes.

The velocity of Lamb waves are dependent on its frequency. Each of the symmetric and anti-symmetric modes have their own frequencies and occur alternately as: $S_0, A_0, S_1, A_1...$, and so on. While the lower order modes are easily discernible the higher order modes are a super position of all the modes occurring before it and are harder to discern from shape.

Compared to SAW and BAW resonators, Lamb acoustic wave resonators fabricated from thin-film AlN are a recent innovation dating back to 2002 by the work of Piazza and Yantchev [Yantchev and Katardjiev, 2013]. The lamb waves propagate through the thin plate-type resonators used within this thesis and as they are reflected at the edge the mode of propagation don't suffer from mode conversion like SAW resonators do nor do they suffer from the multiple frequency mixing problem of BAW resonators.

LAW typically have high quality factors (Q), robust thermal compensation, low

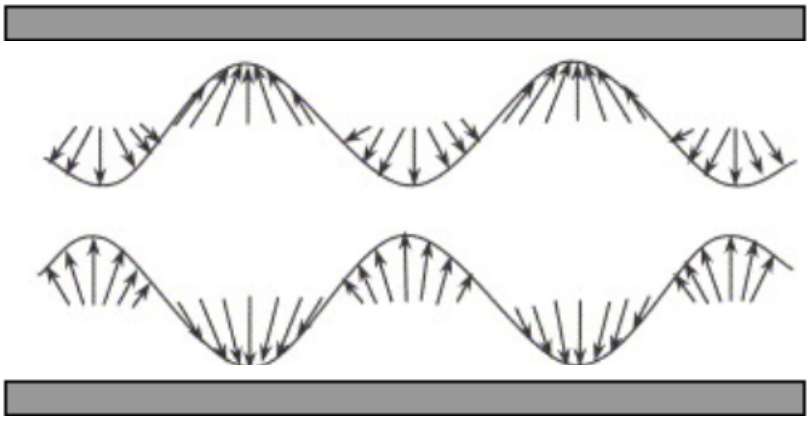

Figure 3·4: Schematic depicting propagation of Lamb asymmetric mode waves.

noise floor and high frequency of operation [Lin et al., 2012, Bjurström et al., 2005, Yantchev et al., 2006, Kuypers et al., 2008, Zhang et al., 2015, Lin et al., 2014]. These waves propagate in piezoelectric plates that are thinner in comparison to the wavelength of the wave being transduced by the Inter-Digitated Transducers (IDTs) patterned on top of the piezoelectric resonator. Suspension of the structure enables a higher Q and larger phase velocity (which enables higher frequency of operation). Due to their high phase velocity, weak dispersion, low susceptibility to mode conversion, and moderate electromechanical coupling, the lowest-order symmetric mode (S_0) has found most use in many practical fields such as high temperature sensing applications [Narducci et al., 2014], high frequency wireless communications [Abazari and Abbey, 2010], chemical and biological sensing [Lu et al., 2013, Chen et al., 2016],pressure and gravimetric sensing [Yantchev and Katardjiev, 2013, Choujaa et al., 1995], and structural health monitoring [Giurgiutiu, 2005]. Given the importance of the S_0 mode for practical applications, wireless excitation of this mode for a micromechanical piezoelectric resonator is demonstrated in this chapter. This S_0 mode has a frequency of about 356.2 MHz which is much higher than the resonance frequencies of Device-A and B of 121.7 and 36.18 MHz in Chapter 2.

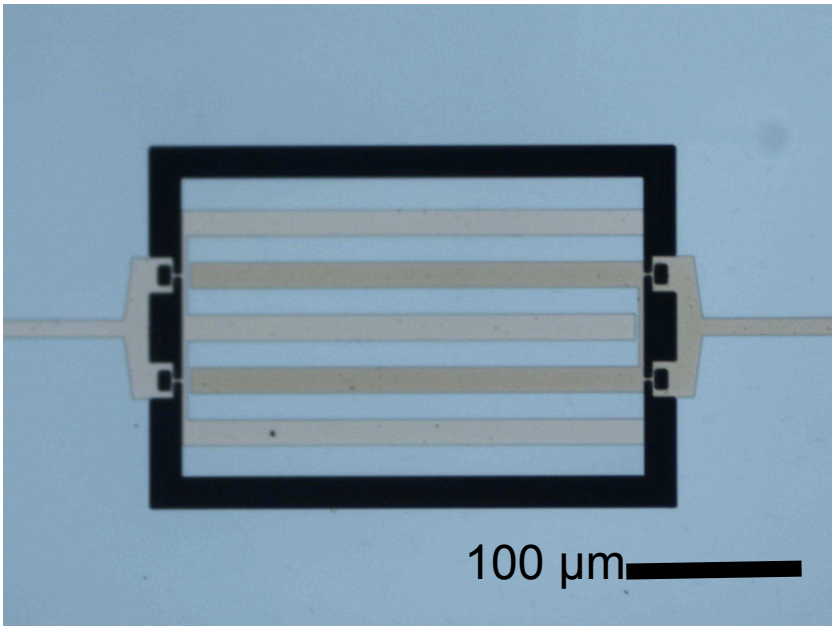

Figure 3·5: Top view of the micro-mechanical piezoelectric resonator. The plate-type piezoelectric element of the resonator has a lateral dimension of 266 by 166 microns. Five interdigitated transducers (IDTs) are overlaid on this element with three connected to the RF-1 tab (not shown) though thin connects on one side while the remaining two are connected similarly to the RF-2 tab (not shown) on the opposite side.

3.2 Simulation Results

Figure 3·5 is an optical micrograph showing the top-view of the MEMS piezoelectric resonator employed for this study. The central rectangular plate (shown in blue color) is the piezoelectric element of size 266 μm by 166 μm, which is suspended over a slightly larger rectangular cavity. The resonator is connected to the bulk material via thin rectangular connects. The top of the resonating element is overlaid with five, 15-μm wide, gold interdigitated transducers (IDTs), shown in dull gold color. Three of these IDTs are connected via a thin gold track to the RF-1 tab on one side (not shown) while the other two IDTs are connected to the RF-2 tab on the other side (also not shown) via a similar thin gold track. As before either RF-1 or RF-2 can be used to apply an AC-signal to piezoelectrically actuate the resonator while the other tab can be used to observe the device response. These resonators are fabricated by standard microfabrication methods. The total thickness of the resonator is 10 μm. From bottom to top, it consists of a 5 μm base polysilicon layer, a 1 μm layer of silicon oxide, a 1 μm layer of gold ground-electrode, a 2 μm layer of aluminum nitride (AlN), and a 1 μm layer of patterned gold top-electrodes. Wireless actuation of this device is carried out similarly as for those devices presented in Chapter 2.

A 2-D model conforming to the approximate dimensions of the device, shown in Figure 3·5, was developed and simulated using the piezoelectric module in the frequency domain of the COMSOL Multiphysics package. The simulation swept the frequency between 350 MHz and 370 MHz and calculated the deformation of the device at every mesh point. The results revealed a mode at 356 MHz, as shown in Figure 3·6.

The inset of Figure 3·6 depicts the deformation of the device resembling the mode shape expected from the symmetric Lamb wave mode S_0 (refer Figure 3·3).

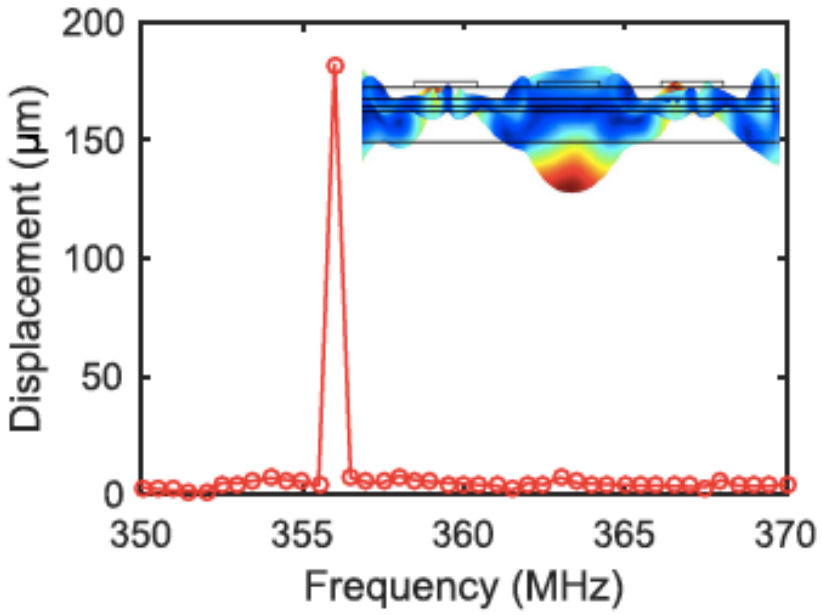

Figure 3·6: The displacement vs. frequency sweep plot produced by COMSOL simulation depicts a mode at the 356 MHz frequency. The inset depicts the symmetric lamb wave mode shape.

3.3 Theoretical calculations

The frequency f_l of the S_0 mode is theoretically calculated to be about 368 MHz and is dependent on the longitudinal velocity of sound v_l through the resonator structure of thickness d comprised of the layers as described before and given as in,

$$f_l = \frac{v_l}{2d} \tag{3.1}$$

The sound velocity v_l through the stack of thickness d is calculated to be about 7386 m/s using the relation,

$$v_l = \sqrt{\frac{E_l}{\rho}} \tag{3.2}$$

where, E_l is the longitudinal Young's modulus and ρ is the density of the stack. A Voigt model for weighted averages is assumed as a first-order approximation for the

Young's modulus of the stack given as,

$$E_l = E_1V_{f1} + E_2V_{f2} + E_3V_{f3} + E_4V_{f4} + E_5V_{f5} \tag{3.3}$$

where E_1 to E_5 and V_{f1} to V_{f5} are the Young's moduli and volume fractions of polysilicon base layer, silicon dioxide, gold ground layer, aluminum nitride (AlN) and gold top electrodes respectively. The volume fractions of each layer is the ratio of the volume of that specific layer to that of the total volume of the entire stack. Thus, for the device shown in Figure 3·5. E_l is calculated to be 201.82 GPa. In addition, replacing all the E's with ρ_1 to ρ_5 (which are the respective densities of the stack in similar order as before) in Equation 3.3 yields an estimate for the stack density (ρ), which comes out to be approximately 3718 kg/m3. It may be noted that the Voigt weighted average method imposes the highest limit on the Young?s modulus for a stack of given dimensions and thickness. Hence, the resulting frequency calculated (368 MHz) from it is an overestimate of the actual frequency.

3.4 Experimental Results

The resonator was excited using a Vector Network Analyzer (VNA, Agilent N3383) and a resonance peak at 356.2 MHz was observed. Figure 3·7(a) shows the S21 parameter (in dB) in the range of 353 MHz and 360 MHz. Figure 3·7(b) shows the resonance plot of the S21 (in dB) data in the same frequency range with the device mounted on a stage facing directly towards a source antenna, at a distance of 0.50 m. The device is indeed actuated wirelessly at exactly the same frequency of 356.2 MHz, thus confirming wireless actuation method. Henceforth, similar measurements were carried out for all distances between the source antenna and the piezoelectric device from 0.15 m up to 1.25 m. It may be noted that all wireless actuation measurements are carried out at a fixed source antenna. A Labview program swept the

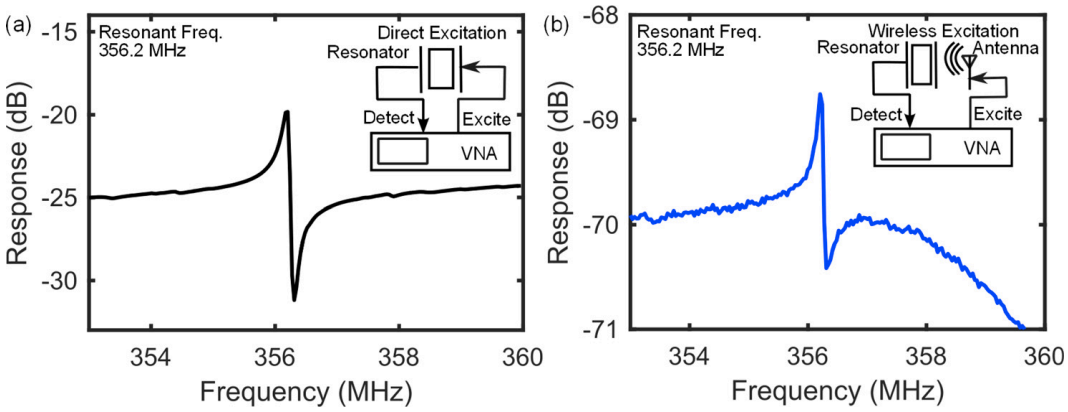

Figure 3·7: (a) Response of the device actuated and measured by direct actuation via the VNA, as depicted by the inset schematic, shows a resonance peak at 356.2 MHz. (b) The response of the device under wireless actuation as depicted by the inset schematic. A similar peak is detected at 356.2 MHz, confirming wireless actuation of the device.

VNA frequency between 353 MHz and 360 MHz and recorded the resulting S21 data for each distance. The S21 parameter represents the ratio of the voltage amplitude at port 2 (response from the resonator device) of the VNA with respect to that at port 1 (excitation to source antenna).

Using a similar method of Chapter 2 the piezoelectric resonator was approximated using an equivalent Butterworth Van Dyke model and the maximum value of the real admittance was extracted and plotted against distance given in terms of the wavelength (λ) (about 0.8 m calculated at the resonance frequency of 356.2 MHz) between the measured 0.15 m and 1.25 m distance range. This distance dependence is presented in Figure 3·8(a). While it is expected that the curve will show a steady decline as the distance of the device increases from the source antenna instead anomalous peaks and troughs are observed, consistent with near-field effects. Although the device actuates wirelessly, this counterintuitive distance dependence is due to the near-field (operation within one wavelength) regime effects where linearly polarized systems are susceptible to reflections and multipath interferences - as described in Chapter 2.

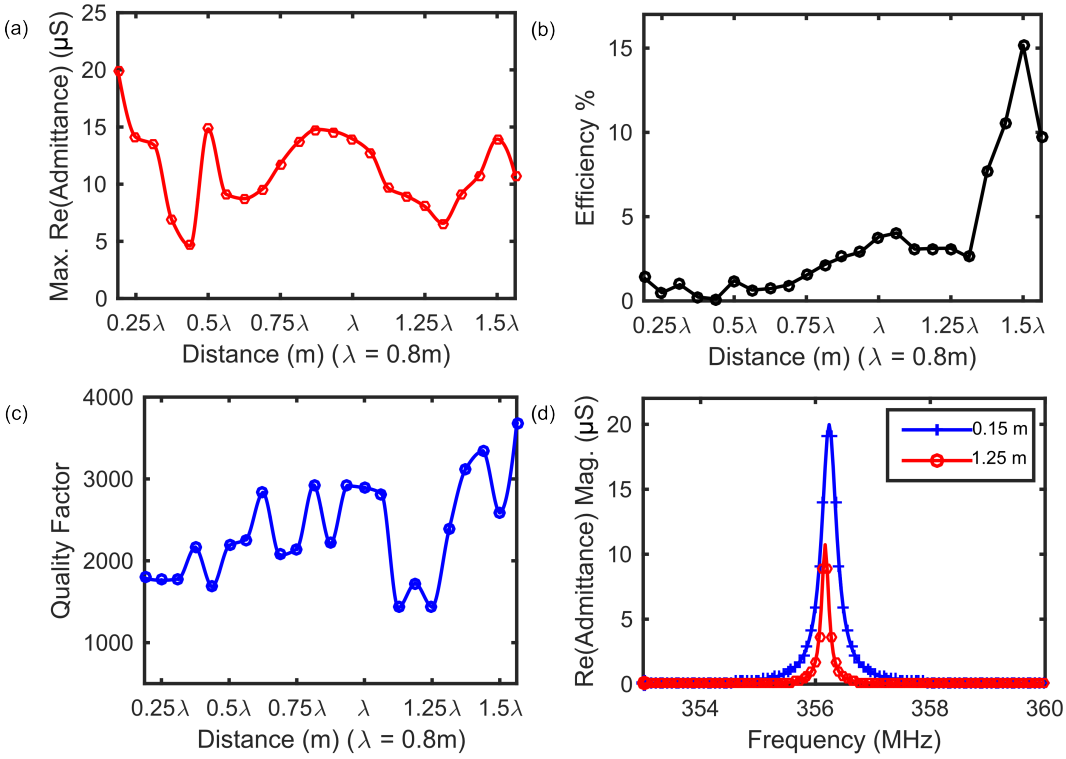

Figure 3·8: (a) The distance dependence of the extracted G_{BVD} is plotted where the distance is given in terms of the wavelength (λ) calculated at the resonance frequency. (b) The distance (given in terms of the wavelength) dependence of the calculated efficiency is plotted. (c) The dependence of the Q to distance (in terms of wavelength) shown. The quality factor varies from between 1400 to about 3600. (d) The superimposed Lorentzian response of the device at distance of 0.15 m and 1.25 m is shown. While the magnitude of the resonance response is higher at 0.15 m, the subsequent quality factor is lower. At 1.25 m, the magnitude is lower and the quality factor is higher, thus resulting in a higher efficiency for the device at 1.25m than at 0.15 m.

The distance (given in terms of the wavelength) dependence of the efficiency is plotted in Figure 3·8(b). The efficiency of the device increases to a maximum of nearly 15 % at a distance of 1.2m from the source antenna. The efficiency of the device is given by the ratio of the incident power to the output power, where the incident power is calculated as the product of the measured power density at each distance by a portable handheld power meter (RF-Explorer 3G) and the effective area of the top IDTs. The output power is calculated from the S21 response of the device measured by the VNA. The efficiency reported here is still low; however, it is significantly larger than the 3 % reported in Chapter 2. The primary reason is believed to be the ratio of device size and wavelength. Increasing this ratio by increasing frequency and at the same time reducing the excitation wavelength can improve the directivity of the device, which can lead to better energy transfer between the incident electric field and the piezoelectric resonator. Typically, the conventional thickness BAW modes have much higher frequencies, which are expected to generate even much higher efficiencies. The quality factors calculated at each distance (given in terms of the wavelength) for the resonator are shown in Figure 3·8(c) and can be seen to be between 1000 and 4000. Figure 3·8(d) shows the superimposed Lorentzian response of the device. It demonstrates that while the magnitude of the resonance is higher at 0.15 m (starting distance of the experiment) the quality factor is lower and at 1.25 m (the last distance measured) the quality factor is higher and the magnitude of the resonance is lower. Thus, the device has a lower efficiency at 0.15 m and a higher efficiency at 1.25 m. It may also be noted that a slight shift in the resonance frequency from 356.2 MHz is also observed as the distance is varied between the source antenna and device.

3.5 Conclusion

To summarize, we demonstrate wireless actuation of S_0 Lamb wave mode in a micro-mechanical resonator with 15% efficiency. This enabling technology of low-power excitation of micro-mechanical devices with small footprint could be fundamentally important to a wide variety of applications in wireless communication and biomedical device engineering.

Chapter 4

Silicon Nanowires

4.1 Introduction

The idea for the very first biosensor was put forward in 1962 by Clark and Lyons from the Children Hospital in Cincinnati [Clark and Lyons, 1962]. There device laid out in a subsequent patent in 1970 used the enzyme glucose oxidase (GOx) embedded between two membranes in contact with an electrode pH sensor to measure the concentration of glucose in solution. This patent was subsequently converted into a commercial device by the Yellow Spring Instrument Company that launched in 1975 the first dedicated glucose analyzer (the Model 23 YSI analyzer) for the direct measurement of glucose in 25 mL samples of whole blood. Since then and aided by CMOS large-scale manufacturing, the world biosensor market has ballooned and is presently expected to reach above 25 Billion USD in the next five years. This includes clinical diagnostics [Kirsch et al., 2013], food safety [Sharma and Mutharasan, 2013], homeland security [Bruckner-Lea, 2004] and environmental monitoring [Nigam and Shukla, 2015].

Point of care (POC) devices for bio-medical applications have been growing in significance partly due to increased life expectancy and corresponding diagnostic needs for common, age-related diseases such as diabetes, heart disease and cancer [Kirsch et al., 2013]. In recent years such POC devices have received much research attention from both academia and industry. The question at the crux of this effort is mostly the same: How many lives could be saved if the presence of a life threatening disease

could be determined by examining a drop of blood in the span of minutes, rather than waiting for lab turn arounds - especially in remote field settings where labs/hospitals are far flung - which in extreme cases could take days. Such POC device biosensors could make a positive analysis based on the presence of a corresponding biomarker in the provided drop of blood or similar body fluid.

4.2 Biosensors

In 1994 Prof. Higson from Manchester University (UK) stated [Higson et al., 1994], that a biosensor was a chemical sensing device in which a biologically derived recognition entity is coupled to a transducer. Biosensors are usually categorized according to the recognition entity as either metabolism sensors, where enzymes chemically convert the analyte or affinity sensors where receptor molecules such as antibodies, aptamers etc. are immobilized on the surface of the detector. These receptors interact with the target molecules with high-affinity. Device sensitivity in such systems is directly based on the antibody-antigen binding affinity [Giljohann and Mirkin, 2009]. This specific interaction is then used by the transduction mechanism to generate an output. The transduction mechanism can either be optical, electrical or mechanical. Common biosensor transducers used today include optics-based devices, such as Enzyme-Linked Immunosorbent Assay (ELISA) and Surface Plasmon Resonance (SPR), and electrochemical techniques and mechanical oscillating devices such as Quartz Crystal Microbalance (QCM) and cantilevers. Within these classifications are further types an exhaustive review of which is outside the scope of this work, however a few of the major types are discussed below.

No matter the sensing or transduction mechanism a biosensor is expected to produce highly reliable, consistent and reproducible results which are based on sensitive and selective measurements of the target analyte being detected. Here sensitivity

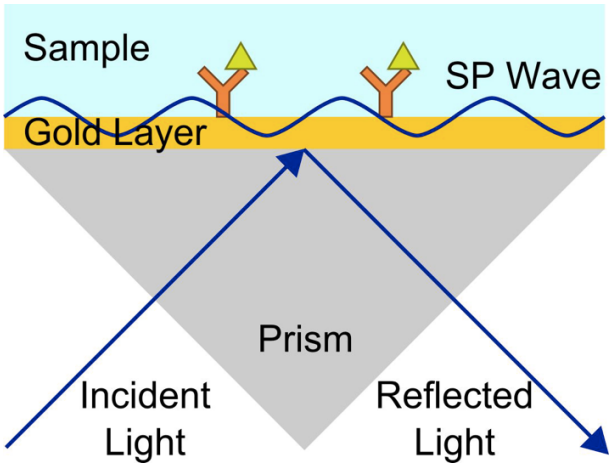

Figure 4·1: Schematic showing the Surface Plasmon Resonance scheme.

is the smallest discernible concentration of the analyte which the sensor can detect above the background noise. While selectivity is the ability of the sensor to detect selectively only recognize the target analyte only in the presence of a myriad of other molecules - such as are present in most physiologically relevant fluids like whole blood or serum.

The Surface Plasmon Resonance (SPR) based biosensor, mentioned above, has long been considered the gold-standard in biosensing mechanisms. It is based on the detection of refractive index changes in a solution in proximity to the surface of a metal plane (typically gold). As shown in Figure 4·1 approrpriate receptor molecules are immobalized on the surface of the gold layer, which is exposed to the sample fluid. As the target analyte selectively binds onto these receptors a change in refractive index is observed due to the coherent electron oscillation, or surface plasmons, at the liquid metal interface are excited by the light polarized parallel to the place of incidence. A prism is used to ensure light has similar momentum as the surface plasmons which results in resonant excitation.

Due to energy transfer from the incident light to surface plasmons, the reaction

intensity shows a minimum at resonance frequency. A shift of this resonance frequency can be directly related to the number of bound molecules. These devices have been developed since 1983 [Liedberg et al., 1983] and are commercially available by various manufacturers like Biocore, Riechert Technologis and GWC Technologies. While having high sensitivity of antigen detection - reported in literature down to pico-molar concentrations [Guo, 2012,Homola, 2008] these sensors suffer from non-specific binding and owing to their construction are too bulky to be of any practical use to POC applications. In addition they are not field hardy and require considerable optical and mechanical maintenance. However at present work is being done on compatible handheld models using this platform.

Compared to optical type of sensors such as the SPR, electrochemical biosensors do not require extensive setup complexity or cost. These types of sensors are further sub-classified as either conductometric, potentiometric or amperometric sensors. As the name suggests conductometric sensors measure the change of conductance due to a binding event between receptor and target (analyte) molecules. Potentiometric sensors monitor the electric potential on a working electrode with respect to a reference electrode and amperometric sensors measure the change in current on the working electrode. Of these amperometric sensors have been shown to be the most sensitive [Mehrvar and Abdi, 2004] and exhibit a linear dependence between the current and analyte concentration. They have been shown to detect a wide variety of biomarker such as the prostrate cancer marker [Akter et al., 2012], the cardiac risk marker C-Reactive Protein (CRP) [Gupta et al., 2014] and metastatic liver cancer marker [Zhao et al., 2013].

While electrochemical based biosensors have been known to have the strongest responses however they still have considerable room for improvement. For instance the presence of differing pH, ionic strength and other molecules in the fluid being

tested - have been shown to cause problems for these type of sensors.

Similar to SPR, mechanical biosensors offer label-free and real time biomarker detection. They are based on shifts in resonance frequency which is caused by the selective binding of the target analyte to the receptor molecules immobilized over the mechanical resonant structure, such as cantilevers, beams or membranes. Amongst the first demonstration of label free biosensing via cantilevers was performed by [Fritz et al., 2000] in 2000 who detected DNA hybridization. Since then they have been used to detect numerous cancer biomarkers, heart disease biomarkers and others [Arntz et al., 2002]. Many expert reviews of this technology have been written and readers are encouraged to go through the same for more information [Goeders et al., 2008, Boisen et al., 2011].

Reducing the dimensions of the resonator increases its mass-resolution hence measurements of analytes down to yoctograms have been reported in literature [Chaste et al., 2012]. While the sensitivity of these devices is remarkable, the optical (laser) based detection system makes them, like the SPR devices described above, unfeasible for POC applications.

4.3 Transistors: Basics

We shall take a slight break in our discussion of Silicon Nanowire based biosensors with a brief detour of the common MOSFET transistor. The transistor (transfer resistor) is a semiconductor device used to switch or amplify electrical signals as they are transferred through it from input to output terminals. Transistors are ubiquitous to modern electronics since there first presentation by the team around W. Shockley at Bell Labs (Nobel Prize in Physics 1956). There are two types of transistors: bipolar (resistance controlled by current) and field-effect (resistance controlled by voltage) transistors. Compared to the former the later consume lower power and hence are

preferred. Metal Oxide Field Effect Transistors (MOSFETs) as they are called will be explained briefly here, while the reader is referred to standard literature for a more detailed description [Sze and Ng, 2007].

Figure 4·2 (a) shows a typical n-channel MOSFET. The metal gate above the semiconductor channel is isolated by a metal oxide - known as the gate oxide. The application of a positive voltage across this oxide layer is what causes the accumulation of negatively charged carriers in the semiconductor layer below, creating an inversion layer. At this point an application of a voltage between source and drain will cause current to flow between the two terminals. The transistor can be operated as shown in Figure 4·2 (b) in either saturation or linear regions. In the linear region the inversion layer (n-doped regions) connects the source and drain like a simple resistor. And the source-drain current I_{SD} is given by Equation 4.1. Where Q is the charge density in the channel, C_{OX} is the capacitance of the gate oxide layer per area, W is the width of the channel, L is the channel length, V_g is the gate voltage, V_{th} is the threshold voltage and V_{sd} is the source-drain voltage. While this linear model is only valid in the small source-drain voltage region where V_{sd} is lesser than the difference between gate voltage and the threshold voltage, the source-drain current becomes zero if the gate voltage is below the threshold voltage.

$$I_{SD} = \mu C_{OX} \frac{W}{L} Q V_{SD} = \mu C_{OX} \frac{W}{L} \left(V_g - V_{th}\right) V sd \tag{4.1}$$

The saturation region occurs at higher V_{sd}, where a higher voltage narrows the inversion channel close to the drain. Above the saturation voltage (V_{sat}) the channel is "pinched-off" at the drain, and the electrons under the influence of the source-drain voltage are forced to propagate through the substrate. The current at this point is nearly independent of the V_{sd}.

To switch on the MOSFET a sufficiently large inversion channel is required which

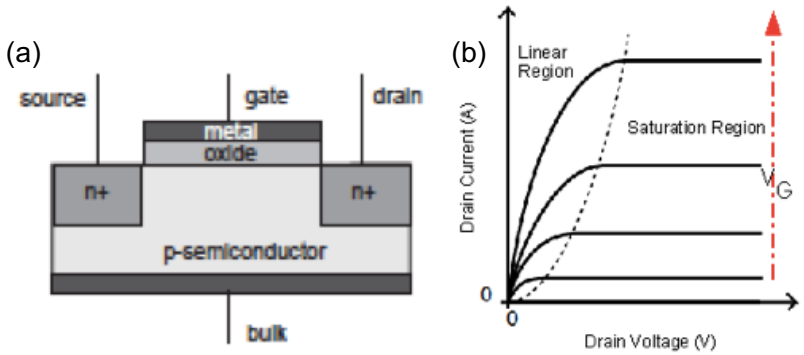

Figure 4·2: (a) Schematic of a typical n-channel MOSFET. The p-type semiconductor substrate contains two highly n-doped regions (source and drain). (b) Typical drain current vs. drain voltage for several gate voltages Vg. Dashed curve indicates the transition between linear and saturation mode.

is established above the V_{th}. It is assumed in our present discussion that the source-drain current is zero for gate voltages below the threshold voltage. However a more minute inspection reveals that a very small current can flow between the source and drain due to thermal fluctuations of charge carriers, below the threshold voltage, as described by Boltzman statistics. This sub-threshold current is exponentially dependent on the gate voltage and given by,

$$I_{sd} \propto exp\left(\frac{e}{kT}\cdot\frac{V_g}{1+C_D/C_{ox}}\right) \tag{4.2}$$

with the depletion capacitance C_D, the gate oxide capacitance C_{ox}, the Boltzmann constant k, the elementary charge e and the absolute temperature T. The threshold voltage for a MOSFET V_{th} is defined as,

$$V_{th} = \varphi_{ms} - \frac{Q_{ox}+Q_{ss}+Q_D}{C_{ox}} + 2\varphi_B \tag{4.3}$$

where the first term is the work function different between the metal gate and the semiconductor, the second is the sum of charges in the oxide Q_{ox}, at the oxide-

semiconductor interface Q_{ss} and the silicon depletion charge Q_D. In the third term, twice the bulk potential occurs to reach the onset of inversion. Details of these and other characteristics can be found in traditional texts [Sze and Ng, 2007]. For this thesis it is the sub-threshold current, defined within a sub-threshold region of the MOSFET transistor that we shall remain interested in. This region of operation is characterized by low self noise, low heating and makes the transistor exceptionally susceptible to the gate voltage, which is essential for employing them as biosensors as will be seen in the next section.

4.4 Nanowire based biosensors

Silicon Nanowire based biosensors have considerable advantages above the sensors described in the previous sections mainly in the essential areas of real-time, label-free sensing using CMOS compatible electronics. These devices can be adapted to multiplexed detection of various antigens on the same chip and have also shown the potential of implantation. Smart design of these sensors have shown measurements independent of temperature, pH and ionic strength.

Based on the field effect employed in metal oxide semiconductor field effect transistors (MOSFETs - discussed in section 4.3) Nanowire based biosensors were pioneered by Prof. Piet Bergveld of the University of Twente (Netherlands) in the 1970's. He named them Ion-sensitive field effect transistors or ISFETs. [Bergveld, 1970]. As shown in Figure 4·3, ISFETs differ from MOSFETs in the manner both devices are gated. In the later a metal electrode is employed while in the former the surface ions above the dielectric oxide layer gate the device below. In addition ISFETs are also called dual-gate-FETs - in the sense that while there exists the ions in the fluid in contact with the gate oxide (dielectric) there is also a back gate being applied to the device which can serve to expand the conduction channel. Since the common mate-

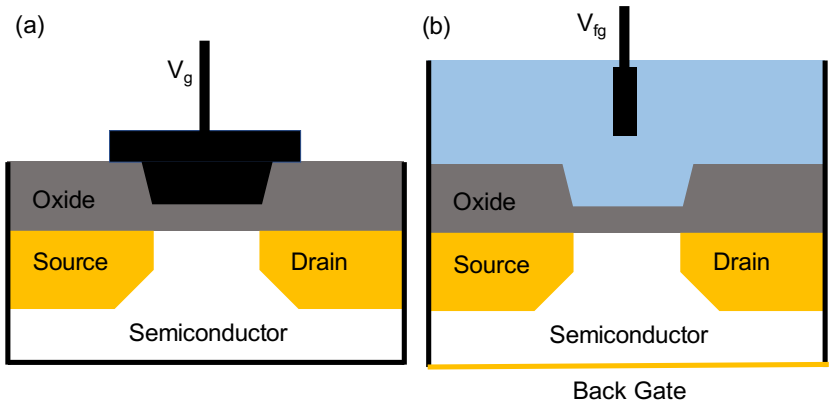

Figure 4·3: (a) Schematic of a typical MOSFET device which includes a source, a drain, a gate electrode which is used to apply potential V_g and a semiconductor conductance channel. (b) Schematic of a ISFET device, the analyte solution is gated by a reference electrode which is used to apply potential V_{fg} - fluid gate voltage. It also has a metaled back-gate which can be used to apply a potential V_{bg}.

rial used for the oxide of the ISFET was Silicon Oxide which would express silanol surface groups which may either be protonized or deprotonized based on the pH of the solution, hence ISFETs have found use as pH sensors [Bergveld, 2003]. A change in pH would thus lead to an appropriate increase or decrease in conductance of the semiconducting channel below (nanowire).

The cross section of the nanowires (semiconducting channel) offers an advantage wherein surface charges will gate the whole cross section of the semiconducting channel, hence traducing a surface effect into measurable changes in bulk properties. The property in question is often the conductance (I/V) of the ISFET. This is to say that the presence of an antigen can be detected in minute quantities in the fluid by the nanowires if it can be brought closer to the same, with enough selectivity over other molecules in the same fluid environment. There in lies the essence of the Silicon Nanowire based ISFET sensor. The method by which an antigen of interest can be attracted over other molecules present in the fluid is to have receptor molecules such as appropriate (and highly selective) antibodies immobilized over the surface which

would then attract and bind on to the analytes of interest. This binding would cause a global change in the field across the dielectric oxide layer causing a change in the conductance of the sensor, which can then be read-out via electronic data analysis systems. It has been shown repeatedly that the sub-threshold regime is the most sensitive for the detection of target antigens [Gao et al., 2009]. Since the gate oxide surface remains in contact with the liquid surface, hence the ISFET is said to have a fluid gate (gate electrode in traditional MOSFET).

There are many research groups who are busy employing Silicon Nanowire based ISFETs for the detection of various biomarkers. Some of them include the Lieber group at Harvard [Cui et al., 2001], the Reed group at Yale [Stern et al., 2007], the Bashir group at the University of Illinois at Urbana-Champaign [Duarte-Guevara et al., 2014], the Heath group at Caltech [Bunimovich et al., 2006] and the Schonenberger group at Besel University [Knopfmacher et al., 2010]. Each of these groups has made headway in detection of biomarkers at various quantities based on different fabrication techniques of the ISEFTs and in mostly buffer solutions.

4.5 Silicon Nanowire biosensor - fabrication

Silicon Nanowires owe there sensitivity to the higher surface area to volume ratio, hence there dimensions of fabrication is important. Many biological molecules of interest are in the range of micro to nano meter ranges. The rough dimensions of most proteins are about 8-10 nm, diameter of DNA helix is around 2 nm, the length of DNA with 100 base pairs is around 34 nm, the thickness of bacterial flagellum is 20 nm, most viruses range in size from 20 to about 400 nm, most bacterium are even larger at about 1 to 10 microns and the diameter of the human red blood cells is about 6 - 8 microns. Thus a biosensor device having sub micron or nano-dimensions has the best efficiency of detecting such molecules.

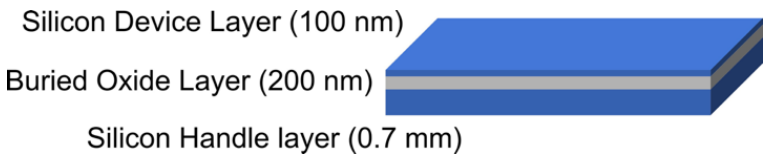

Figure 4·4: Typical SOI wafer with the silicon device layer followed by buried oxide and the thick silicon base handle layer.

The silicon nanowire biosensors are fabricated in a top-down fashion. In contrast such devices can be fabricated in a bottom-up process as had been done by the Lieber group. While it produced high quality nanowires the vapor-liquid-solid growth method did not yield consistent and reproducible devices, hence at present the preferred method of fabrication is the top-down.

The silicon nanowire based biosensors that we have fabricated are based on Silicon-on-oxide (SOI) wafers consisting of a top 100 nm silicon device layer followed by a 200 nm layer of buried oxide, which is followed by a 700-microns of lightly boron-doped Silicon handle layer. The 6" wafers are cut into rectangular pieces of 2 by 3 centimeters. We fabricate 16 nanowire biosensor devices on each of these rectangular pieces.

1. Before the actual fabrication the rectangular piece of SOI wafer as shown in Figure 4·4 is cleaned using acetone and iso propanol followed by a 1:3 mixture of Hydrogen per oxide and Sulphuric acid at 80-degrees for 30 minutes. The piranha solution is very aggressive and quiet exothermic hence only quantity of solution required is made and handled with appropriate protective measures.

   Piranha treatment (cleaning) of the SOI wafer should hydrolyze the surface and make it more hydrophilic hence the surface at the end of the process should wet immediately without the formation of any islands of silicon within the film of water.

2. The cleaned and dry wafer piece is then ready for the photolithography process.

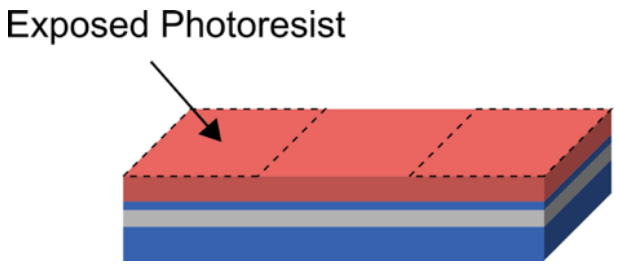

Figure 4·5: Cleaned wafer spun with HMDS and Photoresist is exposed to pattern the source-drain electrodes.

This recipe has been enhanced to care for the effects of humidity when weather control inside the lithography room isn't optimized. The wafer is heated on a hot plate at 115-degrees for 10 to 15 mins. A primer (Hexamethyldisilazane) HMDS and Photoresist S1813 (Microposit) are spun one after the other using a spinner (Headway Research PWM32-CB-15) for 45 seconds at 4000 RPM.

The photoresist (PR) is then baked at 115-degrees again for 10 mins. Once the wafer piece has cooled down it is then stuck onto a 4-inch carrier wafer using double sided tape (3M) and inserted in the MA6 Mask Aligner from Karl Suss with a 350W mercury short arc lamp for 12 seconds at 10mW/cm^3, using Hard contact setting and a contact distance of 50-microns. Following the exposure the wafer piece is immersed in Toluene to harden the top layer of the PR, for about a minute. The piece is then washed and dried with DI water and Nitrogen respectively. The wafer is then post-baked at 115-degrees for 2 minutes and following that is immersed immediately into MF-319 (Microposit) developer. The container is gently shaken to allow the developer to develop the PR for 45 seconds. The wafer is then washed and dried again and observed under the lithography room microscope with a yellow filter.

Once this step has been completed and the pattern looks good the wafer piece is cleaned in the M4L (PVA, Tepla Inc.) plasma asher using an oxygen plasma of 300 sccm at 300 Watts for 5 minutes. This will ensure that any left over

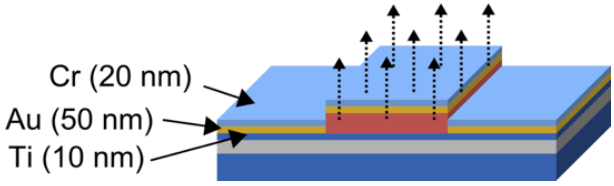

Figure 4·6: Metal deposition followed by the Acetone lift off process which will remove metal layers on top of the unexposed PR.

primer layer (HMDS) and PR residue is removed from the wafer.

3. The plasma asher process from the previous step will ensure better adhesion of the metal layer of this step. It may also be noted that once the wafer is plasma cleaned it should immediately be exposed to the physical vapor deposition (PVD) process for metal deposition. What has been found to work is to setup the PVD - thermal evaporator (Edwards Auto 306 Turbo) before the wafer is cleaned and immediately exposed to the process.

   From bottom to top 10 nm of Titanium is deposited first as an adhesion layer followed by 100 nm of Gold electrode layer and 25 nm of Chromium - which will act as an etch mask later on.

   The final chrome layer completely covers the wafer surface once its removed from the thermal evaporator. The wafer has a mirror like appearance at this stage. This wafer is then introduced into an acetone bath and sonicated for 4-5 minutes. This step often known as lift-off will lift-off the unexposed PR layer and the metal layers on top of it as shown by the schematic of Figure 4·6. At this point sonication beyond 5 minutes could be carried out till the electrodes are sharp and all excess metal and unexposed PR residue is not observed any more. The excessive sonication will not have any effect on the deposited metal if the plasma cleaning from the last step was carried out well. Deposited metal leaving from the exposed pattern will render that particular device on the wafer

useless.

4. Poly-Methyl Methacrylate (PMMA) is now spun onto the wafer to define the nanowires. Two coats of PMMA: PMMA - 495 and 950 (both from Microposit) - are spun one after the other, respectively, at 1700 RPM for 45 seconds. Each layer is baked at 110-degrees for 10 minutes. Scanning Electron Microscope (JEOL 6400) equipped with a beam blanker (Deben) and lithography software (NPGS) is used to write the wires. A CAD-drawing of the dimensions of the pads and the nanowires needs to be drawn in the NPGS software. The dimensions of each of the pads is about 10 by 50 microns. They are 3 microns apart hence the nanowires that straddle them need to be at least 10 microns in length to allow sufficient overlap and connection. In addition we expect each of the wires to be 50-60 nm thick. Electron dosage governs the exposure and the eventual thickness of the nanowires along with the magnification at time of writing.

   The abeam-lithography process as it is called can be understood with the analogy of a common pencil. The sharper the point of the pencil the thinner the text is going to turn out. Hence the higher the magnification the sharper the beam of electrons that is used by the equipment and hence the thinner the feature size. However with higher magnification the field of view also reduces thus the beam is able to see a smaller area. Thus nanowires drawn at a higher magnification could be thinner but the limit of magnification which would allow the drawn nanowires to completely straddle the 5 micron gap of the electrode pads was about 3200x. At this magnification electron dosage of 550 nC/cm_2 was used for the pads and 525 nC/cm_2 was used for the nanowire writing at 40 keV. The wafer piece was then developed in a 1:4 mixture of cold Methyl Isobutyl Keton (MIBK) and iso propanol for 11 seconds. The developed nanowires can then

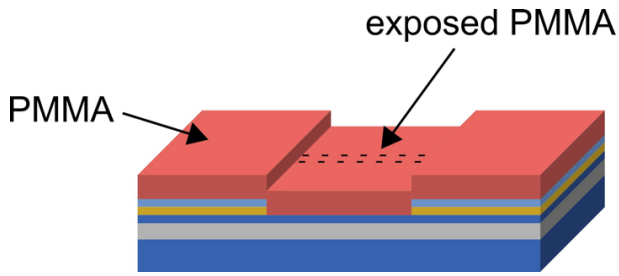

Figure 4·7: PMMA layer exposed to form the pads and the nanowire structures.

be observed under an optical microscope. No attempt however should be made to measure the wires under the SEM - the electron beam could develop the PMMA and destroy the nanowire structures. Nanowire structures can only be measured after chromium mask has been deposited on top of them as described in the next step. However if the wires do not come out to be the right thickness the entire wafer piece at this point will become useless. In order to gain a better understanding multiple dosage tests were carried out using a test wafer piece, before the above mentioned dosage rates were settled upon.

5. The wafer piece is now plasma cleaned again with a similar recipe of 300 W, 300 sccm as before however it is only run for 2 minutes this time. This is since the plasma asher cleans organics it may eat away at the nanowire structures that have been written. A 25 nm layer of Chromium is then deposited as before using the thermal evaporator and lifted off using Acetone in a sonicator. The sonication process should be run for about 4 to 5 minutes or as long as is needed till the nanowires look sharp and clean under an optical microscope.

6. Since there is now a chromium mask on top of the devices the silicon can be etched away to realize the nanowire devices. The 100 nm device silicon layer is etched using the Reactive Ion etching process with a plasma mixture of Oxygen (5 sccm) and Tetrafluoromethane (50 sccm) at 120 Watts for 2 minutes and

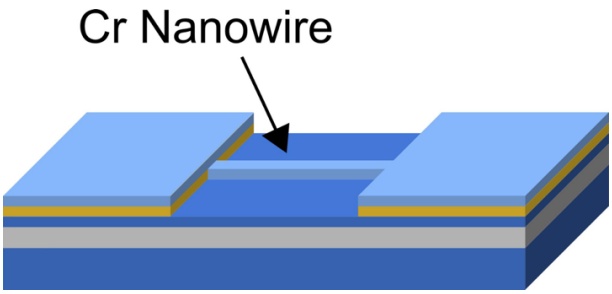

Figure 4·8: Chromium layer deposition on wafer and nanowires.

75 mTorrs. This recipe has shown to etch away the 100 nm of Silicon. The end point reveals an olive green colored wafer which is the color of 200 nm of silicon oxide. If after this process the wafer still looks a bit pinkish or bluish the recipe should be repeated for about 30 seconds. It has also been observed that the cleanliness of the RIE chamber before the beginning of the process and also running the process without the wafer piece both enhance the quality of the devices.

7. Now the chromium layer which has served its masking purpose is removed via the Chromium Etchant (Microposit) and silicon nanowires connected to gold source-drain electrodes are obtained. Figure 4·9 shows this as a schematic and the electronic micrograph of one such set of nanowires. The nanowires are about 60 nm (+/- 1 nm) wide and straddle the gold electrodes on either side. The electrodes are symmetric and either one can be used as the source or drain.

8. The gate oxide is now put down using the Atomic Layer Deposition (ALD) system. About 5 nm of Aluminium Oxide is put down on the entire wafer piece using the ALD (Savannah 100, CambridgeNanotech). The ALD ensures that a continuous layer of the oxide is put down which will conform to the shape of the devices. In contrast E-beam evaporation of oxide layers should be avoided since the deposition system is random and leaves behind microscopic pin holes.

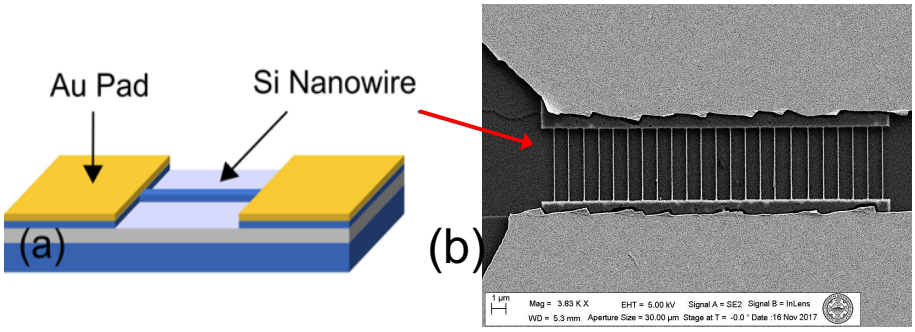

Figure 4·9: (a) The chromium layer removed reveals the gold source-drain electrodes and the silicon nanowires that straddle them. (b) Electron Micrograph of 60 nm (+/- 1 nm) wide silicon nanowires.

Such pin holes would lead to leakage currents in the device and render them useless.

9. We then use an SU-8 insulation layer to cover the source-drain electrodes around the vicinity of the nanowires to ensure that when the device is used only the nanowire structures (covered with 5 nm of gate oxide) are open to interaction with the fluid. The SU-8 (MicroChem) is spun on to the wafer piece at 4000 RPM for 70 secs. Then it is soft baked at 65-degrees for 1 minute, 95-degrees for 2 minutes and then 65-degrees for 1 minute. This allows the trapped moisture to leave the layer and makes a more smoother and flat layer of SU-8. The wafer piece is then exposed for 6.5 seconds at 10 mW/cm^2. The wafer piece is then post baked similarly at 65-degrees for 1 minute, 95-degrees for 2 minutes and then again at 65-degrees for 1 minute. The wafer is then developed in SU-8 developer for 2 mins whilst shaking and washed with Iso propanol. Remember that the developed layer must not be washed with DI-water. In case the windows above the nanowires haven't completely opened the wafer can be developed in 30 second increments till completely done. Also extra care must be taken with this step as the windows being opened over the nanowires are only 5 microns wide and need to be aligned perfectly. SU-8 is also particularly nasty to remove hence

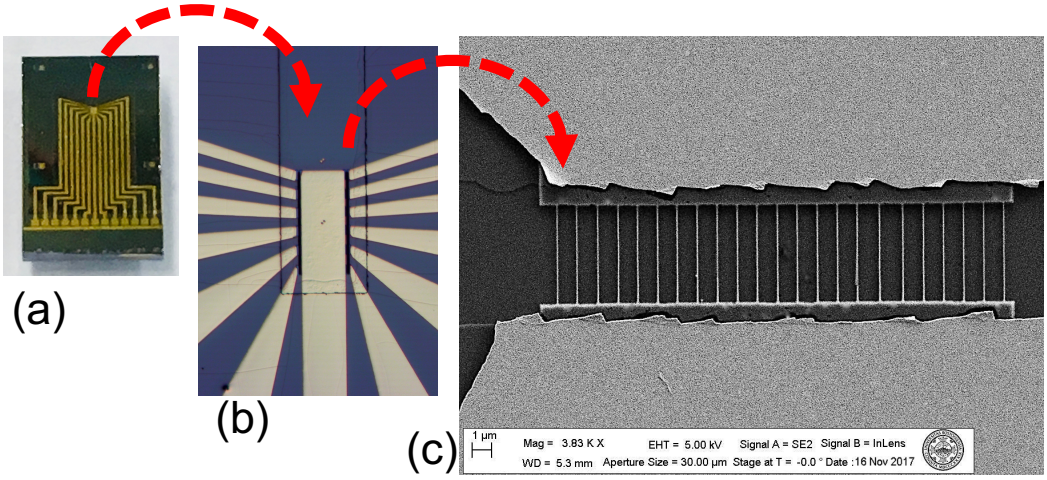

Figure 4·10: (a) Optical picture of the diced device. Golden colored electrodes can be seen. At the base these electrodes can be wirebonded to a PCB board while they each serve as source and drains for the 12 sets of nanowires fabricated on the device. (b) Optical picture of the tip (notch of the M-shape in (a)) of the device in zoomed view to show the central common drain and twelve source electrodes. (c) Electron Micrograph of 60 nm (+/- 1 nm) wide silicon nanowires sets contained between each of the twelve sources and one central common drain of the device.

this step done wrong will mostly likely result in one or many devices or even the entire wafer piece in becoming unusable - since even a minor misalignment may cause the pads to which the nanowires are connected to become exposed rendering the functionality of the wires void. Figure 4·10 (a) shows the picture of the actual diced device. The twelve gold electrodes serve as source electrodes to the nearly twelve sets of nanowires fabricated on the device and connected to one central drain electrode. Figure 4·10 (b) shows the zoomed up tip of the device here while the nanowires can still not been seen however the twelve M-Shaped source electrodes can be seen converging on either side of a central drain electrode. Finally Figure 4·10 (c) shows the electron micrograph of the nanowires containing within each of those spaces between source and common-drain electrode. Altogether each device has 12 nanowires sets. This is to increase the likelihood of detection of the antigen. Multiple wire sets can be used to verify the results observed.

10. The insulated wafer is then coated with PMMA 950 by spinning it at 1700 RPM for 45 seconds and then baking it for 10 minutes at 100 degrees. This will act as a protective cover for the devices during the dicing process. The dicing is carried out with Keteca Dimablades in the Dicer (Disco Dad 3220).

The devices are now ready for funtionalization which will be described in the next section.

4.6 Silicon Nanowire biosensor - funtionalization

This section will present the detailed recipe for funtionalization and salinization of the devices for use with antigen detection. First Silanization is carried out to put down a layer of amines which could then bind out to the antibodies via zero-length functional groups.

1. The device is sonicated in Acetone bath for about 30 seconds to remove the deposited PMMA protective layer, put down during the dicing process. The device is washed with Acetone, Iso propanol and DI Water and dried with Nitrogen.

2. Immobilization of the antibodies is carried out via the salinization step. APTES ((3-aminopropyl)triethoxysilane) is used for this step which is a well known and understood reagent. 50 l of APTES are hydrated in 1 ml of Ethanol/Water solution 95% to 5% v/v. The solution should be at a pH of 5. The APTES solution should be hydrolyzed in the ethanol/water mixture for 20 minutes at least. In this time the device should be plasma cleaned in oxygen plasma for 2 mins (300 Watts, 300 sccm). The plasma asher adds hydroxyl groups to the surface of the oxide atop the nanowires. The device is then added to the same vial containing the hydrolyzed APTES for another 20 mins. At the end the device must be taken out and washed with the Ethanol/Water solution - twice and once with Sodium Hydro-oxide solution 0.1mM before being dried and stored over night in an oven at 100-degrees. The APTES will bind on to the hydroxyl groups to form a layer on top of the oxide as shown in Figure 4·11.

   A few parameters to note here are that APTES reacts and deteriorates under contact with moisture. Hence either Nitrogen should be bubbled through it before extraction from the bottle or it should be extracted using a syringe. The APTES bottle comes in a seal tight bottle however the rubber seal should not be removed completely, instead a syringe should be used to extract the APTES for use. A glove bag under nitrogen blanket could also be used for this purpose. APTES should also be discarded every six months as despite the afore mentioned precautions it will go bad.

   In addition the device can be stored in the oven after salinization overnight

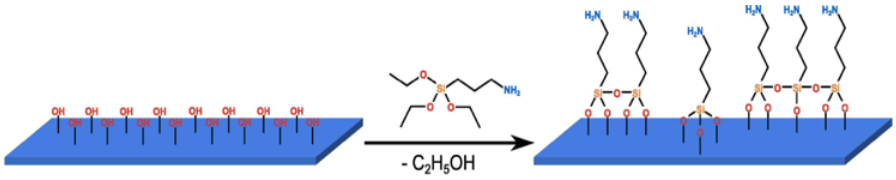

Figure 4·11: The APTES scheme shows the self-assembled monolayer of amines on top of the oxide layer. APTES binds to the hydroxyl groups on the surface which have been added as a result of the plasma asher process.

however it should at least be heated for 3 hours, no less.

3. The device is now ready for funtionalization with the antibody. One aliquot of the antibody anti-ProBNP (8NT2, HYTEST) should be removed from the freezer and allowed to thaw on the bench. The antibodies have previously been aliquoted in 20 μl aliquots each and stored in the freezer.

4. Sulfo-NHS (N-hydroxysuccinimide) is stored in the fridge at 4-degrees while EDC (1-ethyl-3-(3- dimethylaminopropyl)carbodiimide) is stored in the freezer at -20-degrees. These two are the most widely used cross linkers for antibody functionalization on in-organic layers. EDC reacts with carboxyl groups to create an active-ester intermediate, which then reacts with amine groups to form an amide bond. The intermediate is, however, labile in aqueous solutions, and should not be stored but rather used immediately. By adding sulfo-NHS, the solubility and stability of the intermediate is enhanced. The sulfo-NHS replaces EDC to form a sulfo-NHS ester, which is also more active at reacting with amine-containing molecules. NHS and EDS are prepared by measuring 4.4-4.8 mg of the former and adding 1.8 μl of the later to 1 ml of the MES buffer in two separate eppendorf tubes. The schematic of the reaction is shown in Figure 4·12.

5. Immediately 22 μl of each of these solutions is added to the vial containing 20

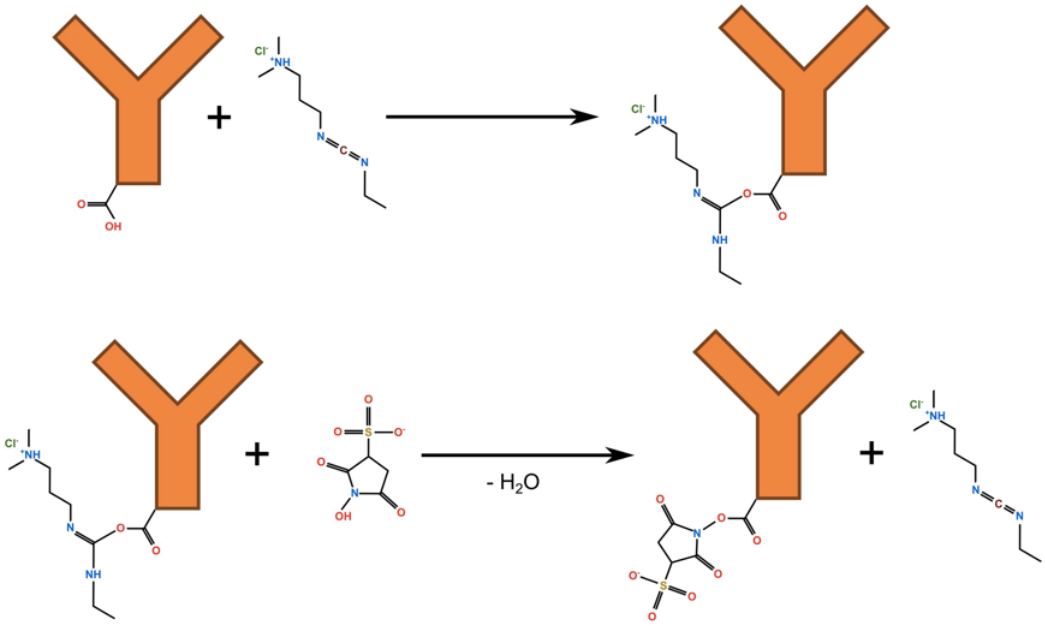

Figure 4·12: Schematic for NHS EDC reaction

μl of the antibody which has by this time come up to room temperature. The resulting mixture is mixed using a pipette and allowed to react for 20 minutes on the bench top. The light in the room may be switched off as a precaution while the reaction takes place.

6. The device is wire bonded onto a PCB with SMA-connectors. The wedge bonder is used for this application rather than the ball bonder since any excessive bonding force might result in the rupture of the thin oxide underneath the device layer rendering the device unusable.

7. At the end of the twenty minutes period 100 μl of PBS pH 8.5 are added to the antibody mixture and mixed. Immediately the drop of this mixture is carefully dropped to the tip of the device while ensuring that the liquid does not touch the wire - bonds. The device (on the PCB) is then enclosed in a plastic petri dish. A wet piece of clean room cloth is added underneath the PCB inside the petri

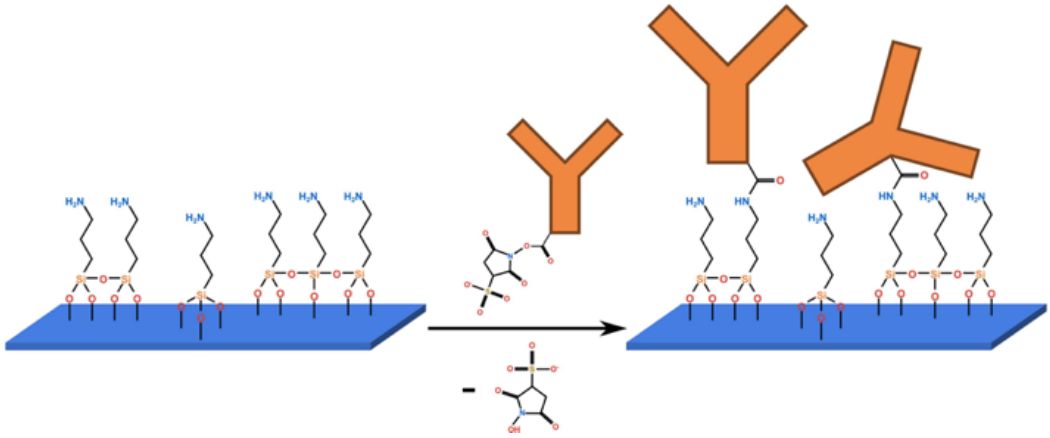

Figure 4·13: Scheme of the zero length cross-linking. The surface amine groups attack the carbonyl group of the sulfo-NHS ester and form a stable amid bond as the sulfo-NHS group leaves.

dish to provide a moisture reservoir and to ensure that the drop of antibody at the tip of the device doesn't dry out. The sulfo-NHS ester will react with amine-covered sensor surface, and form a stable amid bond. The sulfo-NHS group leaves during the reaction resulting in a zero length cross-linking (Figure 4·13).

The device is taken out after 3 hours from the petri-dish and its tip washed with PBS buffer pH 7, three times. At this point the wire bonded device is ready for use.

4.7 Measurements Setup

The wire-bonded and functionalized device is now ready for the experimental setup which comprises of adding a fluid chamber and sealing it in. The fluid chamber used is made out of two parts of acrylic sheet brought together using two metal screws and sealed with the device using para-film. The para-film - seal is created by hand and inserted between the fluid chamber and the wire-bonded device. The fluid chamber has an inlet and an outlet for the fluid to flow along with a port for the reference

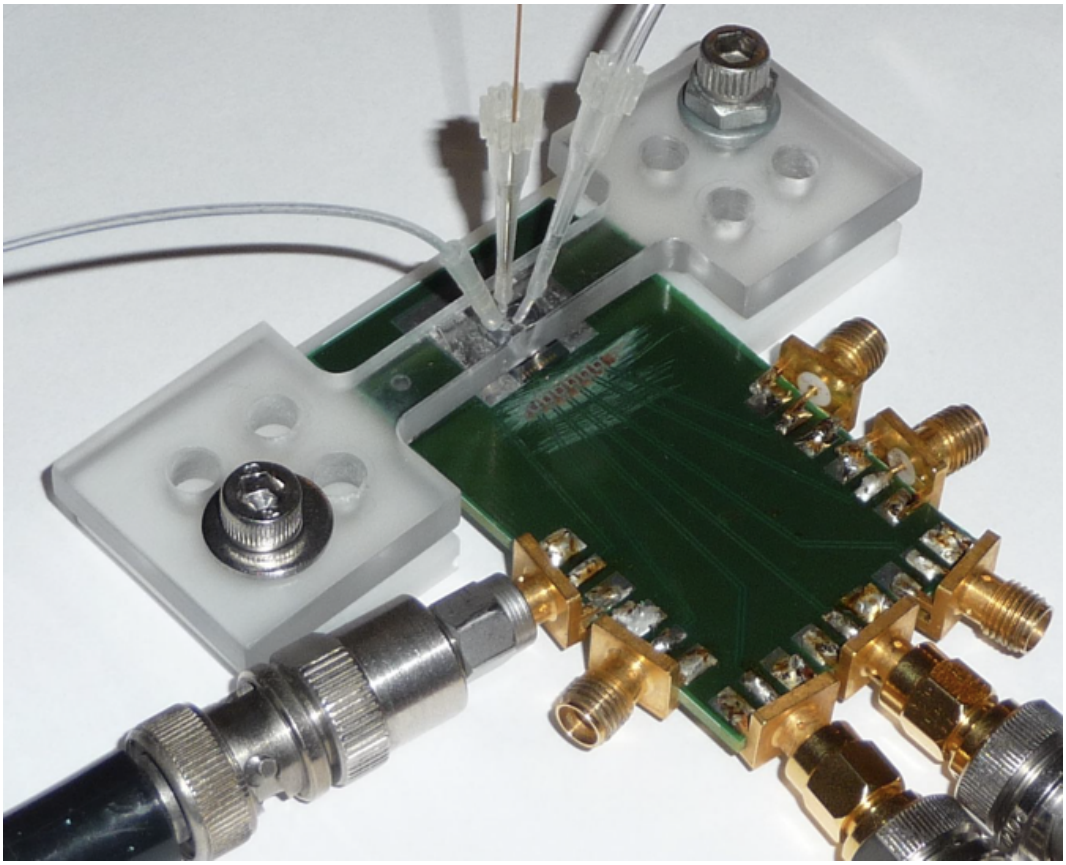

Figure 4·14: The wire-bonded device is shown inside of the fluid chamber. SMA connectors are attached to the various electronic equipments.

electrode.

Figures 4·14 and 4·15 show two views of the fluid chamber with the silicon nanowire device inside. The chamber is secured via two metal screws and a hand rolled parafilm seal. The inlet and outlet ports of the chamber are also marked and the port for the Ag/AgCl reference electrode is also shown.

Typically 50 μl of different concentrations of the antigen separated by 30 μl of wash cycle of PBS (pH 7) - in a so called dilution series - are flown through the inlet and collected at the outlet of the device through the affixed fluid chamber at a constant rate of 400 nl/sec via a syringe pump. Each dilution series contains about 6 - 9 such concentrations all separated by wash cycles. Figure 4·16 shows the circuit

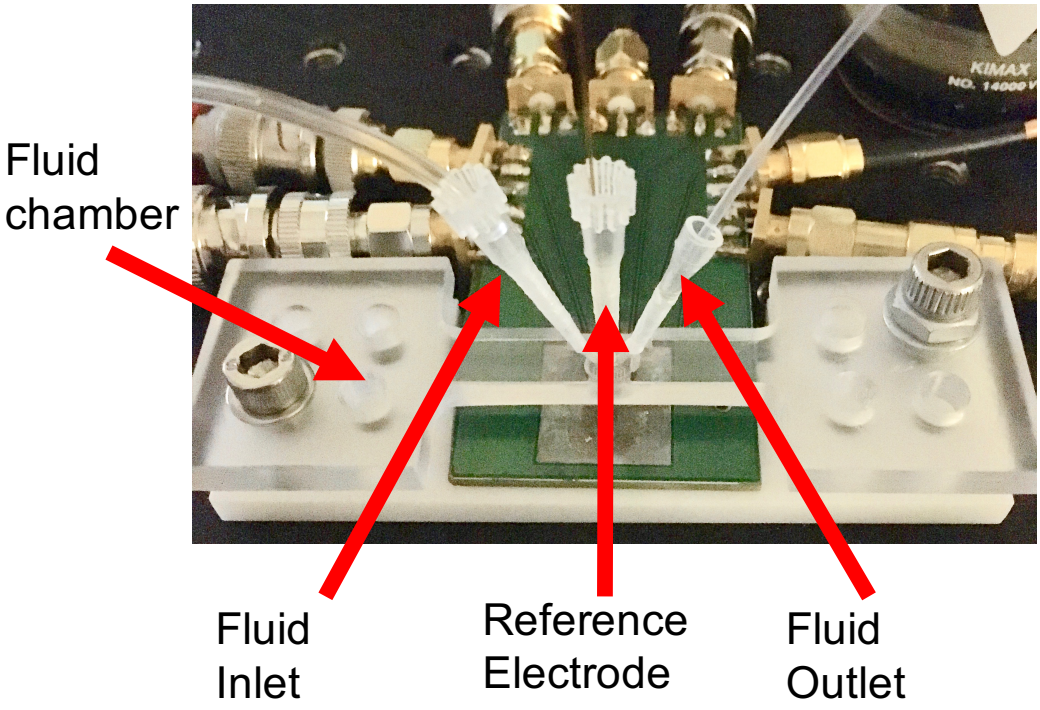

Figure 4·15: Another view of the fluid chamber with the inlet, outlet and reference electrode ports marked.

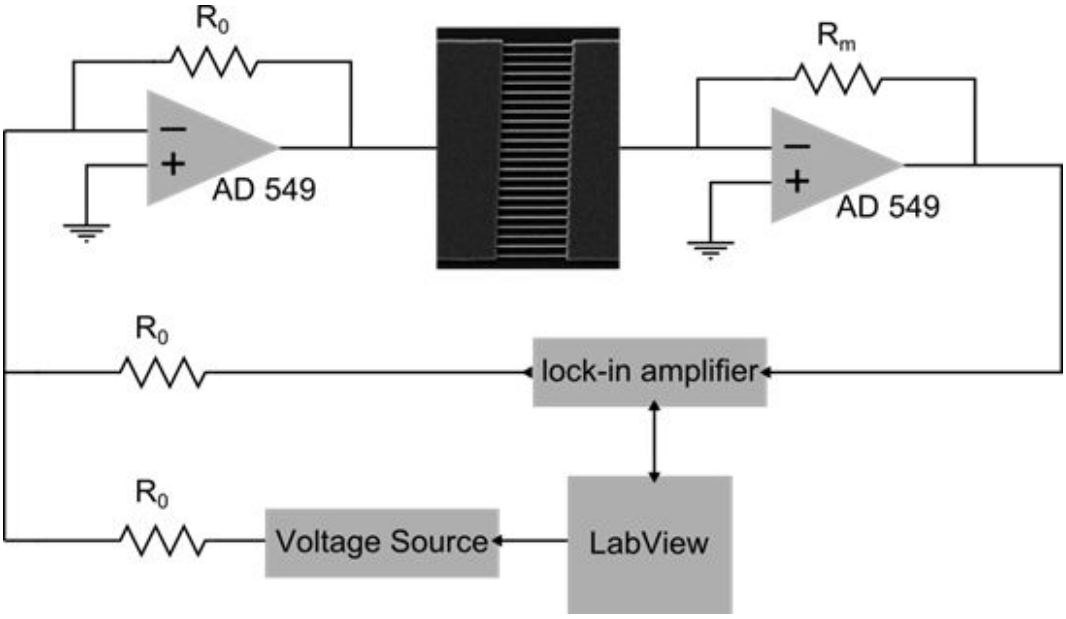

Figure 4·16: Schematic of the measurements circuit used for this experiment. A summing amplifier is used to add a small AC signal atop a DC offset while a post amplifier measures the output before being fed into a lock in amplifier (LIA).

for measurements used for measuring the differential conductance vs. time for each dilution series.

A summing amplifier is used to add a small AC signal (typically 10 mV) atop a DC offset (usually zero-volts for sub-threshold regime). A lock-in amplifier provides the AC signal while a power source provides the DC offset. The frequency of the applied AC voltage is low (typically 17 Hz). The output is amplified by a post amplifier and then fed back to the lock-in amplifier and recorded by a LabView program. The AC component of the output voltage is given by,

$$V_{AC,out} = G_{diff} \times R_m \times \frac{R_0}{R_0 + R_{LIA}} \times V_{AC,in} \tag{4.4}$$

where R_0, R_m and R_{LIA} are the summing circuit resistances, the amplifier resistance and the resistance of the lock-in amplifier. The differential conductance G_{diff} can

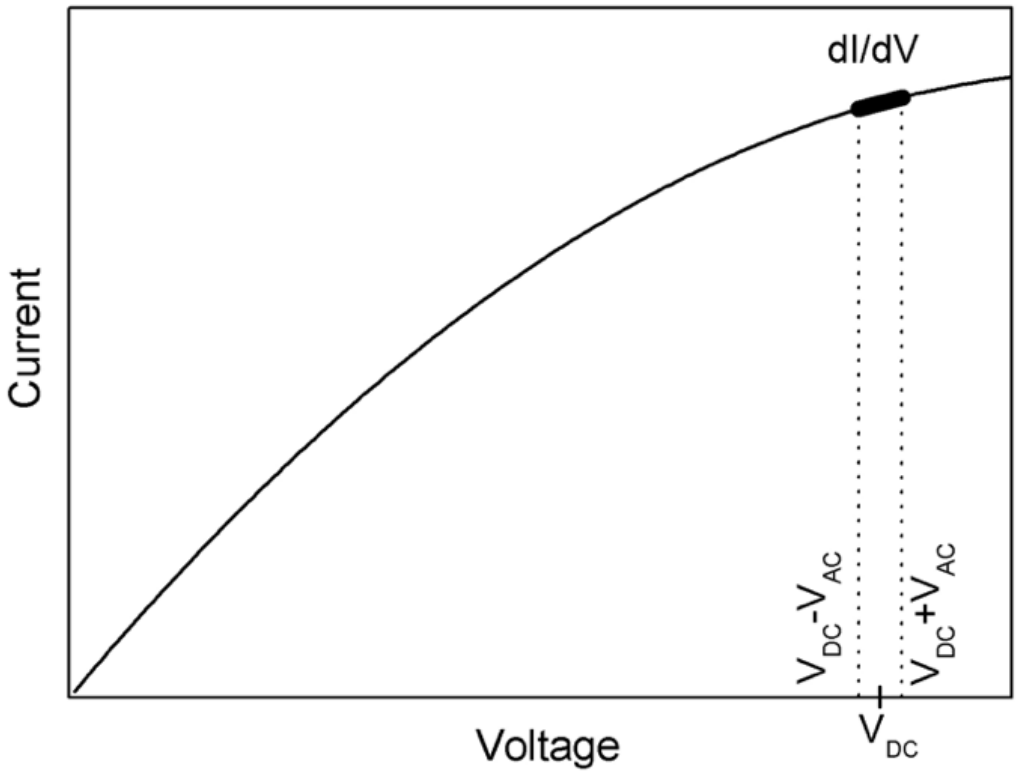

Figure 4·17: Differential conductance measurement concept. A small AC voltage measures the slope on the current-voltage curve around the applied DC voltage.

then be calculated form the output voltage sensed by the lock-in amplifier. The basics of this concept are visualized in Figure 4·17. The small AC voltage essentially approximates the slope of the I-V curve which is the dI/dV or the differential conductance.

4.8 Experimental Results

In this study silicon nanowires have been fabricated down to 60 nm in thickness and have been used to detect the NT-ProBNP bio marker which is used as the gold-standard for heart disease identification. The identification has been made in un-desalted serum which brings the device one step closer to being actually realized in

point of care applications. However we begin by discussing the results in 2 mM PBS buffer. The buffer has very low salt concentration hence it is initially used as a way of verifying the working principle of the device. Later on results in serum will be discussed.

The antigen NT-proBNP was aliquoted into vials of 250 μl each having a concentration of 20 μg/ml. This antigen was used to spike the buffer and create solutions of different concentrations namely: 20 μg/ml, 2 μg/ml, 0.2 μg/ml, 20 ng/ml, 2 ng/ml and 0.2 ng/ml. These solutions were loaded in a tubing in 50 μl each from lowest to highest concentration, each concentration separated by a 2 mM PBS wash cycle of 30 μl. A syringe pump working at 400 nl/sec dispenses the series to the device via the inlet of the fluid chamber shown in Figure 4·14 and 4·15.

Using the above log-series the devices developed in the previous section produced the conductance vs. time results as shown in Figure 4·18. It can be seen that the device responds to the lowest concentration of 200 pg/ml as well (red curve). Thus proving that the device does indeed detect NT-proBNP. In addition we tested the device by flowing 20 μg/ml (equivalent to the highest concentration of the measured NT-ProBNP) of Bovine Serum Albumin (BSA). The results show that the device does not detect non-specific proteins and only responds to analytes it has been functionalized for.

We then tested multiple devices using similar log-dilutions series except now they were all spiked in serum instead of the 2 mM PBS as before.

As per Figure 4·19, it can be seen that the device is capable of detecting the antigen NT-ProBNP in serum as well. However the lowest detectable signal is now nearly an order of magnitude higher at 2 ng/ml. Also the wash cycles in between the concentration plateaus are not as constant or flat as they used to be with the PBS signal in Figure 4·18.

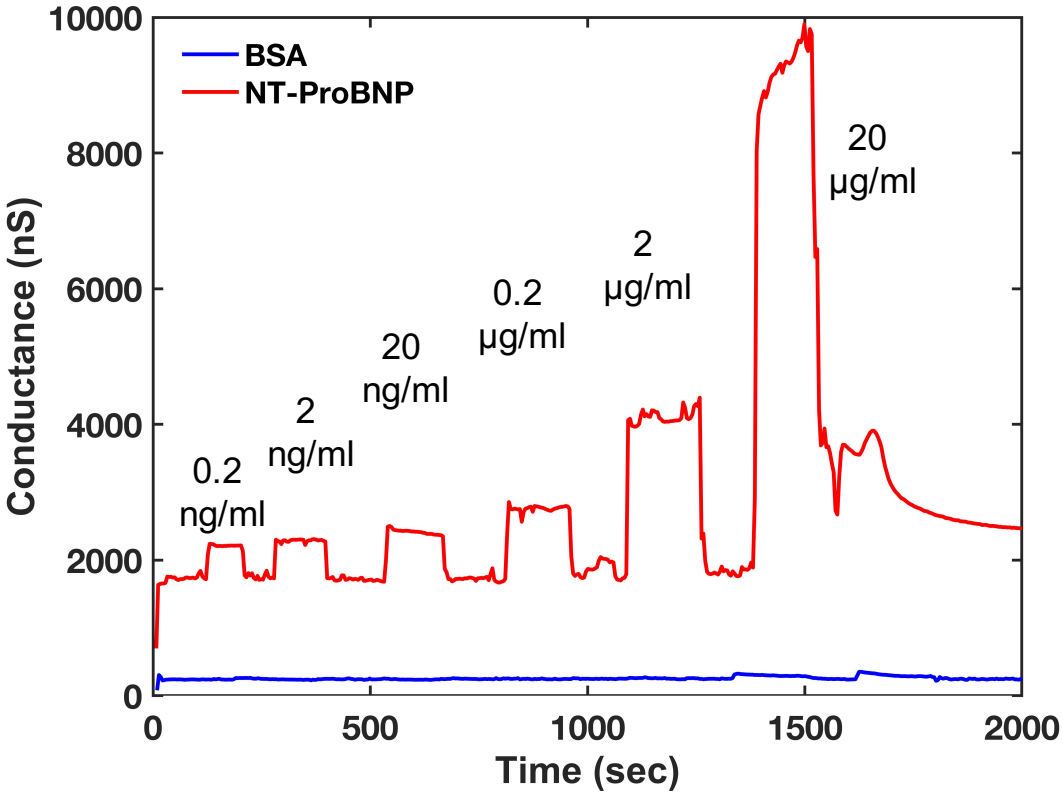

Figure 4·18: Conductance measurement vs. time for a log-concentration in 2 mM PBS buffer. Red-curve is the response for NT-ProBNP while the blue-curve is for BSA.

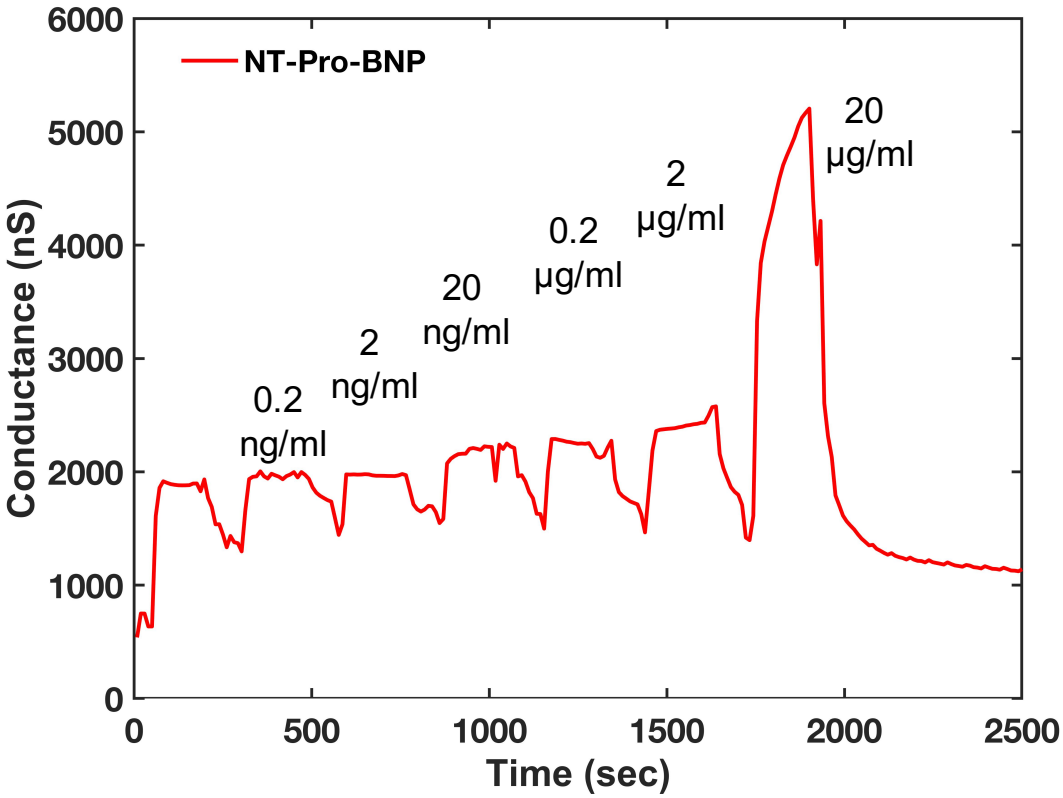

Figure 4·19: Conductance measurement vs. time for a log-concentration in Serum.

4.8.1 Differential Conductance

In this section we discuss a novel method of reducing the background noise in the measurements. Differential conductance is measured by depositing a thick layer of oxide on one set of nanowires about 200 nm - thick, and then subtracting the response of this nanowire set (covered) with respect to that of a nanowire set - open to the fluid flow. This is achieved by employing the A-B functionality of the Lock-in Amplifier (LIA). The LIA in this setup provides an input to the common drain electrode while outputs from source electrode-A and source electrode-B are input to the LIA in differential mode. The thick oxide is deposited on the individual device by coating it with PMMA and then exposing a rectangular window on top fo the nanowire set to the covered. When developed this PMMA is removed from above this set of wire and oxide is deposited using ALD process. When lift-off is done the oxide only remains over one set of nanowires.

Figure 4·20 shows the results of measuring the response of the device using a similar log-dilution series in serum. It can be observed that by employing a differential method of measurement the background immediately becomes flat and goes to zero. This is as per expectation, since background noise is applied equally to both the set of wire covered with thick oxide and that which is not covered with oxide and hence gets subtracted in the differential scheme. While the background does seem to increase for the higher concentrations however this may be due to the intrinsic nature of ion-entrapment in the oxide layer for those higher concentrations.

4.8.2 Limit of Detection

Since we have identified that the device works in its required detection application, we will now present data that will be able to identify the limit of detection for NT-ProBNP using this device.

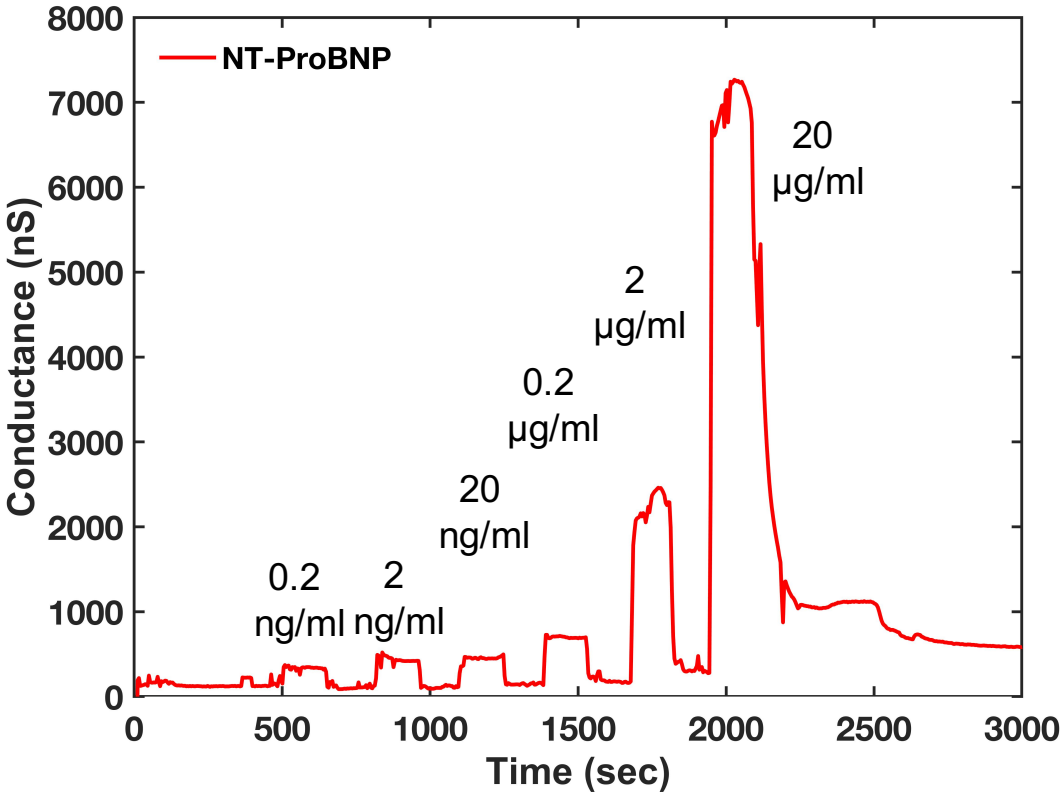

Figure 4·20: Differential conductance measurement vs. time for a log-concentration in Serum.

It was observed that log-dilution series did not completely capture the essence of the complete range of concentrations that the device may be able to detect. Hence a two fold-dilution scheme was adopted. Starting from 20 μg/ml of the analyte NT-ProBNP in serum dilutions were made which were each half of the initial. Hence the solutions (dilutions) that were created consisted of: 20 μg/ml, 10 μg/ml, 5 μg/ml, 2.5 μg/ml, 1.25 μg/ml, 625 ng/ml, 312.5 ng/ml, 156.3 ng/ml, 78.1 ng/ml, 39 ng/ml, 19.5 ng/ml, 9.7 ng/ml, 4.8 ng/ml, 2.4 ng/ml, 1.2 ng/ml, 0.61 ng/ml, and 0.31 ng/ml.

Due to the limited pumping capacity of the syringe pump can only pump about ten of these concentrations at one time, hence first a two-fold dilution series starting from 20 μg/ml is introduced with solutions down to 39 ng/ml. Response of the device is converted to a conductance versus concentration plot shown in Figure 4·21. Each data point is the average value of the each concentration plateau, while the error corresponds to the drift in the measurements. The device as expected responds to each concentration in decreasing order of response as the concentration is lowered. Figure 4·22 is the similar plot for the lower concentrations as the two-fold dilution is progressed further. It can be seen from this plot that the approximate detectable limit for NT-proBNP is about 2.5 ng/ml.

4.9 Conclusion

In this chapter we have presented Silicon Nanowires based biosensors. From there beginning this technology has proven to be far more robust and superior to other label-free detection mechanisms. In addition it lends its self to being adopted for hand-held, wearable and eventually implantable nano-scale sensors for various antigens. The device is versatile and can be functionalized for detecting any other analyte. We have presented our device fabricated down to 60 nm thick wires and then used it to detect NT-ProBNP analyte which is the gold-standard bio marker for heart disease.

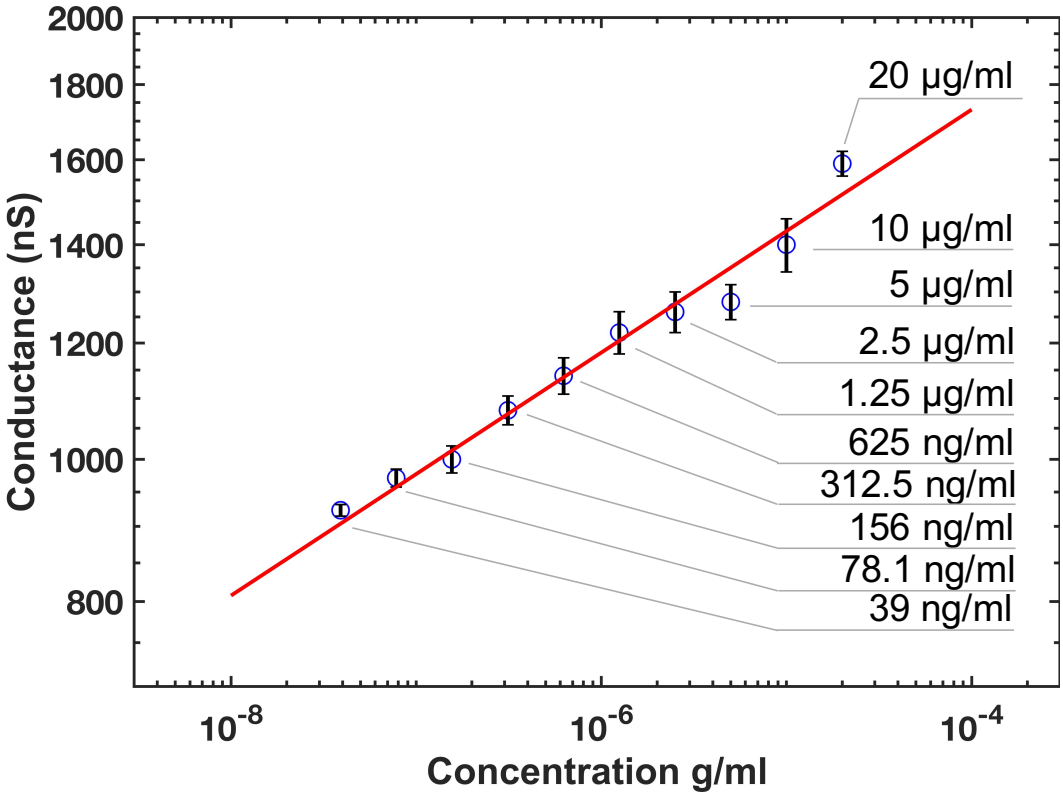

Figure 4·21: Conductance vs. concentration plot for two-fold dilution series of NT-ProBNP spiked in Serum.

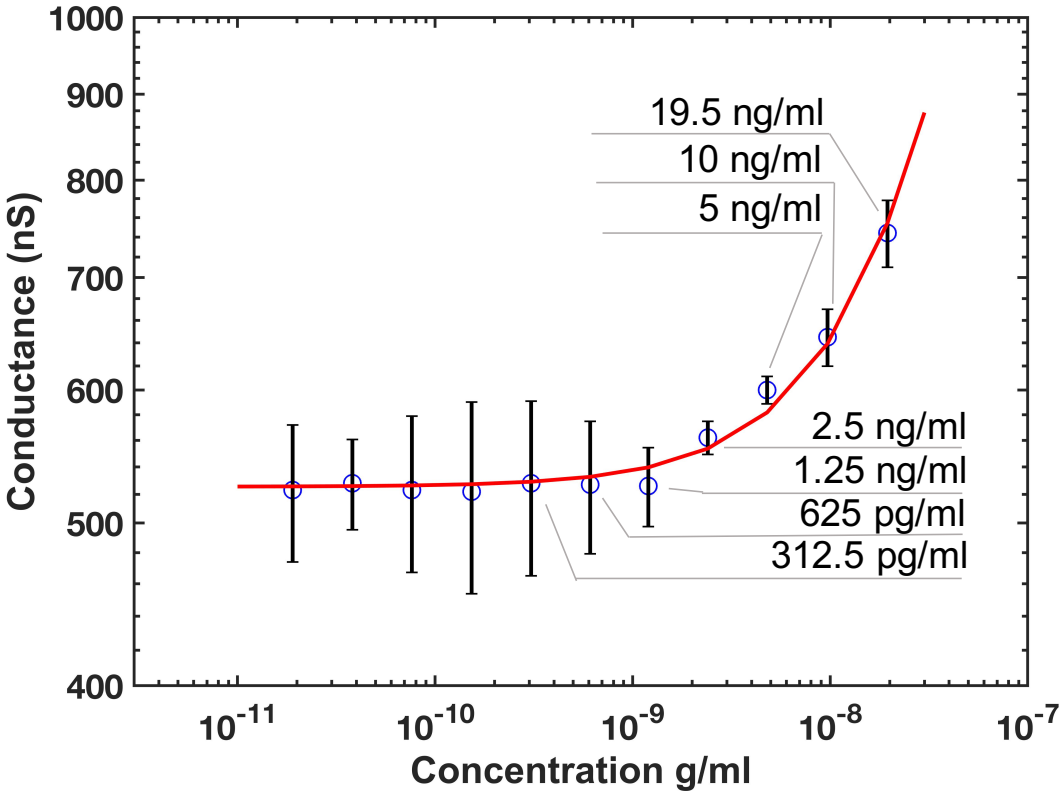

Figure 4·22: Conductance vs. concentration plot for two-fold dilution series of NT-ProBNP spiked in Serum. The plot shows the limit of detection for this device.

We have also presented a differential mode measurement technique which is shown to reduce noise in the results. In the next chapter we shall be looking into ways of enhancing sensitivity of these devices.

Chapter 5

Silicon Nanowires: Increased Sensitivity

5.1 Introduction

The promise of nanowire based bio-sensors is a label free, real-time detector which can be made orders of magnitude more sensitive by application of intelligent design and known methodologies. Hence significant effort is being paid to the realization of the same. In 2004, [Patolsky et al., 2004] demonstrated the detection of single virus molecules in buffer by the real-time correlation of conductance spikes and fluorescent tagged viruses. However the large setup needed did not allow it to be integrated into a POC device. Most groups demonstrate the detection of target analytes in lower concentration buffer to circumvent the Debye layer screening issue present in higher concentration ionic solutions such as whole blood or serum [Kim et al., 2007, Zheng et al., 2005, Chua et al., 2009]. Amougst these the Kim group has demonstrated detection of Prostrate specific Antigen (PSA) a bio-marker for prostrate cancer down to 1 fg/ml using a PBS buffer of 3 μM concentration. However it would make for a cumbersome and complicated POC device requiring the addition of a dilution buffer to bring down the concentration of serum from its usual 150 mM to the required 3 μM before the device could start detecting the PSA. In addition dilution has been shown to have an impact on the ligand-protein and protein-protein interactions [Lloret et al., 2012] and can also reduce the analyte concentration in turn requiring the sensor to be even more sensitive. Another approach which also does not lend a hand for POC applications is to desalt the serum sample before multiplex detection of

biomarkers can be made [Zheng et al., 2005]. The desalting usually has to be carried out via a centrifuge which cannot efficiently be miniaturized for on chip integration. Furthermore precious target analyte can be lost in the desalting process. Another methodology that has been adopted is the introduction of a micro-fluidic purification chip (MPC) system to pre-isolate the target analytes and release them into pure buffer for sensing via nanowire sensors [Stern et al., 2010]. This method while viable is contingent upon the effective operation of the pre-concentrator. Another method for increasing sensitivity of nanowire based biosensors has been to make a comparative measurement of the target analyte in serum with one set of nanowires with respect to another maintained in a reference buffer (lower concentration) also spiked with the target analyte [Kim et al., 2010]. These measurements would then be free of the ionic concentration of the fluid environment. It has also been shown that by only using a small fragment of the antibody, [Elnathan et al., 2012] specifically the lower end that binds to the target analyte the bio-recognition event can be brought nearer to the surface of the nanowire and thus an increase in the sensitivity can be observed.

In this chapter we present a novel method that could be used for sensitivity enhancement of nanowire biosensors. We employ dc-electric fields by an application of electric potential of up to 1V via external electrodes patterned across the nanowires and present how it enhances the sensitivity by nearly an order of magnitude. In high ionic concentration fluids the counter ions shield the charged protein molecules according to the Debye length, which is in-turn dependent on the solution concentration. This characteristic length over which the potential decays into the bulk solutions, is often denoted by λ_D and given by,

$$\lambda_D = \sqrt{\frac{\epsilon_r \epsilon_0 k_B T}{2 L_A e^2 I_c}} \tag{5.1}$$

where ϵ_0 represents the vacuum permittivity, ϵ_r is the relative permittivity of the

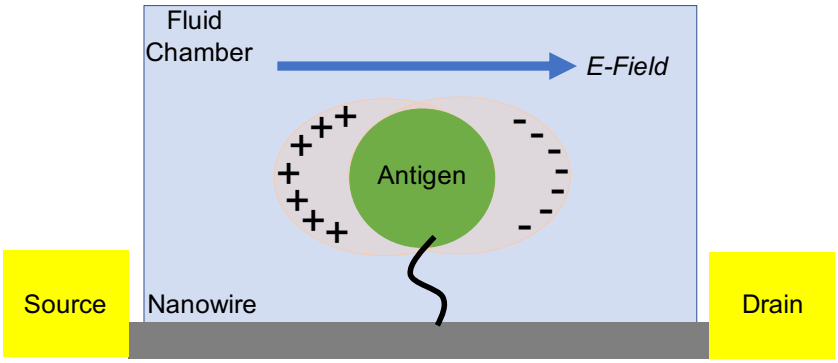

Figure 5·1: Schematic of the dipolar separation technique. A static E-field is applied to a captured target analyte molecule tethered above a silicon nanowire. The field produces a dipole whereby the counter and co-ions shielding the charged particle are displaced temporarily.

medium, k_B is the Boltzmann constant, T is the absolute temperature (K), N_A is the Avogadro's number, e stands for the elementary charge and I represents the ionic strength of the electrolytic (ionic) buffer solution. It can be seen that an ionic solution of higher strength (I) will correspond to a shorter λ_D. The Debye screening length can be thought of as the distance into the solution the nanowires can effectively "see" a target analyte. In serum the high concentration of ionic content causes the Debye length to be about 0.7 nm (150 mM). This short Debye length causes the silicon nanowire based biosensors to loose sensitivity in such solutions.

An applied static (dc) electric field can disrupt this screening by pulling apart the shielding ions from around the proteins hence creating a dipole. This dipolar separation should be proportional to an applied static electric field. This phenomena is by no means new and is the basis of electrophoresis and dielectrophoresis. It is well understood and present in standard micro-fluidic texts [Kirby, 2010]. Moreover it is actively employed in separation of charged bio-particles. In our biosensors we are effectively able to capture target proteins, hence we want to employ static electric fields in producing a dipole which would effectively de-screen the protein, allowing the nanowires below to sense them given the higher concentration of ions in the fluid.

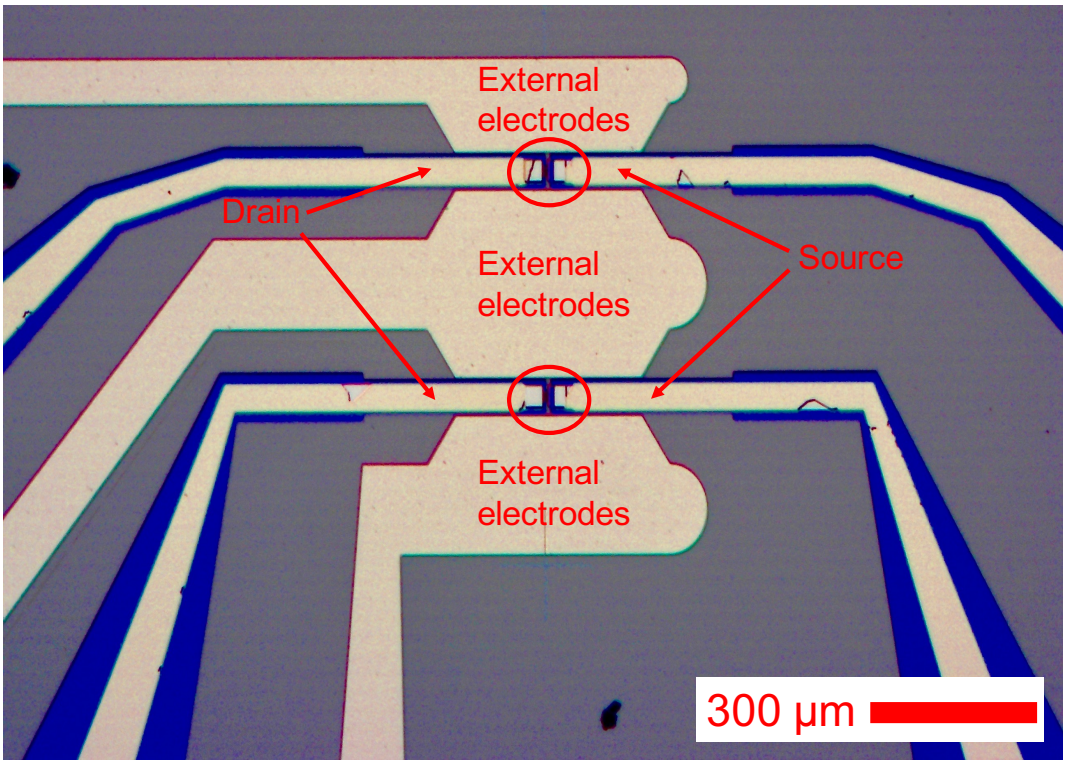

Figure 5·2: Optical micrograph for a nanowire based biosensor with external electrodes. The nanowires are present in between the (red-circled) source and drain electrodes marked.

5.2 Measurement Setup

As in Chapter 4 devices with external electrodes were fabricated through an external off-site employing similar fabrication steps as highlighted in Section 4.5. External gold electrodes were added to the fabrication steps. Figure 5·2 shows the optical micrograph of one such device. Sets of nanowires (marked by red-circles on the picture) straddle the (marked) source and drain electrodes. Each of the nanowires in these devices is about 100 nm thick ($\pm$ 5 nm).

These devices were wire-bonded, silanized, functionalized with the BNP Antibodies and affixed inside the fluid chamber via the same process as detailed in the Section 4.5 previously.

5.3 Experimental Results

Serum spiked with NT-ProBNP antigen was made up to a concentration of 5 μg/ml. This solution was flown in 50 μl quantities separated by 30 μl of 2mM PBS wash. A DC voltage was applied to create a static electric field via the external electrodes shown in Figure 5·2 and varied between 0 and 1 V with 0.2 V steps. The results are shown in Figure 5·3. In the plot it can be seen that initially at 0 volts (no external electric field) the device responds typically to the concentration of the antigen introduced. As the field is increased at every subsequent wash cycle, it can be seen that the response of the device increases almost proportionally. However between the peaks of every subsequent increase in voltage it can be seen that the baseline (wash cycle response) also increases. This may be due to the fact that the PBS buffer also contains ions albeit in a smaller concentration.

Figure 5·4 represents another run using the same concentration however it is based on the application of 0 V, 0.5 V and 1 V. The concentration of the analyte (NT-ProBNP) used for this plot is still 5 μg/ml. It can be seen that the peak responses for each subsequent increase in potential applied at the external electrodes results in a raise in response. However when the potential is kept constant the response too remains constant.

Next we make a similar measurement as that of Figure 5·4 in 2mM PBS. This was done by spiking the PBS with the NT-ProBNP to make a final concentration of 5 μg/ml. This solution was then introduced to the device as a dilution series as before interspaced by the PBS wash cycle solutions. The results shown in Figure 5·5 depict the expected results. It may be noted that the measured conductance is overall higher than that measured in serum spiked measurements of the plots before. This is due to the 2mM PBS having significantly lower salt concentration than serum which has an ionic concentration of about 150 mM.

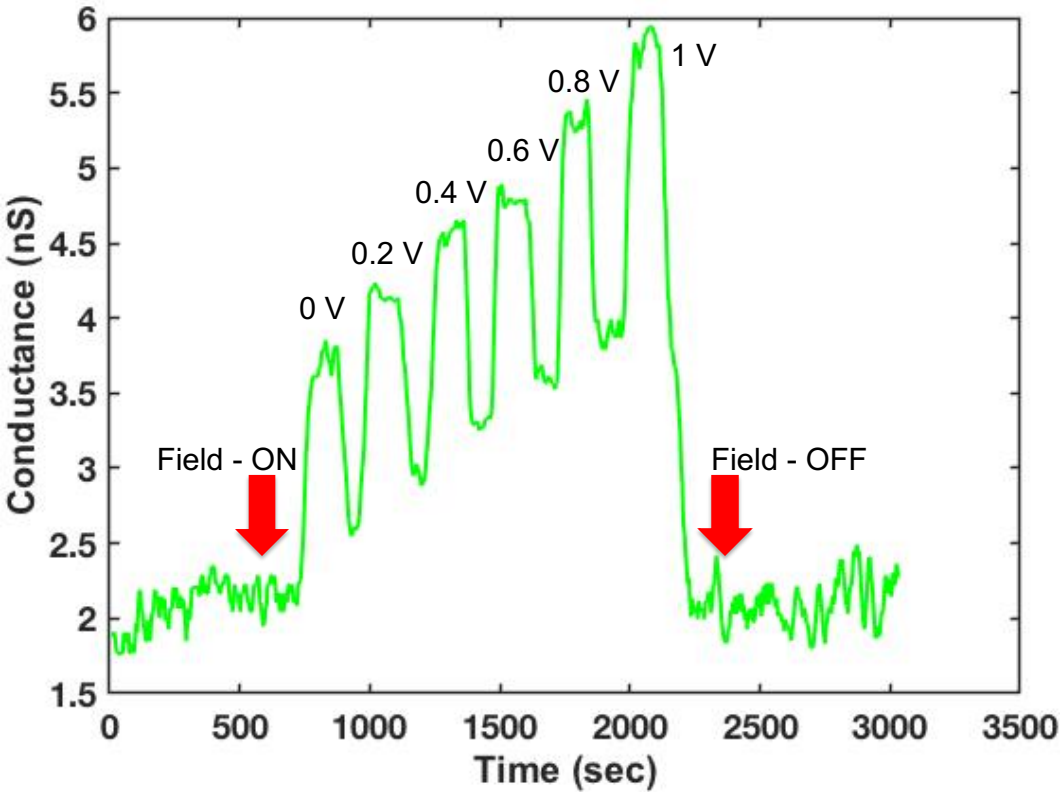

Figure 5·3: Plot of Conductance vs. time showing the results of dipolar separation via the application of static electric fields.

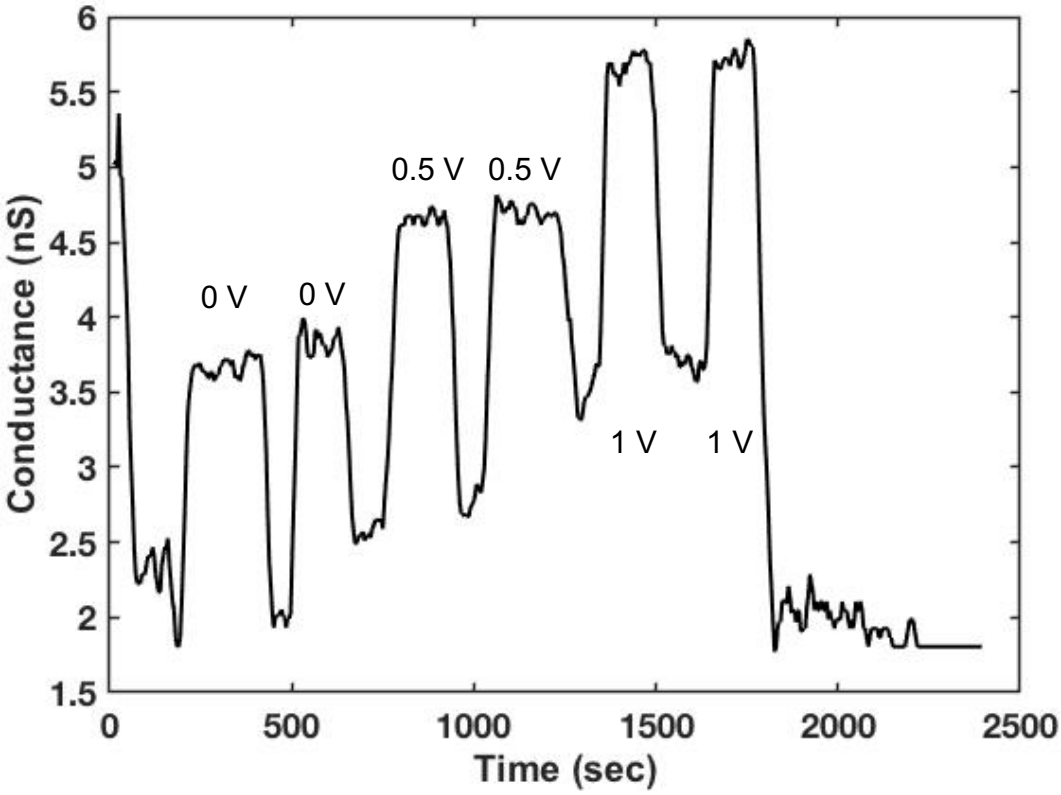

Figure 5·4: Plot of Conductance vs. time showing the results of application of static electric fields. It can be seen when the potential is increased the response increases viz-a-viz the response remaining at a constant amplitude when the potential is held constant.

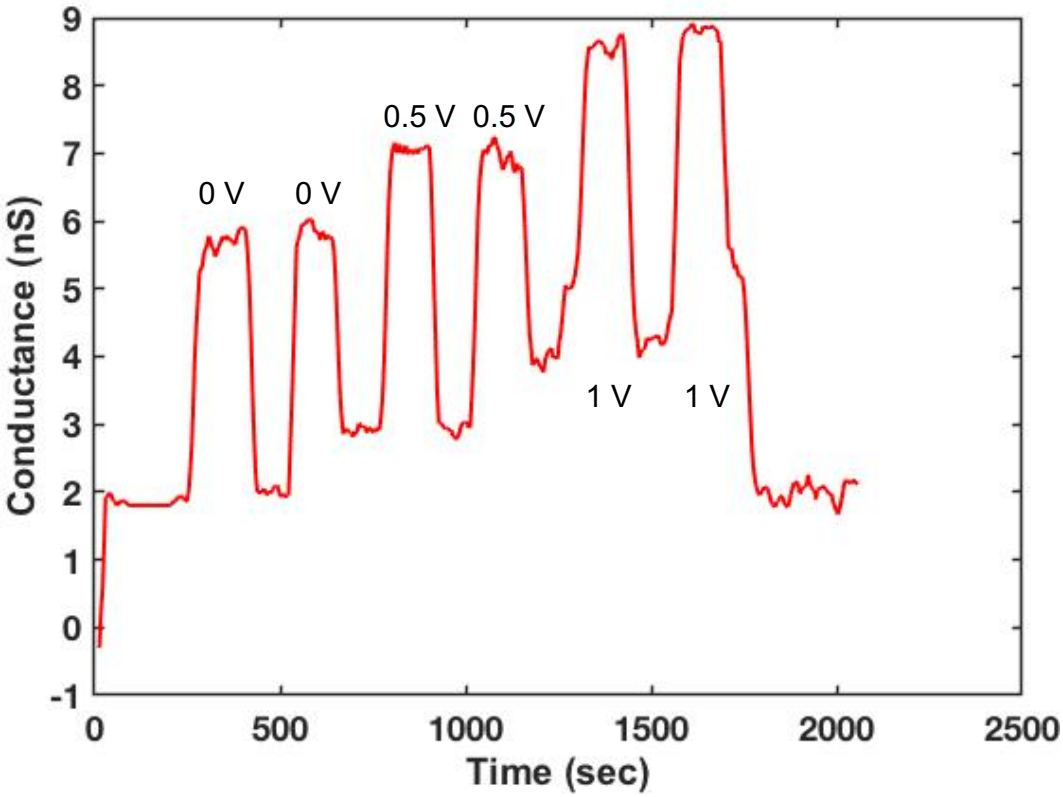

Figure 5·5: Plot of Conductance vs. time showing the results of application of static electric fields to 2mM PBS spiked with the analyte. It can be seen that the measured conductance is overall higher than that of the serum spiked plots of before - due to the significantly lower salt concentration of the PBS.

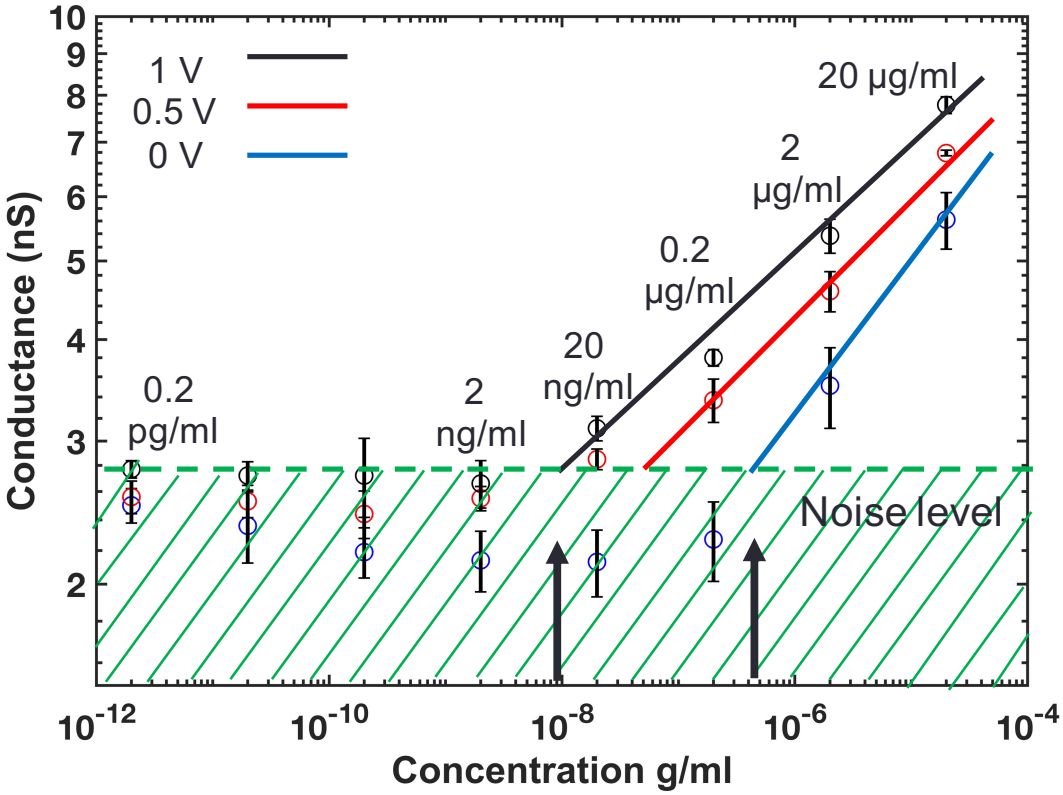

Figure 5·6: Plot of Conductance vs. concentration showing the results of application of static electric fields to dilution series runs of a log-series. It can be seen that the application of the static electric fields for both 0.5 V and 1 V increases the sensitivity by nearly an order of magnitude above the limit of detection with no electric fields (0 V).

Finally the method is used to demonstrate how it may be able to increase sensitivity of the present devices. For this a log-dilution series was prepared by spiking serum with NT-ProBNP. The concentrations used were: 20 μg/ml, 2 μg/ml, 0.2 μg/ml, 20 ng/ml, 2 ng/nl, 0.2 ng/ml, 20 pg/ml, 2 pg/ml. These runs were repeated once for each of 0 V, 0.5 V and 1 V. The results are shown in Figure 5·6.

The blue plot in the figure is the base plot for 0 V DC potential applied to the external electrodes. It can be seen that only 20 μg/ml and 2 μg/ml concentrations are discernible at this stage. All other concentrations are not discernible since they all fall rather non-intuitively. The sensor is unable to successfully differentiate between

these lower end concentrations. As the run is repeated with a voltage of 0.5 V (red-plot) we begin to observe a significant signal from the 0.2 μg/ml concentration and a smaller but promising signal from the 20 ng/ml concentration as well above the other concentrations of this run. Finally as the entire dilution series is repeated with the application of 1 V (black-plot) on the external electrodes we find that the 20 ng/ml concentration signal is more significant and above the signal from the lower end of the concentrations, which are all along a flat line indicating that these concentrations are not differentiable from each other by the sensor.

5.4 Conclusion

In this chapter we have demonstrated a method for sensitivity enhancement viz-a-viz those developed by other groups discussed in the introduction section. By the application of a static electric field delivered by external electrodes fabricated alongside the nanowires we are able to show nearly an order of magnitude increase of sensitivity over that obtained with no field applied. The potential applied to the external electrodes in this demonstration has been varied between 0 and 1 V. In theory a higher potential can be applied however during experimentation it was observed that increasing the voltage to about 1.5 V produced minuscule bubbles in the fluid chamber which holds a small sample size (10 μl) of the fluid being tested by the sensor.

Chapter 6

Conclusions

6.1 Summary of the thesis

Piezoelectric micro-mechanical resonators of various resonator element shapes and dimensions have been tested and found to be compliant with the wireless actuation mechanism at distances of over a meter and actuation power of -10 dBm (0.1 mW). The distance and polarization dependences of the same present non-intuitive responses which are explained by near field effects and multi-path interferences of the E-fields. However it is interesting to note that there is a signal registered by the device at nearly all orientations and distances from the antenna source. This may be handy for applications such as powering of either handheld, wearable or implantable biomedical devices. However the efficiency initially reported is about 3%. In Chapter 4, we have presented how accessing a higher frequency mode of similar resonators can be used to increase efficiency to 15% without any design modifications. This is due to the fact that closing the gap between the resonance frequency of the top IDT - patch antennas and the mechanical plate type resonator below enhances the energy transfer coupling between them and causes the system to become more efficient. While we restricted our observations to a source antenna power of -10 dBm (0.1 mW) it has been observed that increasing this by even a decade can improve observed results and the efficiency. Design modifications to the resonators where by mechanically the resonance frequency of the resonator is increased to a level to match or come close to the resonance of the patch antennas or equivalently to design slightly

longer patch antennas (since the resonance frequency of the patch relates inversely with its length) which would resonate at lower frequencies and thus match the resonator's resonance frequencies would yield further gains in efficiency. Conversely an array of similar resonators can be fabricated and used to capture more of the incident energy. Such a system while larger than a single resonator would still not occupy a large foot print given the micron-dimensions of a single resonator. Further more tests of these devices should be carried out with the aid of human phantom, which mimic the electrical properties of human tissues. Such experiments could guide design of future devices for maximum energy transfer for bio-implants.

In the second half of the thesis Silicon Nanowire based biosensors have been presented and discussed extensively as robust platforms of highly sensitive bio-molecule detection. We have fabricated the wires down to 60 nm thickness which has been a significant advancement in this kind of fabrication in our group. Earlier wire thicknesses used were only up to about 100 - 130 nm thick. Also using an SU-8 layer for insulation has resulted in lower leakage currents in the device as compared to previous ones. In addition a thinner gate oxide of just 5 nm has helped us make the sensitivity of the device higher in Serum. We are able to detect NT-ProBNP down to 2 ng/ml using these devices. In addition a separate set of devices are also presented having external patterned electrodes. Upon the application of DC-fields it can be seen that there is an increase in device sensitivity by nearly of an order of magnitude. Future works can look into the application of AC-fields to the fluid around the nanowires. It is expected that there will be interesting frequency dependencies of the devices. However for this an appropriate ground plane is necessary to be built onto the chip design.

In conclusion both Piezoelectric micro-mechanical resonators and Silicon Nanowire based biosensors are found to be robust platforms for wireless actuation and bio-

sensing in POC device applications, respectively. Both of them are commercially viable and in the future can be developed as either standalone products or as an integrated whole. Given there micron dimensions it is expected that both of them may eventually help save precious lives one day!

Appendix A

Butterworth Van Dyke (BVD) model

The Butterworth Van Dyke (BVD) model is traditionally used to simplify and characterize the piezoelectric resonator and consists of four lumped element components. The model (Figure A·1) consists of two arms in parallel; the first containing Capacitance C_0, which is a purely electrical quantity physically representing the capacitance between the top electrodes and the bottom ground plane, while the second arm contains the resistance R_m, inductance L_m, and capacitance C_m.

Qualitatively, these three terms represent the motional arm and determine the series resonance, where the admittance of the resonator rises to value $1/R_m$ at a frequency where the series inductance L_m cancels the series capacitance C_m. It may be noted that the S21 data was recorded for a two-port system, consisting of not only a piezoelectric resonator but also a coaxial cabling system connecting the input and output ports of the resonator. To model such a system a two-port, three-element, pi-network was used (Figure A·1). Each of the three elements in the network has discrete internal impedances namely Z_a and Z_c corresponding to the cable connections and Z_b corresponding to the BVD model of the piezoelectric resonator. The measured S-parameter data relating the ratio of output to input voltage, for this two-port pi-network was then converted to Z-parameters ($Z-11$, $Z-21$, $Z-12$ and $Z-22$) for the same, relating the input and output voltage and currents of the two-port network using conversion formulas given in literature [Pozar, 2009], using line impedance Z_0 of 50 Ω. Employing the reciprocity of a passive element network, we have $Z-21 =$

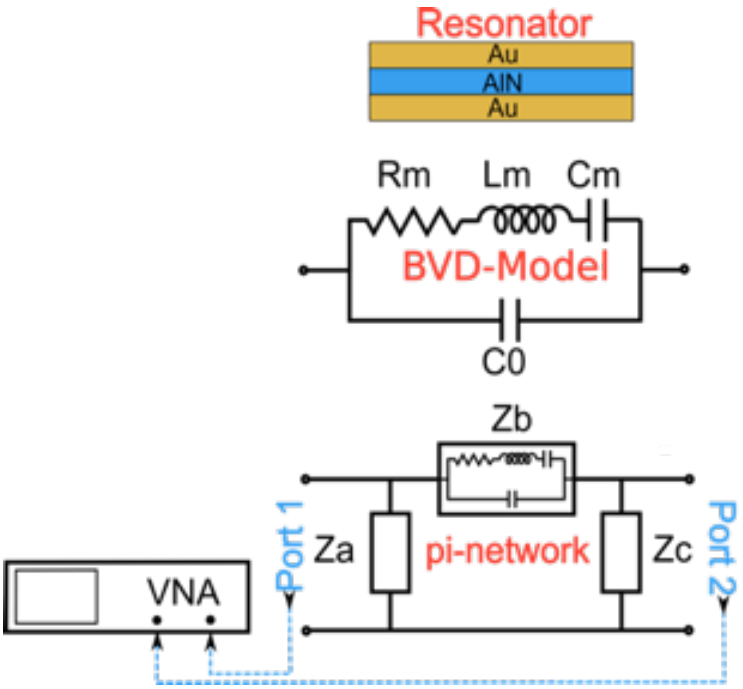

Figure A·1: The four element Butterworth Van Dyke equivalent model used to model the piezoelectric resonator consists of two parallel arms of which the series arm (top) consists of R_m, L_m and C_m which represent the mechanical motion of the resonator while the second arm (below) consists of the capacitance C_0. A two-port three-element pi-network is used to model the entire piezoelectric resonator along with connecting coaxial cables. Each element of the network has internal impedance (Z_a, Z_b and Z_c).

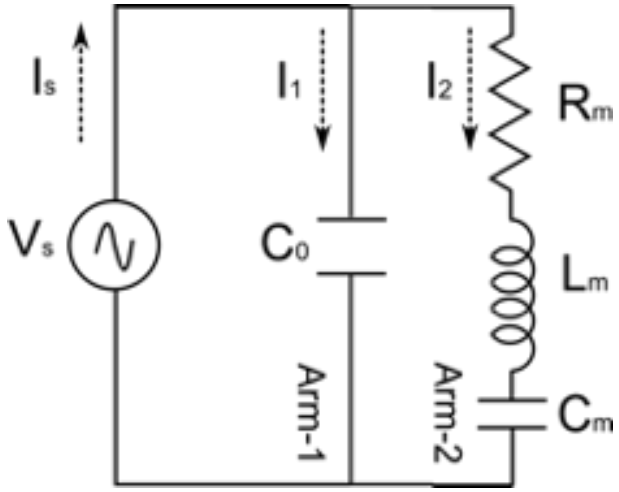

Figure A·2: The BVD model under voltage (V_s) excitation results in the total current response Is flowing in the circuit which is the sum of the currents I_1 and I_2 through each arm as shown. The voltage across each arm is equal to V_s.

$Z-12$, giving the Z-parameter equations in terms of internal impedances, Z_a, Z_b and Z_c of the pi-network.

All transformations up to this point are exact. However, the only approximation and possible source of error is modeling of the resonator and the connections by a three-element pi-network, while ignoring the more complex parasitic topologies. However, in first order approximations, this model is valid and can provide reasonable results. In particular, the impedance Z_b is of interest as it represents the input impedance of the BVD model circuit. A Matlab algorithm performs these calculations on each measured data set and converts it to the impedance Z_b from which are extracted the series and parallel resonance frequency f_s and f_p along with the corresponding impedance values z_s and z_p at the respective frequencies. These values are used with the following relations to extract the lumped elements of the BVD as shown in Figure A·2.

$$R_m = z_s \tag{A.1}$$

$$C_0 = \sqrt{\frac{1}{\omega_p^2 R z_p}} \tag{A.2}$$

$$C_m = C_0 \left(\frac{\omega_p^2}{\omega_s^2} - 1 \right) \tag{A.3}$$

$$L_m = \frac{1}{C_m \omega_s^2} \tag{A.4}$$

where, ω_s and ω_p are the corresponding angular frequencies to both f_s and f_p respectively. The response of the BVD circuit to a voltage excitation reveals the input admittance of the model. Considering a voltage excitation of the form:

$$V_S = V_0 exp^{\iota\omega t} \tag{A.5}$$

where ω is the excitation frequency hence from here the currents in the two arms can be calculated:

$$I_1 = I_{01} exp^{\iota\omega t} \tag{A.6}$$

$$I_2 = I_{02} exp^{\iota\omega t} \tag{A.7}$$

For arm-1 the voltage equations becomes

$$V_S = \frac{Q_1}{C_0} \tag{A.8}$$

where Q is the charge related to the current by the integral with respect to time. The the voltage equation for arm-2 becomes:

$$V_S = I_2 R_m + \frac{Q_2}{C_m} + L_m \frac{dI_2}{dt} \tag{A.9}$$

Using the charge-current relation from before and the voltage-current relation for

an inductor, and adding the two arm currents gives us:

$$I_S = V_S \iota\omega C_0 + \frac{V_S}{R_m - \frac{\iota}{\omega C_m} + \iota\omega L_m} \tag{A.10}$$

$$\frac{I_S}{V_S} = \iota\omega C_0 + \frac{1}{R_m - \frac{\iota}{\omega C_m} + \iota\omega L_m} \tag{A.11}$$

The LHS of the above equation is the input admittance of the BVD circuit (Y_{BVD}), which is complex, and its real (G_{BVD}) and imaginary (B_{BVD}) parts reveal the amplitude and phase information given by the following equations after simple algebraic manipulations:

$$Y_{BVD} = \left(\frac{R_m}{R_m^2 + \left(\omega L_m - \frac{1}{\omega C_m}\right)^2} \right) + \iota \left(\omega C_0 - \frac{\left(\omega L_m - \frac{1}{\omega C_m}\right)}{R_m^2 + \left(\omega L_m - \frac{1}{\omega C_m}\right)^2} \right) \tag{A.12}$$

$$G_{BVD} = \left(\frac{R_m}{R_m^2 + \left(\omega L_m - \frac{1}{\omega C_m}\right)^2} \right) \tag{A.13}$$

$$B_{BVD} = \left(\omega C_0 - \frac{\left(\omega L_m - \frac{1}{\omega C_m}\right)}{R_m^2 + \left(\omega L_m - \frac{1}{\omega C_m}\right)^2} \right) \tag{A.14}$$

The earlier calculated values of the series Resistance (R_m), Inductance (L_m) and Capacitance (C_m) from the impedance data Z_b is used to plot the real part of the admittance (G_{BVD}), which is the lorentzian response of the device. It is this response that is used through out this work for analysis of resonators.

Appendix B

Efficiency Calculation for Wireless Actuation

It is important to discuss there brief calculation here. It may be noted that the electric field undergoes fringing along the length of the patch. These fringing fields travel in both the substrate and air hence an effective dielectric constant ϵ_{eff} is used. In addition the same fringing fields causes the patch antenna to appear longer thus an effective Length L_{eff} is introduced. Analytical expressions for calculation of the effective length, dielectric constant and the resonant frequency of the patch are given by,

$$\epsilon_{eff} = \frac{\epsilon_r + 1}{2} + \frac{\epsilon_r - 1}{2}\left[1 + 12\frac{h}{W}\right]^{-\frac{1}{2}} \tag{B.1}$$

$$\triangle L = 0.412h\frac{(\epsilon_{eff} + 0.3)\left(\frac{W}{h} + 0.264\right)}{(\epsilon_{eff} - 0.258)\left(\frac{W}{h} + 0.8\right)} \tag{B.2}$$

$$L_{eff} = L + 2 \triangle L \tag{B.3}$$

where L and W are the length and width of the patch respectively while ϵ and h are the dielectric constant and height of the piezoelectric material respectively. The resonant frequency of a patch antenna is given by the equation,

$$f_r = \frac{c}{2L_{eff}\sqrt{\epsilon_{reff}}} \tag{B.4}$$

where c is the speed of light given approximately as 300 m/s. Thus for a patch of

L 87-microns, W of 25 microns, piezoelectric substrate height of 2-microns and a dielectric constant of 9.00, all corresponding to one of the patches of Device A the resonant frequency as per the above is given by 603.33 GHz.

The efficiency of Device A is dependent on the efficiency of the top interdigitated array of patch electrodes. The efficiency of this array is given as the ratio of the power the device outputs to the wireless power captured by the device from the transmission bi-conical antenna. The output power from the device can be calculated using the S21-parameter from the network analyzer (VNA) data. The input power into Device-A is taken as the power irradiating the resonator due to the transmission bi-conical antenna at each of the 10 measurement distances (6,8,10,12,16,20,24,28,32 and 36 inches). This input power is the product of the power density at each of these distances, as measured by a portable power meter, and the effective area (A_eff) of the top interdigitated array of patch antennas. The maximum effective area (A_eff) of any antenna is related to its maximum directivity by,

$$A_{eff} = \frac{\lambda^2 D_0}{4\pi} \tag{B.5}$$

where, lambda (λ) is about 2.5m corresponding to the irradiating wave at a frequency of 121.7 MHz and D_0 is the directivity of the top interdigitated patch electrode array. This directivity is the product of the directivity of a single patch electrode (D_1) and the array factor. Realizing that a patch antenna can be modeled as two radiating slots separated by a length L_eff the far-field electric field pattern is then given as,

$$E_\phi = \iota \frac{k_0 h W E_0 exp^{-\iota k_0 r}}{2\pi r} \left\{ sin\theta \frac{sinX}{X} \frac{sinZ}{Z} \right\} \tag{B.6}$$

$$X = \frac{k_0 h}{2} sin\theta cos\phi \tag{B.7}$$

$$Z = \frac{k_0 W}{2} cos\theta \tag{B.8}$$

Also $E_r \approx E_\theta \approx 0$ in the far-field. In addition for small substrate heights $k_0 h$ less than 1 so the sin(X)/X term becomes = 1, hence we get,

$$E_\phi = \iota \frac{k_0 h W E_0 exp^{-\iota k_0 r}}{2\pi r} \left\{ sin\theta \frac{sinZ}{Z} \right\} \tag{B.9}$$

where for Device-A, E_θ is the electric field (V/m), h is the patch substrate height (2e-6 m), W is the width of the patch (25e-6 m), f_r is the resonance frequency of the patch 603.33 GHz, λ_0 is the free space wavelength (5.00e-4 m), k_0 is the free space wave number (12.566e3 m -1). Then the radiation intensity U (W/sr) is given by,

$$U = \frac{r^2}{2\eta_0} [E_\phi]^2 = \left(\frac{r^2}{2\eta_0} \right) \left(\frac{k_0 h W E_0}{2\pi r} \right)^2 \left\{ sin\theta \frac{sinZ}{Z} \right\}^2 \tag{B.10}$$

$$X = \frac{k_0 h}{2} sin\theta cos\phi \tag{B.11}$$

$$Z = \frac{k_0 W}{2} cos\theta \tag{B.12}$$

where η_0 is the impedance of free space about 377 Ω. The product of the electric field and the height of the substrate gives the voltage across each slot. Hence the power radiated P_{rad} (W) can be calculated via the integration of the radiation intensity U (W/sr), over the solid angles.

$$P_{rad} = \oint_0^{2\pi} \oint_0^{pi} U sin\theta d\theta d\phi \tag{B.13}$$

P_{rad} is given in Watts (W) and the element solid angle $d\Omega = sin\theta d\theta d\phi$, thus integrating the radiation intensity equation over the solid angles, we get P_{rad} as,

$$P_{rad} = \frac{|V_0|^2}{2\pi\eta_0} \int_0^{\pi} \left(\frac{sin\left(\frac{k_0 W}{2} - cos\theta\right)}{cos\theta} \right)^2 sin^2\theta sin\theta d\theta \tag{B.14}$$

Directivity of an antenna is the ratio of the radiation intensity (U_{max}) in a given

direction from the antenna to the radiation intensity averaged over all directions (U_0). The average radiation intensity $U_0 = (P_{rad})/4\pi$. Given that,

$$D_1 = \frac{4\pi U_{max}}{P_{rad}} \tag{B.15}$$

where U_{max} is the maximum radiation intensity (W/solid angle), P_{rad} is the total power radiated (W). The maximum radiation intensity given as U_{max} (W/sr) as follows,

$$U_{max} = \left(\frac{r^2}{2\eta_0}\right)\left(\frac{k_0 W h E_0}{2\pi r}\right)^2 \tag{B.16}$$

which reduces to,

$$U_{max} = \frac{|V_0|^2}{2\eta_0 \pi^2}\left(\frac{\pi W}{\lambda_0}\right)^2 \tag{B.17}$$

where $k_0 = \frac{2\pi}{\lambda_0}$

Thus the directivity of a single slot using the above becomes,

$$D_1 = \frac{U_{max}}{U_0} = \frac{4\pi U_{max}}{P_{rad}} = \frac{4\pi \frac{|V_0|^2}{2\pi^2\eta_0}\left(\frac{\pi W}{\lambda_0}\right)}{\frac{|V_0|^2}{2\pi\eta_0} I} \tag{B.18}$$

where,

$$I = \int_0^{\pi} \left(\frac{sin\left(\frac{k_0 W}{2} cos\theta\right)}{cos\theta}\right)^2 sin^2\theta sin\theta d\theta \tag{B.19}$$

$$D_1 = \left(\frac{2\pi W}{\lambda_0}\right)^2 \frac{1}{I_1} \tag{B.20}$$

A numerical estimation for the integral I, is given as,

$$I_1 = -2 + cos(X) + XS_i(X) + \frac{sin(X)}{X} \tag{B.21}$$

where, W is the width of the patch (25 μm), h is the height of the substrate (2 μm), f_r is the resonance frequency of the patch 603.33 GHz, λ_0 is the free space wavelength (0.5 mm), k_0 is the free space wave number given by (12566.66), $X = k_0 W = 0.3$ and S_i is the sine integral for which the values can be found from tables given in [con,]. This gives an I_1 of 0.03 for $X = 0.3$.

The directivity D1 for the first slot comes out to be 3.2898 (dimensionless). The directivity of the second slot can be calculated considering that the two slots separated by distance L_eff from a linear array of two elements for which the directivity (D_{slots}) is given by,

$$D_{slots} = \frac{2Nd}{\lambda} \tag{B.22}$$

where $N = 2$ (number of elements), d is the distance between the slots (0.8869 μm), λ is the free space wavelength given before. This gives a D_{slots} of 0.7095, using it with $D_1 = 3.2898$ the directivity for one patch is given by $D_{patch} = D_1 x D_{slots} = 2.334$ which is the directivity of a single patch antenna for Device A. There are 4 sets of interdigitated patch antennas in Device A (8 patch antennas in total) out of these the signal output is only from one set of 4 patch antennas. Hence the product of the directivity of a single patch (2.334) and the directivity of the linear array of 4 patch antennas each separated form the other by a distance d of 37.86 μm gives an array directivity D_{array} of 0.6057.

Thus the total directivity D_0 as $D_0 = D_{patch} * D_{array} = 1.4138$

This total directivity can be used now to calculate the effective area (A_{eff}) of the patch antenna as given by the expression before. Once the effective area is known the input power to Device A can be calculated and thus the efficiency as described earlier.

References

Abazari, M. and Abbey, C. (2010). 2010 index ieee transactions on ultrasonics, ferroelectrics and frequency control vol. 57. *IEEE Transactions on Ultrasonics, Ferroelectrics, and Frequency Control*, 57(12):2851.

Ajami, S. and Teimouri, F. (2015). Features and application of wearable biosensors in medical care. *Journal of research in medical sciences: the official journal of Isfahan University of Medical Sciences*, 20(12):1208.

Akter, R., Rahman, M. A., and Rhee, C. K. (2012). Amplified electrochemical detection of a cancer biomarker by enhanced precipitation using horseradish peroxidase attached on carbon nanotubes. *Analytical chemistry*, 84(15):6407–6415.

Arntz, Y., Seelig, J. D., Lang, H., Zhang, J., Hunziker, P., Ramseyer, J., Meyer, E., Hegner, M., and Gerber, C. (2002). Label-free protein assay based on a nanomechanical cantilever array. *Nanotechnology*, 14(1):86.

Bao, X., Burkhard, W., Varadan, V., and Varadan, V. (1987). Saw temperature sensor and remote reading system. In *IEEE 1987 Ultrasonics Symposium*, pages 583–586. IEEE.

Bergveld, P. (1970). Development of an ion-sensitive solid-state device for neurophysiological measurements. *IEEE Transactions on Biomedical Engineering*, (1):70–71.

Bergveld, P. (2003). Thirty years of isfetology: What happened in the past 30 years and what may happen in the next 30 years. *Sensors and Actuators B: Chemical*, 88(1):1–20.

Bjurström, J., Katardjiev, I., and Yantchev, V. (2005). Lateral-field-excited thin-film lamb wave resonator. *Applied Physics Letters*, 86(15):154103.

Blaha, C. D., Chang, S.-Y., Bennet, K. E., and Lee, K. H. (2015). Electrochemical recordings during deep brain stimulation in animals and humans: Wincs, mincs, and closed-loop dbs. In *Compendium of in vivo monitoring in real-time molecular neuroscience*, pages 225–250. World Scientific.

Boisen, A., Dohn, S., Keller, S. S., Schmid, S., and Tenje, M. (2011). Cantilever-like micromechanical sensors. *Reports on Progress in Physics*, 74(3):036101.

Bolomey, L., Meurville, E., and Ryser, P. (2009). Implantable ultra-low power dsp-based system for a miniature chemico-rheological biosensor. *Procedia Chemistry*, 1(1):1235–1238.

Brown, M. E. and Gallagher, P. K. (2011). *Handbook of thermal analysis and calorimetry: recent advances, techniques and applications*, volume 5. Elsevier.

Bruckner-Lea, C. J. (2004). Biosensor systems for homeland security. *Interface*, 13(2):36–42.

Bunimovich, Y. L., Shin, Y. S., Yeo, W.-S., Amori, M., Kwong, G., and Heath, J. R. (2006). Quantitative real-time measurements of dna hybridization with alkylated nonoxidized silicon nanowires in electrolyte solution. *Journal of the American Chemical Society*, 128(50):16323–16331.

Caliò, R., Rongala, U. B., Camboni, D., Milazzo, M., Stefanini, C., De Petris, G., and Oddo, C. M. (2014). Piezoelectric energy harvesting solutions. *Sensors*, 14(3):4755–4790.

Cha, K. H., Jensen, G. C., Balijepalli, A. S., Cohan, B. E., and Meyerhoff, M. E. (2014). Evaluation of commercial glucometer test strips for potential measurement of glucose in tears. *Analytical chemistry*, 86(3):1902–1908.

Chaste, J., Eichler, A., Moser, J., Ceballos, G., Rurali, R., and Bachtold, A. (2012). A nanomechanical mass sensor with yoctogram resolution. *Nature nanotechnology*, 7(5):301.

Chen, D. M., Kuypers, J. H., Mohanty, P., Schoepf, K. J., Zolfagharkhani, G., Goodelle, J., and Rebel, R. (2015). Microelectromechanical systems (mems) resonators and related apparatus and methods. US Patent 9,030,080.

Chen, Z., Fan, L., Zhang, S.-y., and Zhang, H. (2016). Performance optimization of high-order lamb wave sensors based on silicon carbide substrates. *Ultrasonics*, 65:296–303.

Chiu, K.-H., Chen, H.-R., and Huang, S. R.-S. (2007). High-performance film bulk acoustic wave pressure and temperature sensors. *Japanese journal of applied physics*, 46(4R):1392.

Choujaa, A., Tirole, N., Bonjour, C., Martin, G., Hauden, D., Blind, P., Cachard, A., and Pommier, C. (1995). Aln/silicon lamb-wave microsensors for pressure and gravimetric measurements. *Sensors and Actuators A: Physical*, 46(1-3):179–182.

Chow, E. Y., Yang, C.-L., Ouyang, Y., Chlebowski, A. L., Irazoqui, P. P., and Chappell, W. J. (2011). Wireless powering and the study of rf propagation through ocular tissue for development of implantable sensors. *IEEE Transactions on Antennas and Propagation*, 59(6):2379–2387.

Chua, J. H., Chee, R.-E., Agarwal, A., Wong, S. M., and Zhang, G.-J. (2009). Label-free electrical detection of cardiac biomarker with complementary metal-oxide semiconductor-compatible silicon nanowire sensor arrays. *Analytical chemistry*, 81(15):6266–6271.

Clark, L. C. and Lyons, C. (1962). Electrode systems for continuous monitoring in cardiovascular surgery. *Annals of the New York Academy of sciences*, 102(1):29–45.

Cleland, A. N. (2013). *Foundations of nanomechanics: from solid-state theory to device applications*. Springer Science & Business Media.

Cui, Y., Wei, Q., Park, H., and Lieber, C. M. (2001). Nanowire nanosensors for highly sensitive and selective detection of biological and chemical species. *Science*, 293(5533):1289–1292.

Da Cunha, C., Boschen, S. L., Gómez-a, A., Ross, E. K., Gibson, W. S., Min, H.-K., Lee, K. H., and Blaha, C. D. (2015). Toward sophisticated basal ganglia neuromodulation: review on basal ganglia deep brain stimulation. *Neuroscience & Biobehavioral Reviews*, 58:186–210.

Dagdeviren, C., Yang, B. D., Su, Y., Tran, P. L., Joe, P., Anderson, E., Xia, J., Doraiswamy, V., Dehdashti, B., Feng, X., Lu, B., Poston, R., Khalpey, Z., Ghaffari, R., Huang, Y., Slepian, M. J., and Rogers, J. A. (2014). Conformal piezoelectric energy harvesting and storage from motions of the heart, lung, and diaphragm. *Proceedings of the National Academy of Sciences*, 111(5):1927–1932.

De Klerk, J. (1975). 1975 ultrasonics symposium proceedings. In *Ultrasonics Symposium (1975: Los Angeles, Calif.)*. Institute of Electrical and Electronics Engineers.

Dong, S., Li, L., Gui, Z., Zhou, T., and Zhang, X.-w. (1995). A new type of linear piezoelectric stepper motor. *IEEE Transactions on Components, Packaging, and Manufacturing Technology: Part A*, 18(2):257–260.

Dorignac, J., Gaidarzhy, A., and Mohanty, P. (2009). Arbitrary distribution and nonlinear modal interaction in coupled nanomechanical resonators. *Journal of Applied Physics*, 105(10):103520.

Duarte-Guevara, C., Lai, F.-L., Cheng, C.-W., Reddy Jr, B., Salm, E., Swaminathan, V., Tsui, Y.-K., Tuan, H. C., Kalnitsky, A., Liu, Y.-S., et al. (2014). Enhanced biosensing resolution with foundry fabricated individually addressable dual-gated isfets. *Analytical chemistry*, 86(16):8359–8367.

Elnathan, R., Kwiat, M., Pevzner, A., Engel, Y., Burstein, L., Khatchtourints, A., Lichtenstein, A., Kantaev, R., and Patolsky, F. (2012). Biorecognition layer engineering: overcoming screening limitations of nanowire-based fet devices. *Nano letters*, 12(10):5245–5254.

Enz, C. C. and Kaiser, A. (2012). *MEMS-based circuits and systems for wireless communication*. Springer Science & Business Media.

Fanget, S., Hentz, S., Puget, P., Arcamone, J., Matheron, M., Colinet, E., Andreucci, P., Duraffourg, L., Myers, E., and Roukes, M. (2011). Gas sensors based on gravimetric detection?a review. *Sensors and Actuators B: Chemical*, 160(1):804–821.

Ferrari, A. C., Bonaccorso, F., Fal'Ko, V., Novoselov, K. S., Roche, S., Bøggild, P., Borini, S., Koppens, F. H., Palermo, V., Pugno, N., et al. (2015). Science and technology roadmap for graphene, related two-dimensional crystals, and hybrid systems. *Nanoscale*, 7(11):4598–4810.

Fritz, J., Baller, M., Lang, H., Rothuizen, H., Vettiger, P., Meyer, E., Güntherodt, H.-J., Gerber, C., and Gimzewski, J. (2000). Translating biomolecular recognition into nanomechanics. *Science*, 288(5464):316–318.

Gaidarzhy, A., Imboden, M., Mohanty, P., Rankin, J., and Sheldon, B. W. (2007). High quality factor gigahertz frequencies in nanomechanical diamond resonators. *Applied Physics Letters*, 91(20):203503.

Gao, X. P., Zheng, G., and Lieber, C. M. (2009). Subthreshold regime has the optimal sensitivity for nanowire fet biosensors. *Nano letters*, 10(2):547–552.

García-Gancedo, L., Zhu, Z., Iborra, E., Clement, M., Olivares, J., Flewitt, A., Milne, W., Ashley, G., Luo, J., Zhao, X., et al. (2011). Aln-based baw resonators with cnt electrodes for gravimetric biosensing. *Sensors and Actuators B: Chemical*, 160(1):1386–1393.

Gautschi, G. (2002). Piezoelectric sensors. In *Piezoelectric Sensorics*, pages 73–91. Springer.

Ghafar-Zadeh, E. (2015). Wireless integrated biosensors for point-of-care diagnostic applications. *Sensors*, 15(2):3236–3261.

Giljohann, D. A. and Mirkin, C. A. (2009). Drivers of biodiagnostic development. *Nature*, 462(7272):461.

Giurgiutiu, V. (2005). Tuned lamb wave excitation and detection with piezoelectric wafer active sensors for structural health monitoring. *Journal of intelligent material systems and structures*, 16(4):291–305.

Goeders, K. M., Colton, J. S., and Bottomley, L. A. (2008). Microcantilevers: sensing chemical interactions via mechanical motion. *Chemical reviews*, 108(2):522–542.

Grudkowski, T., Black, J., Reeder, T., Cullen, D., and Wagner, R. (1980). Fundamental mode vhf/uhf minature acoustic resonators and filters on silicon. *Applied Physics Letters*, 37(11):993–995.

Guo, X. (2012). Surface plasmon resonance based biosensor technique: a review. *Journal of biophotonics*, 5(7):483–501.

Gupta, R. K., Periyakaruppan, A., Meyyappan, M., and Koehne, J. E. (2014). Label-free detection of c-reactive protein using a carbon nanofiber based biosensor. *Biosensors and Bioelectronics*, 59:112–119.

Gyselinckx, B., Penders, J., and Vullers, R. (2007). Potential and challenges of body area networks for cardiac monitoring. *Journal of electrocardiology*, 40(6):S165–S168.

He, X., Garcia-Gancedo, L., Jin, P., Zhou, J., Wang, W., Dong, S., Luo, J., Flewitt, A., and Milne, W. (2012). Film bulk acoustic resonator pressure sensor with self temperature reference. *Journal of Micromechanics and Microengineering*, 22(12):125005.

Hemsel, T. and Wallaschek, J. (2000). Survey of the present state of the art of piezoelectric linear motors. *Ultrasonics*, 38(1-8):37–40.

Hickernell, F. S. (2003). The piezoelectric semiconductor and acoustoelectronic device development in the sixties. In *Proceedings of the 2003 IEEE International Frequency Control Symposium and PDA Exhibition Jointly with the 17th European Frequency and Time Forum, 2003.*, pages 1012–1020. IEEE.

Higson, S. P., Reddy, S. M., and Vadgama, P. (1994). Enzyme and other biosensors: Evolution of a technology. *Engineering Science & Education Journal*, 3(1):41–48.

Ho, J. S., Yeh, A. J., Neofytou, E., Kim, S., Tanabe, Y., Patlolla, B., Beygui, R. E., and Poon, A. S. (2014). Wireless power transfer to deep-tissue microimplants. *Proceedings of the National Academy of Sciences*, 111(22):7974–7979.

Homola, J. (2008). Surface plasmon resonance sensors for detection of chemical and biological species. *Chemical reviews*, 108(2):462–493.

Imboden, M. and Mohanty, P. (2014). Dissipation in nanoelectromechanical systems. *Physics Reports*, 534(3):89–146.

Imboden, M., Williams, O. A., and Mohanty, P. (2013). Observation of nonlinear dissipation in piezoresistive diamond nanomechanical resonators by heterodyne down-mixing. *Nano letters*, 13(9):4014–4019.

Johnston, M. L., Edrees, H., Kymissis, I., and Shepard, K. L. (2012). Integrated voc vapor sensing on fbar-cmos array. In *IEEE 25th International Conference on Micro Electro Mechanical Systems (MEMS), 2012*, pages 846–849. IEEE.

Jung, W.-S., Kang, M.-G., Moon, H. G., Baek, S.-H., Yoon, S.-J., Wang, Z.-L., Kim, S.-W., and Kang, C.-Y. (2015). High output piezo/triboelectric hybrid generator. *Scientific reports*, 5:9309.

Kim, A., Ah, C. S., Park, C. W., Yang, J.-H., Kim, T., Ahn, C.-G., Park, S. H., and Sung, G. Y. (2010). Direct label-free electrical immunodetection in human serum using a flow-through-apparatus approach with integrated field-effect transistors. *Biosensors and Bioelectronics*, 25(7):1767–1773.

Kim, A., Ah, C. S., Yu, H. Y., Yang, J.-H., Baek, I.-B., Ahn, C.-G., Park, C. W., Jun, M. S., and Lee, S. (2007). Ultrasensitive, label-free, and real-time immunodetection using silicon field-effect transistors. *Applied Physics Letters*, 91(10):103901.

Kim, T.-i., McCall, J. G., Jung, Y. H., Huang, X., Siuda, E. R., Li, Y., Song, J., Song, Y. M., Pao, H. A., Kim, R.-H., et al. (2013). Injectable, cellular-scale optoelectronics with applications for wireless optogenetics. *Science*, 340(6129):211–216.

Kirby, B. J. (2010). *Micro-and nanoscale fluid mechanics: transport in microfluidic devices*. Cambridge university press.

Kirsch, J., Siltanen, C., Zhou, Q., Revzin, A., and Simonian, A. (2013). Biosensor technology: recent advances in threat agent detection and medicine. *Chemical Society Reviews*, 42(22):8733–8768.

Knopfmacher, O., Tarasov, A., Fu, W., Wipf, M., Niesen, B., Calame, M., and Schonenberger, C. (2010). Nernst limit in dual-gated si-nanowire fet sensors. *Nano letters*, 10(6):2268–2274.

Kurs, A., Karalis, A., Moffatt, R., Joannopoulos, J. D., Fisher, P., and Soljačić, M. (2007). Wireless power transfer via strongly coupled magnetic resonances. *Science*, 317(5834):83–86.

Kuypers, J. H., Lin, C.-M., Vigevani, G., and Pisano, A. P. (2008). Intrinsic temperature compensation of aluminum nitride lamb wave resonators for multiple-frequency references. In *2008 IEEE International Frequency Control Symposium*, pages 240–249. IEEE.

Lakin, K. and Wang, J. (1980). Uhf composite bulk wave resonators. In *1980 Ultrasonics Symposium*, pages 834–837. IEEE.

Lakin, K. M., Kline, G. R., and McCarron, K. T. (1995). Development of miniature filters for wireless applications. *IEEE Transactions on Microwave Theory and Techniques*, 43(12):2933–2939.

Lamb, H. (1917). On waves in an elastic plate. *Proceedings of the Royal Society of London. Series A*, 93(648):114–128.

Lewitus, D. Y., Smith, K. L., Landers, J., Neimark, A. V., and Kohn, J. (2014). Bioactive agarose carbon-nanotube composites are capable of manipulating brain–implant interface. *Journal of applied polymer science*, 131(14).

Liedberg, B., Nylander, C., and Lunström, I. (1983). Surface plasmon resonance for gas detection and biosensing. *Sensors and actuators*, 4:299–304.

Lin, A., Yu, H., Waters, M. S., Kim, E. S., and Goodman, S. D. (2008). Explosive trace detection with fbar-based sensor. In *IEEE 21st International Conference on Micro Electro Mechanical Systems, 2008. MEMS 2008*, pages 208–211. IEEE.

Lin, C.-M., Chen, Y.-Y., Felmetsger, V. V., Senesky, D. G., and Pisano, A. P. (2012). Aln/3c–sic composite plate enabling high-frequency and high-q micromechanical resonators. *Advanced Materials*, 24(20):2722–2727.

Lin, C.-M., Yantchev, V., Zou, J., Chen, Y.-Y., and Pisano, A. P. (2014). Micromachined one-port aluminum nitride lamb wave resonators utilizing the lowest-order symmetric mode. *Journal of microelectromechanical systems*, 23(1):78–91.

Lloret, N., Frederiksen, R. S., Møller, T. C., Rieben, N. I., Upadhyay, S., De Vico, L., Jensen, J. H., Nygård, J., and Martinez, K. L. (2012). Effects of buffer composition and dilution on nanowire field-effect biosensors. *Nanotechnology*, 24(3):035501.

Lu, X., Lee, C. M., Wu, S. Y., Ho, H. P., and Lau, K. M. (2013). Gan-based s0-wave sensors on silicon for chemical and biological sensing in liquid environments. *IEEE Sensors Journal*, 13(4):1245–1251.

Mannoor, M. S., Tao, H., Clayton, J. D., Sengupta, A., Kaplan, D. L., Naik, R. R., Verma, N., Omenetto, F. G., and McAlpine, M. C. (2012). Graphene-based wireless bacteria detection on tooth enamel. *Nature communications*, 3:763.

Mateen, F., Brown, B., Erramilli, S., and Mohanty, P. (2016). Wireless actuation of bulk acoustic modes in micromechanical resonators. *Applied Physics Letters*, 109(7):073502.

Matsumoto, H., Asai, K., and Hikita, M. (2004). Development of film bulk acoustic wave resonators based on piezoelectric aluminum nitride. *The Journal of the Acoustical Society of America*, 116(4):2544–2544.

Mehrvar, M. and Abdi, M. (2004). Recent developments, characteristics, and potential applications of electrochemical biosensors. *Analytical sciences*, 20(8):1113–1126.

Mei, H. and Irazoqui, P. P. (2014). Miniaturizing wireless implants. *Nature biotechnology*, 32(10):1008.

Morita, T. (2003). Miniature piezoelectric motors. *Sensors and Actuators A: Physical*, 103(3):291–300.

Narducci, M., Ferrari, M., Ferrari, V., and Campanella, H. (2014). Aluminum nitride soi lamb-wave resonators towards multi-frequency, multi-sensitive temperature sensor platform. *Procedia Engineering*, 87:1152–1155.

Nawito, M., Richter, H., Stett, A., and Burghartz, J. (2015). A programmable energy efficient readout chip for a multiparameter highly integrated implantable biosensor system. *Advances in Radio Science: ARS*, 13:103.

Nigam, V. K. and Shukla, P. (2015). Enzyme based biosensors for detection of environmental pollutants-a review. *Journal of Microbiology and Biotechnology*, 25(11):1773.

Pandian, P., Mohanavelu, K., Safeer, K., Kotresh, T., Shakunthala, D., Gopal, P., and Padaki, V. (2008). Smart vest: Wearable multi-parameter remote physiological monitoring system. *Medical engineering and physics*, 30(4):466–477.

Pang, W., Zhao, H., Kim, E. S., Zhang, H., Yu, H., and Hu, X. (2012). Piezoelectric microelectromechanical resonant sensors for chemical and biological detection. *Lab on a Chip*, 12(1):29–44.

Patolsky, F., Zheng, G., Hayden, O., Lakadamyali, M., Zhuang, X., and Lieber, C. M. (2004). Electrical detection of single viruses. *Proceedings of the National Academy of Sciences of the United States of America*, 101(39):14017–14022.

Platt, S. R., Farritor, S., Garvin, K., and Haider, H. (2005). The use of piezoelectric ceramics for electric power generation within orthopedic implants. *IEEE/ASME transactions on mechatronics*, 10(4):455–461.

Pozar, D. M. (2009). *Microwave engineering*. John Wiley & Sons.

Qiu, X., Oiler, J., Zhu, J., Wang, Z., Tang, R., Yu, C., and Yu, H. (2010). Film bulk acoustic-wave resonator based relative humidity sensor using zno films. *Electrochemical and Solid-State Letters*, 13(5):J65–J67.

Qiu, X., Tang, R., Zhu, J., Oiler, J., Yu, C., Wang, Z., and Yu, H. (2011). The effects of temperature, relative humidity and reducing gases on the ultraviolet response of zno based film bulk acoustic-wave resonator. *Sensors and Actuators B: Chemical*, 151(2):360–364.

Rayleigh, L. (1885). On waves propagated along the plane surface of an elastic solid. *Proceedings of the London Mathematical Society*, 1(1):4–11.

Roda, A., Guardigli, M., Calabria, D., Calabretta, M. M., Cevenini, L., and Michelini, E. (2014). A 3d-printed device for a smartphone-based chemiluminescence biosensor for lactate in oral fluid and sweat. *Analyst*, 139(24):6494–6501.

Sardini, E. and Serpelloni, M. (2010). Instrumented wearable belt for wireless health monitoring. *Procedia Engineering*, 5:580–583.

Sauerbrey, G. (1959). Verwendung von schwingquarzen zur wägung dünner schichten und zur mikrowägung. *Zeitschrift für physik*, 155(2):206–222.

Sharma, H. and Mutharasan, R. (2013). Review of biosensors for foodborne pathogens and toxins. *Sensors and actuators B: Chemical*, 183:535–549.

Steele, R., Lo, A., Secombe, C., and Wong, Y. K. (2009). Elderly persons? perception and acceptance of using wireless sensor networks to assist healthcare. *International journal of medical informatics*, 78(12):788–801.

Stern, E., Klemic, J. F., Routenberg, D. A., Wyrembak, P. N., Turner-Evans, D. B., Hamilton, A. D., LaVan, D. A., Fahmy, T. M., and Reed, M. A. (2007). Label-free immunodetection with cmos-compatible semiconducting nanowires. *Nature*, 445(7127):519.

Stern, E., Vacic, A., Rajan, N. K., Criscione, J. M., Park, J., Ilic, B. R., Mooney, D. J., Reed, M. A., and Fahmy, T. M. (2010). Label-free biomarker detection from whole blood. *Nature nanotechnology*, 5(2):138.

Sze, S. and Ng, K. K. (2007). Photodetectors and solar cells. *Physics of semiconductor devices*, pages 663–742.

Tan, Y., Richards, D., Xu, R., Stewart-Clark, S., Mani, S. K., Borg, T. K., Menick, D. R., Tian, B., and Mei, Y. (2015). Silicon nanowire-induced maturation of cardiomyocytes derived from human induced pluripotent stem cells. *Nano letters*, 15(5):2765–2772.

Tesla, N. (1914). Apparatus for transmitting electrical energy. US Patent 1,119,732.

Tsubouchi, K. and Mikoshiba, N. (1985). Zero-temperature-coefficient saw devices on aln epitaxial films. *IEEE Transactions on Sonics Ultrasonics*, 32:634–644.

White, R. and Voltmer, F. (1965). Direct piezoelectric coupling to surface elastic waves. *Applied physics letters*, 7(12):314–316.

Xu, S., Zhang, Y., Jia, L., Mathewson, K. E., Jang, K.-I., Kim, J., Fu, H., Huang, X., Chava, P., Wang, R., et al. (2014). Soft microfluidic assemblies of sensors, circuits, and radios for the skin. *Science*, 344(6179):70–74.

Yantchev, V., Enlund, J., Biurström, J., and Katardjiev, I. (2006). Design of high frequency piezoelectric resonators utilizing laterally propagating fast modes in thin aluminum nitride (aln) films. *Ultrasonics*, 45(1-4):208–212.

Yantchev, V. and Katardjiev, I. (2013). Thin film lamb wave resonators in frequency control and sensing applications: a review. *Journal of Micromechanics and Microengineering*, 23(4):043001.

Zhang, H., Liang, J., Zhou, X., Zhang, H., Zhang, D., and Pang, W. (2015). Transverse mode spurious resonance suppression in lamb wave mems resonators: theory, modeling, and experiment. *IEEE Transactions on Electron Devices*, 62(9):3034–3041.

Zhang, S. and Yu, F. (2011). Piezoelectric materials for high temperature sensors. *Journal of the American Ceramic Society*, 94(10):3153–3170.

Zhang, Y. (2006). In situ fatigue crack detection using piezoelectric paint sensor. *Journal of Intelligent Material Systems and Structures*, 17(10):843–852.

Zhao, C., Lin, D., Wu, J., Ding, L., Ju, H., and Yan, F. (2013). Nanogold-enriched carbon nanohorn label for sensitive electrochemical detection of biomarker on a disposable immunosensor. *Electroanalysis*, 25(4):1044–1049.

Zhao, X., Ashley, G. M., Garcia-Gancedo, L., Jin, H., Luo, J., Flewitt, A. J., and Lu, J. R. (2012). Protein functionalized zno thin film bulk acoustic resonator as an odorant biosensor. *Sensors and Actuators B: Chemical*, 163(1):242–246.

Zhao, X., Pan, F., Ashley, G. M., Garcia-Gancedo, L., Luo, J., Flewitt, A. J., Milne, W. I., and Lu, J. R. (2014). Label-free detection of human prostate-specific antigen (hpsa) using film bulk acoustic resonators (fbars). *Sensors and Actuators B: Chemical*, 190:946–953.

Zheng, G., Patolsky, F., Cui, Y., Wang, W. U., and Lieber, C. M. (2005). Multiplexed electrical detection of cancer markers with nanowire sensor arrays. *Nature biotechnology*, 23(10):1294.

Zimmerman, M. D., Chaimanonart, N., and Young, D. J. (2006). In vivo rf powering for advanced biological research. In *28th Annual International Conference of the IEEE Engineering in Medicine and Biology Society, 2006. EMBS'06*, pages 2506–2509. IEEE.

CURRICULUM VITAE